ELSEVIER

Check for updates

A review on the distribution of relaxation times analysis: A powerful tool for process identification of electrochemical systems

Christian Plank [a,d,*], Tom Rüther [a,d], Leonard Jahn [a,d], Maximilian Schamel [a,d], Jan Philipp Schmidt [b,d], Francesco Ciucci [c,d], Michael A. Danzer [a,d]

[a] Chair of Electrical Energy Systems, University of Bayreuth, Universitätsstraße 30, Bayreuth, 95447, Bavaria, Germany
[b] Chair for Systems Engineering for Electrical Energy Storage, Universitätsstraße 30, Bayreuth, 95447, Bavaria, Germany
[c] Chair of Electrode Design for Electrochemical Energy Storage, Universitätsstraße 30, Bayreuth, 95447, Bavaria, Germany
[d] Bavarian Center for Battery Technology, University of Bayreuth, Universitätsstraße 30, Bayreuth, 95447, Bavaria, Germany
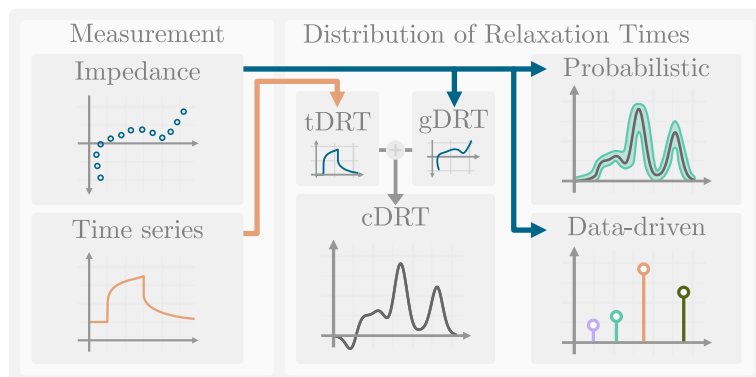
HIGHLIGHTS

- State-of-the-art methods for the Distribution of Relaxation Times analysis.
- Discrete and regularization-based solution algorithms.
- Probabilistic deconvolution method based on Gaussian Process optimization.
- Data-driven approach based on the interpolatory Loewner Method.
- Overview on measurement and data validation techniques.

GRAPHICAL ABSTRACT

ARTICLE INFO

ABSTRACT

The Distribution of Relaxation Times (DRT) analysis gained considerable attention for its ability to reveal detailed information about complex electrochemical processes without requiring a priori knowledge. This review provides a comprehensive insight into different methods of the DRT analysis, their mathematical bases, and the latest approaches to acquiring and analyzing frequency and time domain data. The analysis is based on the deconvolution of frequency domain data into a distribution function of gains at (pre-specified) relaxation times in the time domain, which improves the spectral resolution and separability of electrochemical processes. It provides valuable information about different electrochemical processes on different time scales, making it particularly useful for the characterization of both materials and electrochemical systems. The DRT analysis can be applied to arbitrary spectra containing electromagnetic effects, resistive–capacitive processes, and solid-state diffusion. To enhance process identification, a post-processing step involving peak analysis with Gaussian or RQ-distribution peaks is presented and the assignment of peak patterns induced by distributed processes like solid-state diffusion is discussed. In addition, a step-by-step workflow for the DRT analysis is provided to guide researchers from data acquisition and validation techniques to calculation and interpretation of the distribution function.

* Corresponding author.
  E-mail address: christian.plank@uni-bayreuth.de (C. Plank).

Abbreviations

cDRT	Combined distribution of relaxation times.
CPE	Constant phase element.
CT	Charge transfer.
DL	Double layer.
DOL	Degree of lithiation.
DRT	Distribution of relaxation times.
ECM	Equivalent circuit model.
eDRT	Extended distribution of relaxation times.
EI	Electrolyte interface.
EIS	Electrochemical impedance spectroscopy.
ekkt	Extended Kramers-Kronig test.
FLW	Finite length warburg.
FSW	Finite space warburg.
gDRT	Generalized distribution of relaxation times.
GITT	Galvanostatic intermittent titration technique.
GP	Gaussian process.
HC	Hard carbon.
HRR	Hydrogen reduction reaction.
kkt	Kramers-Kronig test.
LD	Lithium deposition.
LF	Loewner framework.
LFP	Lithium iron phosphate.
LIB	Lithium ion battery.
LM	Loewner method.
LTI	Linear time invariant.
NCA	Nickel cobalt aluminum oxide.
NIB	Natrium ion battery.
NMC	Nickel manganese cobalt oxide.
OCV	Open circuit potential.
ORR	Oxygen reduction reaction.
PBA	Prussian blue analogue.
PEMFC	Polymer electrolyte membrane fuel cell.
PITT	Potentiostatic intermittent titration technique.
PL	Passivation layer.
rGO	Reduced graphene oxide.
SEI	Solid electrolyte interphase.
SEM	Scanning electron microscope.
SIW	Semi infinite warburg.
SOC	State of charge.
SOFC	Solid oxide fuel cell.
tDRT	Time domain distribution of relaxation times.

Symbols

$C_{\Delta\text{Int}}$	Differential intercalation capacitance.
C	Capacitance.
H	Transfer function.
I	Current.
J	Cost function.
$K(x, y)$	Kernel function.
K	Non-ideal inductance.
L	Inductance.

N_τ	Number of time constants.
N_f	Number of frequencies.
Q	Non-ideal capacitance.
R	Ohmic resistance.
U	Voltage.
Z	Impedance.
$\boldsymbol{b}$	Measurement data of discrete DRT.
$\boldsymbol{x}$	Solution vector.
δ	Dirac impulse function.
γ	Frequency of the left dataset.
$\hat{V}$	Eigenvector.
$\hat{\Sigma}$	Eigenvalue matrix.
λ	Tikhonov regularization parameter.
$\mathbb{L}_S$	Shifted Loewner matrix.
$\mathbb{L}$	Loewner matrix.
$\mathbb{V}$	Vector of the transfer function (left dataset).
$\mathbb{W}$	Vector of the transfer function (right dataset).
$\ominus$	Experimental state.
$\hat{\mathbb{L}}_S$	Reduced Loewner matrix.
$\hat{\mathbb{L}}$	Reduced Loewner matrix.
$\hat{\mathbb{V}}$	Reduced vector of the transfer function (left dataset).
$\hat{\mathbb{W}}$	Reduced vector of the transfer function (right dataset).
$\mathbf{A}$	System matrix.
$\mathbf{B}$	Input Matrix.
$\mathbf{C}$	Output Matrix.
$\mathbf{D}$	Differentiation matrix.
$\mathbf{E}$	Mass matrix.
$\mathbf{G}$	System submatrix for the time domain distribution.
$\mathbf{I}$	Identity matrix.
$\mathbf{M}$	System submatrix for the resistive–capacitive distribution.
$\mathbf{N}$	System submatrix for the resistive–inductive distribution.
$\mathbf{P}$	System submatrix for the lumped elements.
$\mathbf{X}_k$	Left projection matrix.
$\mathbf{Y}_k$	Right projection matrix.
$\boldsymbol{\Gamma}$	Tikhonov regularization matrix.
$\boldsymbol{\Pi}$	Matrix of weights.
$\hat{\mathbf{A}}$	Reduced system matrix.
$\hat{\mathbf{B}}$	Reduced input matrix.
$\hat{\mathbf{C}}$	Reduced output matrix.
$\hat{\mathbf{E}}$	Reduced mass matrix.
ω	Angular frequency.
ϕ	Phase of impedance.
ψ	Frequency of the right dataset.
ρ	Riemann-Zeta function.
σ	Step function.
τ_0	Characteristic time constant.
τ	Time constant.
$\tilde{h}$	Distribution function (time-scale).
φ	Coefficient for non-ideal elements $0 \leq \varphi \leq 1$.
ξ	ZHIT derivative prefactor.

e	Squared error.
f	Frequency.
g	Normalized distribution function.
h_{LM}	Distribution of gains of Loewner method.
h_{RC}	Resistive–capacitive distribution function.
h_{RL}	Resistive–inductive distribution function.
h	Distribution function.
k	Model order, instance of discrete time.
p	Probability density function.
v	Impedance of the left dataset.
w	Impedance of the right dataset.
v_i	i'th value of the left eigenvector.
w_i	i'th value of the right eigenvector.

1. Introduction

In recent years, research and patent activity [1] in the field of electrochemical systems have experienced significant growth. Technologies such as batteries and fuel cells [2–4] are considered some of the most promising solutions to address environmental challenges and to achieve a more sustainable future. This increasing interest is also reflected in the associated materials and components [5], as well as recycling and remanufacturing [6–8]. To further improve and develop new electrochemical technologies ranging from materials up to system level, it is essential to understand the underlying processes through accurate process identification and comprehensive characterization.

Electrochemical impedance spectroscopy [9–11] and time domain measurements [12–14] emerged as the state-of-the-art non-destructive and non-invasive measurement techniques for obtaining impedance spectra and time series data. Unfortunately, a direct identification and quantification of polarization contributions of internal electrochemical processes is challenging.

To resolve this issue, equivalent circuit modeling (ECM), which is a widely recognized and well-adopted method for describing and interpreting a system's characteristics, is applied. In general, ECMs can be categorized as behavioral or respectively phenomenological models [15] . Their primary goal is not to provide a comprehensive description and understanding of all processes at a physical or physicochemical level, as seen e.g. in atomistic or microscopic models [16]. They are applied as a physically motivated approach to approximate the system's transfer function by combining various electrical circuit elements [16]. For example, Chu et al. developed a lumped ECM for the solid-electrolyte interphase of a Li-ion battery by model-order reduction and linearization of the physics-based model equations [17]. These models find application in a wide range of devices and systems, including electrical [18–20], electrochemical [21–23], fluid mechanical [24], and thermal effects [25,26].

However, interfacial processes in electrochemical systems exhibit a polarization distribution across a wide range of time constants, making it challenging to model them satisfactorily with lumped parameter models. To enhance the model's accuracy, multiple circuit elements connected in series can be employed, instead of assuming a single element for each process. While this approach improves model accuracy, it comes at the cost of reduced physical interpretability, complex parameter identification, and a higher risk of overparameterization [9]. Detailed reviews and comparisons of various equivalent circuit model approaches, with a specific focus on battery description, can be found in literature [15,27]. One significant drawback of this approach is the requirement for a priori knowledge of the expected processes in the system under investigation to propose a suitable ECM.

In this context, the Distribution of Relaxation Times analysis (DRT) offers the advantage of being a largely model-free approach, where

specific a priori knowledge about the system and its processes is not required to conduct the analysis and retrieve results. However, for an accurate interpretation, having knowledge about the electrochemical system and its multiple interconnected processes, is mandatory.

The DRT analysis enables the deconvolution of frequency domain data into a distribution of relaxation times function in the time domain, enhancing the resolution and thus increasing the separability of electrochemical processes, which are otherwise hard to distinguish in solely the impedance spectrum [28]. In addition to frequency data, this technique can also be applied to analyze time-series data obtained from pulse measurements [13,29]. After calculating the distribution function a post-processing step involving a peak fitting algorithm can be employed. By additionally conducting the analysis for different states this can be used to identify and quantify the distribution of polarizations between the involved processes [30]. Additionally, these findings can be instrumental in pre-identifying the number of dominant processes required for an appropriate ECM structure [9,22,31], rendering the DRT analysis as a superior tool for the analysis of electrochemical systems. Lu et al. presented a detailed perspective on the application of the DRT analysis for analyzing battery impedance spectra and how utilize the resulting distribution to identify processes and develop suitable electrochemical models [32].

The interpretation of the distribution functions so far is more oriented towards the evaluation of phenomenological observations through variations of SoC and temperature as well as towards the ECM theory. Yet an interpretation based on first-principles models of the DRT is not sufficiently covered in the literature. However, in recent research, impedance models derived from physics-based equations are used to analyze the relation between the DRT method and the first-principles model, and to develop a better understanding of how the electrochemical processes affect the resulting distribution function. Using this approach, Zhao et al. first investigated the porous electrode structures in Li-ion batteries [33], followed by a detailed analysis of the diffusion phenomena [34].

This review offers a comprehensive understanding of the distribution of relaxation times analysis, including its mathematical foundations, derivation of the distribution from impedance and time-series data using state-of-the-art methods, as well as the latest and novel approaches presented in the literature. As depicted in Fig. 1, the main content is divided into four sections. The first two sections cover the DRT analysis and provide examples of its applications, while the last two sections explain in detail how to obtain and validate frequency domain and time domain data obtained from measurements.

2. Calculation of the DRT

Besides solely resistive contributions, processes in electrochemical systems can generally be categorized into two main types: resistive–inductive and resistive–capacitive. Examples of resistive–inductive effects can be found in fuel cells, particularly in the low-frequency range, driven by complex electrochemical reactions [35,36]. In batteries, these effects occur in the high-frequency range and result from electromagnetic coupling due to cell geometry and wiring. On the other hand, resistive–capacitive effects are primarily associated with charge transfer reactions combined with double layers, surface processes, diffusional mass transport, or grain boundary conductivity. The main electrical circuit elements used in the context of electrochemical systems can be classified in ideal or lumped elements like inductance (L), resistance (R), capacitance (C), and non-ideal or distributed elements such as Warburg impedance (W), constant phase element (CPE) or (Q) and non-ideal inductance (K). The corresponding impedance of CPE and K can be calculated according to:

$$Z_Q(\omega) = \frac{1}{Q(j\omega)^\varphi} \tag{1}$$

$$Z_K(\omega) = K(j\omega)^\varphi \tag{2}$$
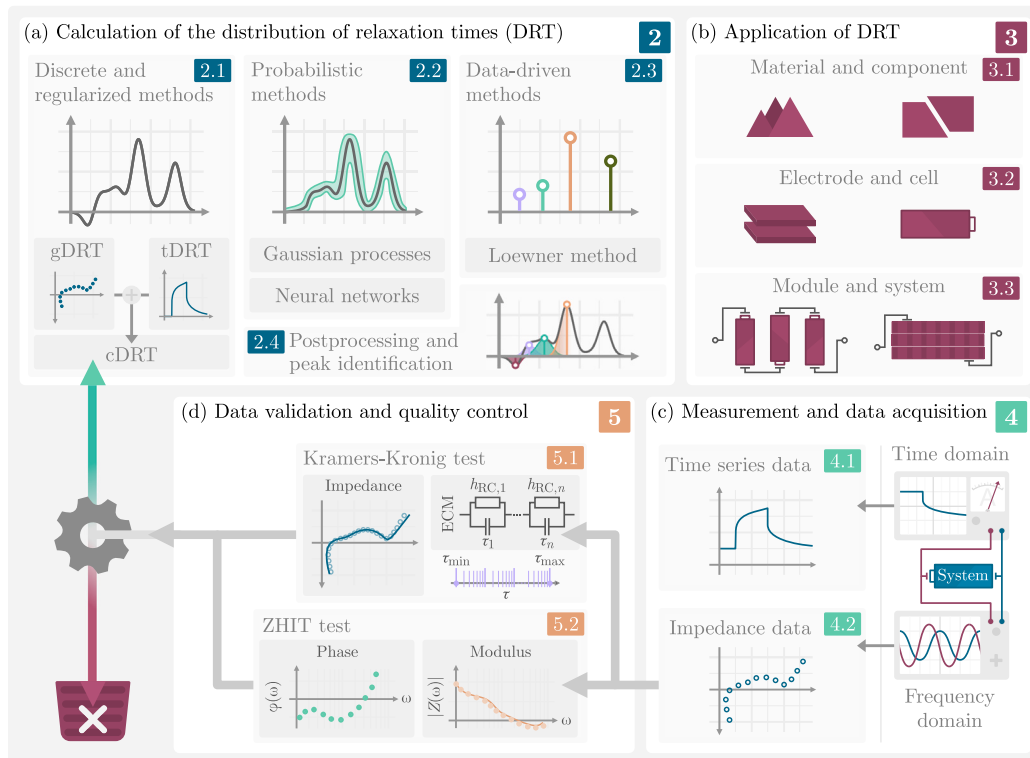
Fig. 1. The figure provides an overview of the structure of the review. (a) Section 2 covers the fundamental mathematical derivation of the DRT analysis and presents state-of-the-art deconvolution approaches, including the gDRT, probabilistic methods such as Gaussian process optimization and neural networks, as well as a purely data-driven approach using the Loewner Framework. (b) Section 3 presents examples from the literature showcasing various application levels for the DRT analysis, ranging from materials and electrodes to the characterization of modules and systems. (c) Section 4 explains the most commonly used measurement techniques for obtaining impedance and time-series data, while (d) Section 5 introduces two algorithms for data validation, enabling the selection of valid and invalid measurements.

with the phase angle φ as additional parameter in contrast to the lumped elements. At this point it should be noted, that the values of Q and K do not inherit the physical interpretation of an inductance and capacitance anymore. Resistive–capacitive processes are commonly described by a parallel connection of a resistor and a capacitor, forming what is known as an RC element. This arrangement results in the following transfer function

$$Z_{RC}(\omega) = \frac{R}{1 + j\omega\tau} \tag{3}$$

with the time constant $\tau = RC$. However, empirical findings by Cole and Cole in 1941 indicated that the complex dispersion of dielectric constants could not be adequately represented by an RC element. Instead, they proposed a depressed semicircle behavior [37]. Similar behavior can also be observed in the interfacial processes between the electrode and electrolyte. Mathematically, this phenomenon can be described by the transfer function of a CPE element in parallel with a resistor [9,38,39]. The transfer function is defined as follows:

$$Z_{RQ}(\omega) = \frac{R}{1 + (j\omega\tau)^{\varphi}} \tag{4}$$

Here, the time constant is denoted as $\tau = RQ$. Assuming that both time constants of the RC and RQ elements are equal, the real capacity of an RQ element can be determined by $C = \frac{\sqrt[\varphi]{RQ}}{R}$. A similar approach can be applied to the mathematical description of ideal or non-ideal resistive–inductive processes:

$$Z_{RL}(\omega) = \frac{R\,j\omega\tau}{1 + j\omega\tau} \tag{5}$$

and

$$Z_{RK}(\omega) = \frac{R(j\omega\tau)^{\varphi}}{1 + (j\omega\tau)^{\varphi}} \tag{6}$$

Here, the time constant is defined as $\tau = \frac{L}{R}$. The real inductance can be calculated similarly to the RQ element: $L = R\sqrt[\varphi]{RK}$. The main

difference between lumped and non-ideal elements is that the latter can only be described in time domain by using fractional derivatives for which no continuous analytical functions can be found [40,41]. As a compromise, these elements can be approximated by a serial connection of multiple lumped RC elements with differing time constants and polarization [15,39–41]. By applying a large number of serially connected RC elements, a transformation of the impedance data from the frequency domain into the time domain can be achieved, where each time constant possesses its own polarization contribution. With this approach, known as the distribution of relaxation times analysis, no a priori knowledge of the quantity and quality of the underlying processes is necessary for the analysis. Let the number of serially connected elements approach infinity and the limits range from zero to infinity, a continuous distribution function $h(\tau)$ can be found. Mathematically, the transformation between the frequency domain and the time domain can be described as a Fredholm integral of the first kind:

$$z(x) = \int_a^b K(x, y) \cdot f(y)\,\mathrm{d}y \tag{7}$$

Here, the kernel function is denoted as $K(x, y)$, the resulting function is represented by $z(x)$, and the desired function is referred to as $f(y)$. In the context of this problem, the kernel function corresponds to the transfer function of a resistive–capacitive RC-element, see Eq. (3), the resulting function $z(x)$ relates to the measured impedances $Z(j\omega)$, and the function $f(y)$ represents the distribution function. The variable x is substituted by the frequency ω, and y represents the time constants τ. The integral is evaluated over the time constants and the boundaries span from the minimum time constant (zero) to infinity. Typically, the ohmic offset R_0 is introduced into the equation, resulting in the well-known form for the DRT:

$$Z(j\omega) = R_0 + \int_0^\infty \frac{\tilde{h}(\tau)}{1 + j\omega\tau}\,\mathrm{d}\tau \tag{8}$$

As the integral equation is typically used in the logarithmic form, a substitution of $\tau = e^{\ln(\tau)}$ in the integral is required. It can be performed by introducing a new variable $u = \ln(\tau)$, which yields $e^u = \tau$. The differential $d\tau$ then becomes $d\tau = e^u du$ and the integral boundaries span from minus to positive infinity. Consequently, the Fredholm integral can be expressed in the logarithmic scale with $h(\tau) = \tau \bar{h}(\tau)$ as follows [42]:

$$Z(j\omega) = R_0 + \int_{-\infty}^{\infty} \frac{h(\tau)}{1 + j\omega\tau} d\ln\tau = R_0 + R_p \underbrace{\int_{-\infty}^{\infty} \frac{g(\tau)}{1 + j\omega\tau} d\ln\tau}_{=1} \qquad (9)$$

In some instances, the integral of this function is defined with an area of 1, where R_p represents the total polarization of the system and $g(\tau)$ the normalized distribution. However, it is important to note that in literature, the nomenclature for the log-scale distribution in (9) varies among authors: Boukamp uses $G(\tau)$ [43], Ciucci et al. employ $\gamma(\tau)$ [44,45], Danzer et al. opt for $h(\tau)$ [28,30], and Dion and Lasia did not introduce a specific variable name [46]. Also the assignment of $\gamma(\tau)$ is not consistent between publications. Dierickx et al. [47] uses $\gamma(\tau)$ according to time-scale distribution in (8) and the Group of Ciucci according to the log-scale definition in (9). For this review we want to use the presented notation which defines the relevant log-scale distribution function as $h(\tau)$, the normalized log-scale distribution function as $g(\tau)$ and the time-scale distribution as $\bar{h}(\tau)$. The distribution function is typically constrained to positive values. This makes the deconvolution of spectra with resistive–inductive features difficult. However, an analogous derivation for the Fredholm integral can be performed for resistive–inductive spectra by replacing the kernel function with the transfer function (5) of an RL element. An implementation of this option is found in the generalized distribution of relaxation times analysis in 2.2.1. In cases where the distribution of time constants is sought for time domain measurements, such as pulses, a modified transformation can be employed. Here, the kernel can be Laplace transformed into the time domain representation, resulting in an exponential function with a distinct time constant and polarization. Details on this can be found in Section 2.2.2. In general, Fredholm integral equations represent inverse ill-posed problems [43,48], implying the existence of multiple solutions. Nevertheless, not all of these solutions may have a physically meaningful interpretation. As described earlier, the solution space is therefore constrained to positive values, and some kind of regularization, filtering, or windowing technique is employed to filter out non-smooth distributions, reducing the number of possible solutions. Several different approaches have been published for solving this deconvolution problem. Schichlein et al. [49] used the Fourier transformation for analyzing solid oxide fuel cells (SOFC). Liedermann [50] applied this technique to investigate material permittivity, while Hershkovitz et al. employed a genetic algorithm to directly obtain the Fourier transform from impedance data. Ciucci's group utilized neural networks to extract the distribution from the spectrum [51,52]. Hörlin [53] presented a method based on the maximum entropy approach to investigate the electrochemical behavior of different electrode materials. Several research publications by various groups focus on probabilistic deconvolution methods using Gaussian processes and the Bayesian statistical framework [45,54,55]. Bergmann et al. [56] adapted and compared the iterative Van-Cittert and Gold algorithms, commonly used in image processing, for deconvolution of impedance spectra. They also compared these methods with the sparse-spike deconvolution technique, which is typically applied in the field of seismology. Recently, Rüther et al. [57] presented a completely data-driven approach based on the Loewner Framework [58] for model-order reduction for the investigation of a Li-ion battery. Yet the most commonly used approach so far involves discretizing the integral with respect to the time constants, resulting in the aforementioned series of RC circuits. Typically, the solution is obtained by applying Tikhonov L2-regularization to a linear optimization algorithm [28,30, 47,59–61]. Each of these methods has its own set of advantages and disadvantages, which primarily revolve around factors such as resolution,

separability of processes, preprocessing requirements (e.g., removing resistive–inductive effects or diffusive regions in the spectrum), and the constraints imposed on the resulting distribution function. In this review, we will primarily focus on discussing the most popular and novel methods, which include the discretization based method with Tikhonov regularization, the probabilistic deconvolution approach, and the data-driven Loewner method.

2.1. Direct inversions (analytic solution)

In 1941 Fuoss and Kirkwood [62] presented an analytic relation between the continuous transfer function in the frequency domain and the continuous distribution of time constants in the time domain

$$h(\tau) = \frac{1}{\pi} \cdot \left[Z_{\text{imag}}\left(j\frac{1}{\tau} \right) + Z_{\text{imag}}\left(-j\frac{1}{\tau} \right) \right] \qquad (10)$$

To perform the transformation, it is necessary to determine the imaginary part of the transfer function. Boukamp [43] used this method to derive the direct inversion of various electrochemical transfer functions. However, an alternative approach based on the Mellin transformation exists, which circumvents the need for determining the real or imaginary parts individually and instead operates directly with the complex transfer function [63,64]. Both transformations yield equivalent results, but the Mellin transformation offers the advantage of potentially requiring less effort, as it eliminates the need to extract the imaginary part. It is important to note that the resulting distribution is real-valued, meaning that the imaginary parts from both transformations must cancel out. This simplifies the calculation, particularly for the Fuoss and Kirkwood method, as only one part needs to be evaluated. The transformation applied to the imaginary part of the transfer function of an RQ element (4) yields the following analytical and continuous distribution with τ_0 as the characteristic time constant of the RQ element:

$$h_{\text{RQ}}(\tau) = \frac{R_{\text{RQ}}}{2\pi} \cdot \frac{\sin(\varphi\pi)}{\cosh\left(\varphi\ln\left(\frac{\tau_0}{\tau} \right) \right) + \cos(\varphi\pi)} \qquad (11)$$

The same can be applied to the non ideal resistive–inductive RK element (6), resulting in the negative distribution of (11):

$$h_{\text{RK}}(\tau) = -h_{\text{RQ}}(\tau) = \frac{-R_{\text{RQ}}}{2\pi} \cdot \frac{\sin(\varphi\pi)}{\cosh\left(\varphi\ln\left(\frac{\tau_0}{\tau} \right) \right) + \cos(\varphi\pi)} \qquad (12)$$

The analytical distributions and their derivation for other well-established impedance models, such as Gerischer and Finite-Length-Warburg, are presented in the work of Boukamp [43]. When comparing continuous distributions with discrete distributions, it is important to acknowledge that the analytical solution needs to be discretized. This can be achieved in log space by numerically integrating the analytic distribution between the center of two neighboring discrete time constant ranges.

2.2. Discrete and regularization based deconvolution methods

For non-synthetic measured data, a closed analytical solution cannot be found. However, a viable solution for the integral can still be found by approximation by means of discretization. Instead of a continuous description of the time constants τ, a prespecified and logarithmically spaced set of N_τ time constants $\tau = [\tau_{\min}, \ldots, \tau_k, \ldots, \tau_{\max}]$ is used for the calculation of a discrete distribution of relaxation times. Due to missing data in real measurements in the ranges from $f_{\min} \to 0$ and $f_{\max} \to \infty$, the integral limits are capped at $\tau_{\min}$ and $\tau_{\max}$. In general, the choice of the time constants is mathematically independent of the measured frequency points in the impedance spectrum. For the sake of smoothness of the resulting distribution function, in most cases N_τ is chosen as a multiple of the number of measured frequencies in the impedance spectrum N_f, i.e., $N_\tau = c \cdot N_f$, with $c \in [1, 2, 3]$ [28,30]. Typically, the minimum and maximum time constants are set according
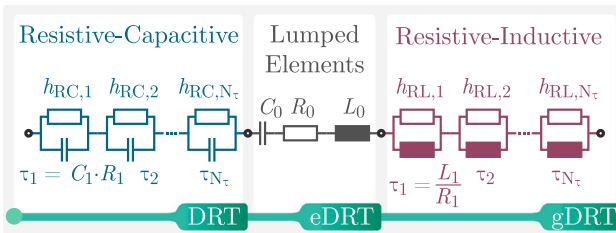
Fig. 2. Principle of DRT, eDRT and gDRT.

to the corresponding maximum and minimum frequencies of the spectrum, i.e., $\tau_{\min} = (2\pi f_{\max})^{-1}$ and $\tau_{\max} = (2\pi f_{\min})^{-1}$. Mathematically, though, this choice is not compulsory. An extension of the minimum and maximum preset time constant has been shown to be beneficial for the calculation of the DRT, especially for spectra with impedance values diverging from the real axis for low and high frequencies [28,30].

2.2.1. Extended and generalized distribution of relaxation times analysis

For a resistive–capacitive behavior of the impedance spectrum, i.e., impedance values in the fourth quadrant of the Nyquist plot with positive real parts and negative imaginary parts, with impedance values converging to the origin for high frequencies and to the real axis for low frequencies, the following impedance function is used

$$Z_{\mathrm{DRT}}(\omega) = \sum_{k=1}^{N_\tau} \frac{h_{\mathrm{RC},k}}{1 + j\omega\tau_k} \qquad (13)$$

with $h_{\mathrm{RC},k}$ being the coefficients of the discrete distribution function

$$h_{\mathrm{RC}}(\tau) = \sum_{k=1}^{N_\tau} h_{\mathrm{RC},k} \cdot \delta(\tau_k). \qquad (14)$$

at the prespecified time constants τ_k. Here, $\delta(\tau_k)$ is a discrete Dirac impulse in the time domain at $\tau = \tau_k$ that equals 1 for $\tau_k \in \tau$ and 0 everywhere else. The notation h_{RC} is used here to link the kernel function to its resistive–capacitive behavior, described by the transfer function (3) of an RC-element, and to distinguish it from the generalized DRT below where a different kernel function for resistive–inductive behavior is introduced. The total polarization resistance

$$R_p = \sum_{k=1}^{N_\tau} h_{\mathrm{RC},k} = R_p \sum_{k=1}^{N_\tau} g_{\mathrm{RC},k} \qquad (15)$$

equals the sum of all coefficients $h_{RC,k}$. The normalized distribution function $g_{\mathrm{RC}}(\tau)$ is calculated by $g_{\mathrm{RC},k} = h_{\mathrm{RC},k} \cdot R_p^{-1}$ with $\sum_{k=1}^{N_\tau} g_{\mathrm{RC},k} = 1$. The impedance function (13) of the DRT equals the transfer function of an equivalent circuit of N_τ RC-elements in series.

For impedance spectra with a shift in the real axis to positive values, with impedance values diverging to positive imaginary values for high frequencies, and diverging to negative imaginary values for low frequencies, the impedance function can be extended by lumped elements of an ohmic resistance, R_0, an inductivity, L_0, and a capacitance, C_0, as first introduced in [65]. As for the extended Kramers–Kronig test, which is in detail explained in Section 4.4.1, and as depicted in Fig. 2, the impedances of the resistor, the inductor, and the capacitor are added in series to the impedance of the DRT

$$Z_{\mathrm{eDRT}}(\omega) = Z_{\mathrm{DRT}}(\omega) + R_0 + j\omega L_0 + (j\omega C_0)^{-1} \qquad (16)$$

to yield the impedance function of the extended DRT (eDRT).

For impedance spectra with an additional resistive–inductive behavior, in [28] Danzer introduced a second kernel function and extended the eDRT by a serial connection of N_τ RL-elements, as shown in Fig. 2, that leads to the impedance function of the generalized DRT (gDRT)

$$Z_{\mathrm{gDRT}}(\omega) = Z_{\mathrm{eDRT}}(\omega) + \sum_{k=1}^{N_\tau} \frac{j\omega\tau_k \cdot h_{\mathrm{RL},k}}{1 + j\omega\tau_k}. \qquad (17)$$

Fig. 3 exemplarily shows the measured impedance spectrum of a wound lithium-ion cell (c), the two identified distribution functions for the resistive–capacitive as well as for the resistive–inductive part (a), the identified parameters for the lumped elements (d), the L-curve method for the determination of a mathematically optimal Tikhonov regularization parameter λ (see Section 2.2.3) (e) and finally the modeled impedance spectrum of the identified DRT in (c) as well as the residuals between measurement and reconstruction in (b). At this point, it is important to mention that the two resulting distributions are discontinuous but represented as continuous lines for visualization purposes. The same applies to the following figures containing discrete solutions for the distribution of relaxation times.

For the identification of the unknown model parameters the parameters of the distribution functions, $h_{\mathrm{RC},k}$ and $h_{\mathrm{RL},k}$, as well as the lumped parameters R_0, L_0, and C_0 are combined in the desired vector $\mathbf{x}$. The quality function of the optimization problem

$$J = \sum_{l=1}^{N_f} m\, e_{\mathrm{Re},l}^2(\omega) + \sum_{l=1}^{N_f} n\, e_{\mathrm{Im},l}^2(\omega) = \|\mathbf{A}\mathbf{x} - \mathbf{b}\|^2 \qquad (18)$$

is defined as the sum of the squared errors or the norm of the rearranged linear system of equations. The weighting factors m and n can be used, e.g., to normalize the impedance values to the maximum value. The given vector $\mathbf{b} = [\mathrm{Re}\{\mathbf{Z}_{\mathrm{meas}}\}; \mathrm{Im}\{\mathbf{Z}_{\mathrm{meas}}\}]$ contains both the real and the imaginary part of the measured impedance data. Alternatively, for linear systems fulfilling the Kramers–Kronig relations (44) and (45), the use of the real or the imaginary part only are also possible [30]. In the system matrix $\mathbf{A}$ all model parts of the resulting linear system of equations of the impedance function (17) are collected for all measured frequencies and all prespecified time constants, i.e., $\mathbf{A}(k,l) = \mathrm{Re}\{(1 + j\omega_l\tau_k)^{-1}\}$ and $\mathbf{A}(k, N_f + l) = \mathrm{Im}\{(1 + j\omega_l\tau_k)^{-1}\}$. For the ohmic resistance R_0 a single line with one element 1 is introduced in $\mathbf{A}$, for the inductivity and the capacitance two additional columns with the elements ω_l and $-\omega_l^{-1}$ are added. For the capacitance the inverse $\bar{C} = C_0^{-1}$ is used in $\mathbf{x}$ to fulfill the linearity condition in (18). A detailed derivation of the equation system can be found in Appendix A. The optimization problem to be solved is

$$\min_{\mathbf{x}} J(\mathbf{x}) = \min_{\mathbf{x}} \|\mathbf{A}\mathbf{x} - \mathbf{b}\|^2. \qquad (19)$$

If all parameters within (17) are positive, passive electrochemical systems can be characterized and $\mathbf{x}$ can be limited to $\mathbf{x} \in \mathrm{R}^{0+}$. For active systems such as photovoltaic cells, negative parameters need to be allowed. Since the system matrix $\mathbf{A}$ in the quality function, in most cases, has a high condition, a method of regularization is required to yield physically meaningful results in solving the optimization problem. In case of the Tikhonov regularization a penalty term is added to the unregularized quality function (18):

$$J_{\mathrm{reg}}(\mathbf{x}) = J(\mathbf{x}) + \|\boldsymbol{\Gamma}\mathbf{x}\|^2 \qquad (20)$$

with $\boldsymbol{\Gamma} = \lambda\mathbf{I}$, the identity matrix $\mathbf{I}$, and the regularization parameter λ. Alternative definitions of the regularization and a discussion on its effects can be found in [30]. The number of peaks or respectively the smoothness of the resulting distribution function depends on the choice of the regularization parameter λ. How to determine an optimal regularization parameter is discussed in Section 2.2.3.

2.2.2. Time domain distribution of relaxation times method and combination

Besides impedance measurements in the frequency domain, several other methods have been developed to transform measurements with excitation waveforms different from a sine into the frequency domain. These methods essentially rely on the Fourier transform [67], Laplace transform [68,69], or wavelet transform [70–73]. As a result, it is also possible to calculate the DRT from time domain measurements through the detour of impedance.

An approach for the direct calculation of the distribution of relaxation times was first proposed by Schmidt et al. in [13] and later
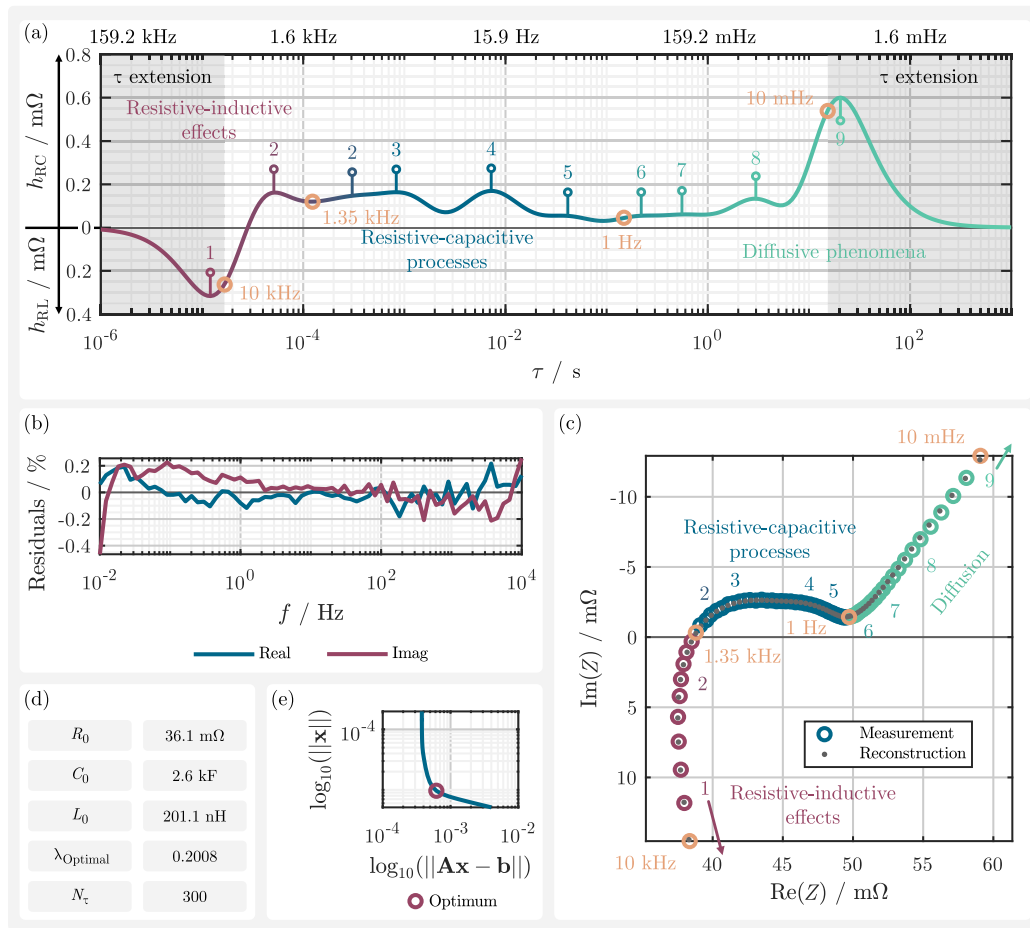
Fig. 3. Discrete distribution of relaxation times determined by the gDRT analysis (a) for an impedance spectrum (c) of a graphite — NMC 18 650 cell from the manufacturer Panasonic. The distribution of gains (a) and the Nyquist plot (c) are separated into the domains of diffusion, resistive–capacitive and resistive–inductive features by the low-frequency minimum (1 Hz) and the high frequency crossover (1.35 kHz). The peaks in the distribution of gains and the impedance spectrum are enumerated, with their positions indicating the corresponding frequencies of maximum of the peak. The mathematical optimal λ is determined by the kink point of the L-curve method (e) and the selected extension of time constants is marked in gray in (a). The list of the identified lumped parameters R_0, L_0, and C_0 is presented in (d). (c) shows the reconstructed impedance from the gDRT analysis and (b) the residuals between measurement and model prediction.

adapted by Wildfeuer et al. in [66]. This method requires that the system behavior can be represented by the DRT and a purely capacitive part. Consequently, by calculating the impedance from pulse measurements, the DRT is obtained as a by-product. This approach is referred to as the time domain DRT (tDRT) method. The tDRT can be utilized for lower frequencies through pulse measurements, while the electrochemical impedance spectroscopy measurement can be used for higher frequencies. The reason for this is the limited sampling frequency for pulse measurements and the increasing influence of nonlinearities and instationarities for impedance measurements in the low frequency range. These datasets can then be combined to form a comprehensive impedance spectrum containing both information.

Goldammer et al. [29] describes the identical procedure, but does not implicitly estimate the open circuit voltage as well, but subtracts it in a pre-processing step. Furthermore, the differential intercalation capacitance is not subtracted or implicitly co-estimated, so that the resulting spectra do not show a capacitive branch for low frequencies as LIBs usually do, but return to a real part of zero. This can be explained via the mapping of the behavior in this frequency range exclusively via the discrete DRT, which does not include pure capacitive behavior.

Basis for the approach is – as with the gDRT calculation in Section 2.2.1 – the transition from the continuous distribution function to a discrete one, which results in a finite and discrete sum of RC-elements. However, the kernel function for the Fredholm integral in Eq. (7) has to be replaced by the inverse-transform of the transfer function (3) of

a RC element in the Laplace domain into the time domain.

$$H_{\mathrm{RC}}(s) = \frac{R}{1 + s\tau} \quad \bullet\!\!-\!\!\circ \quad \frac{R}{\tau} e^{\frac{-t}{\tau}} \cdot \sigma(t) = h_{\mathrm{RC}}(t) \qquad (21)$$

As usual in signal and system theory, the $\bullet\!\!-\!\!\circ$ operator represents the inverse transformation into the time domain. The complex impedance can be obtained at any time by the identity $s = j\omega = j2\pi f$. Since excitation with a Dirac impulse $\delta(t)$ is practically impossible, an excitation signal is chosen instead which can be practically implemented. Hence, a current step with current I is applied. According to this, a convolution operation in the time domain must be performed with a step signal $I\sigma(t)$, which corresponds to a multiplication by $\frac{I}{s}$ in the Laplace domain. Therefore, the voltage step response is given by

$$U_{s,\mathrm{RC}}(s) = \frac{I}{s}\frac{R}{1 + s\tau} \quad \bullet\!\!-\!\!\circ \quad \left[1 - e^{\frac{-t}{\tau}}\right]\sigma(t) = u_{s,\mathrm{RC}}(t) \qquad (22)$$

By superposition of a negative and positive current step, the current pulse response can be calculated for a current pulse of length t_d

$$u_{p,\mathrm{RC}}(t) = IR\left[(1 - e^{\frac{-t}{\tau}})\sigma(t) - (1 - e^{\frac{-(t-t_d)}{\tau}})\sigma(t - t_d)\right] \qquad (23)$$

where it was assumed without further restrictions that the current pulse starts at $t = 0$. Correspondingly, the discrete DRT results in a sum of RC elements in the frequency domain with $\tau_n = R_n C_n$ and thus the response for the current pulse results in a sum of exponential functions

$$u_{p,\mathrm{NRC}}(t) = I\sum_{n=1}^{N} R_n\left[(1 - e^{\frac{-t}{\tau_n}})\sigma(t) - (1 - e^{\frac{-(t-t_d)}{\tau_n}})\sigma(t - t_d)\right] \qquad (24)$$
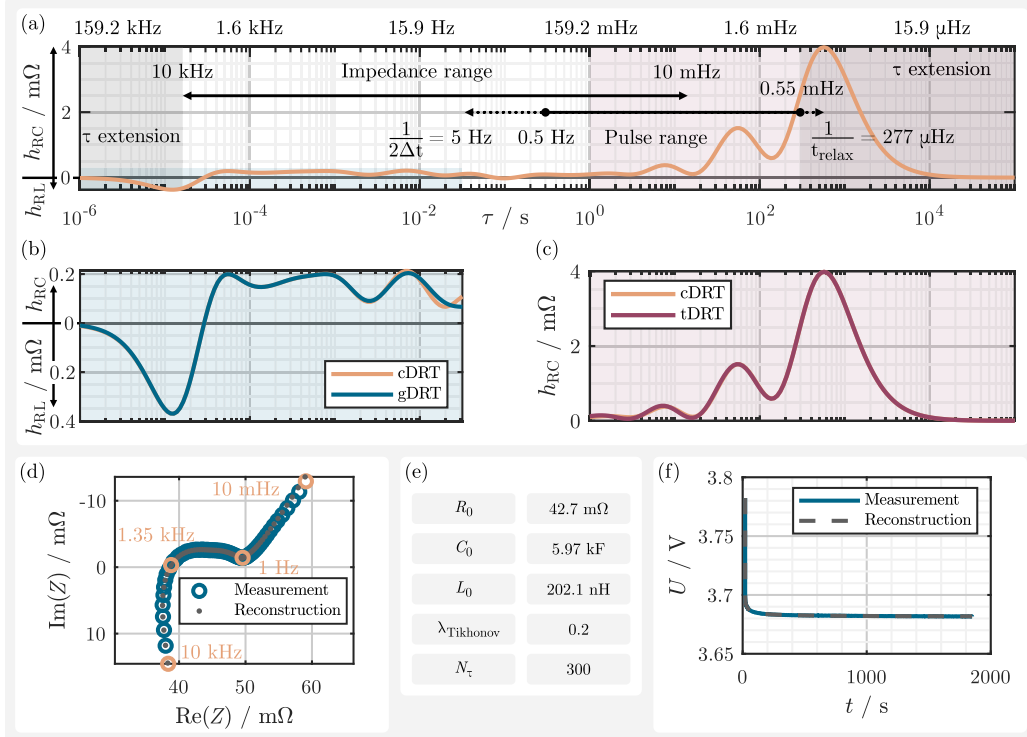
Fig. 4. (a) Combined DRT (cDRT) method, where time domain data from a pulse measurement (f) and impedance data from an impedance measurement (d) are fused according to [13,66]. The impedance data covers the frequency range from 10 kHz to 10 mHz. The pulse data theoretically spans from 5 Hz to 277 µHz, but is reduced to 0.5 Hz to 0.55 mHz. (b) Comparison of the distribution of gains derived by the gDRT analysis applied solely to the impedance data and the cDRT analysis. (c) Analogous comparison for only the pulse data obtained by the tDRT analysis. (d) Reconstruction from the cDRT solution shown for the impedance spectrum and the pulse data (f). (e) List of the lumped parameters and the corresponding regularization parameter λ used in the cDRT analysis, presented in a table.

Further effects like open circuit voltage or change of open circuit voltage due to SOC change, must be either subtracted before the fit, or implicitly considered in the equation. This is done simply, by extending the voltage by two additional terms, which are linearly dependent on the current I. It is important that the effects must be linear in nature. Accordingly, an inductance could also be included. The terminal voltage of the cell after switching off the current pulse, which still includes the open-circuit voltage U_{OCV} as well as the change of the open-circuit voltage by ΔU_{OCV} thus results in

$$u(t) = u_{p,NRC}(t) + U_{OCV} + \frac{I t_d}{C_{\Delta Int}} \tag{25}$$

Here, the change of the open circuit voltage in the last term is calculated via the differential intercalation capacitance $C_{\Delta Int}$ and the charge throughput of the current pulse $I \cdot t_d$.

The process of determining time constants and setting up the equation system for the time domain DRT method is analogous to the gDRT analysis described in Section 2.2.1. The key distinction lies in the fact that no separation between the real and imaginary parts is necessary, as time domain data is purely real-valued. Furthermore, the number of equations in the tDRT analysis is determined by the number of measurement data points, which is typically a lot higher compared to impedance measurements. For M discrete sampling times t_m, a system of equations with M equations and $N + 2$ parameters needs to be determined (if only the open circuit voltage should be estimated, and the differential intercalation capacitance not, the number of parameters is reduced by one). A detailed derivation of the equation system can be found in Appendix A.

As for the computation of the DRT in the frequency domain also for computation of the DRT from time domain data it has to be considered that the inversion is an ill-posed problem. In the present literature exclusively Tikhonov L2 regularization is used for the stabilization of the solution. This can be implemented analogously to the procedure with the computation in the frequency domain by multiplying the norm of the solution with the regularization parameter λ. In [66] a variation of the Tikhonov regularization is shown: from penalizing the amplitude, the first order derivative as well as the second order derivative which was used by Schmidt et al. [13]. In comparison to the computation of the DRT from frequency domain data, here still no alternative approaches to the Tikhonov regularization have been investigated.

The excitation signal is not limited to a current step. Accordingly, in Eq. (22) instead of a multiplication by s for the step response, other functions would have to be multiplied and correspondences in the time domain would have to be found. Furthermore, as in Eq. (23) for the construction of a pulse from two step functions, other functions can also be approximated via superposition.

The choice of time constants for the DRT is limited for large time constants by observation duration and for small time constants by sampling rate. While the minimum time constant is theoretically limited by the Nyquist–Shannon theorem and the sampling frequency f_s, practically higher values are obtained by a factor α, following:

$$\tau_{min} = \frac{\alpha}{\pi f_s} \tag{26}$$

Here, Wildfeuer et al. suggested $\alpha = 10$ [66], Schmidt et al. [13] applied $\alpha = 100$ and Goldammer et al. [29] used the theoretical limits of $\alpha = 1$. For the maximum time constant τ_{max}, with respect to the observation phase or relaxation duration t_{relax}

$$\tau_{max} = \frac{t_{relax}}{\beta \pi} \tag{27}$$

As suggested by Klotz et al. [67], Goldammer et al. selected $\beta = 8$, while Wildfeuer et al. extended the minimum time constant with $\beta = 2$ referencing [30]. Since classical impedance spectroscopy has clear advantages over time domain measurement at high frequencies in terms

of measurement duration and signal-to-noise ratio, the higher frequencies are characterized by EIS in [13,66]. While in [13] the impedance over the extended frequency range from time and frequency domain measurements is combined after calculating the tDRT, in [66] the combined DRT (cDRT) is calculated over the extended frequency range via a combined fitting on the individual DRTs based on frequency- and time domain.

Fig. 4 presents the distribution of gains for both the resistive–capacitive and resistive–inductive parts (a) obtained from the measured impedance spectrum (d) of a cylindrical lithium-ion cell. The distribution was calculated using the cDRT analysis applied to a combination of pulse and impedance measurement data. For the higher-frequency range, the impedance spectrum was analyzed using the gDRT analysis and compared to the distribution obtained by the cDRT analysis (b), while for the lower-frequency range, the tDRT analysis was compared to the cDRT (c). To ensure comparability, the number and range of the predetermined τ vector were kept equal for all three DRT analysis methods.

The lumped parameters and the regularization parameter λ used can be found in (e). As noted in (a), the usable measurement range of the pulse data is reduced following the recommendations given in Eqs. (26) and (27). By combining both datasets, the analyzable time constant range can be extended by more than one decade towards the lower frequencies.

To validate the results of the cDRT solution, both the impedance spectrum (d) and the pulse time series (f) were reconstructed, demonstrating a good agreement for both domains.

2.2.3. Determination of optimal regularization parameter

As depicted in Fig. 5, the regularization parameter significantly influences the resulting distribution function, emphasizing the importance of selecting an appropriate value. Different approaches for the determination of the optimal regularization parameter have been investigated in literature. Saccoccio et al. [74] introduced two sets of test functions for this purpose. The first, the real and imaginary discrepancy test function assess the difference between the real and imaginary part of the impedance computed by the DRT. The second approach, the real and imaginary cross-validation accesses the distance between the real/imaginary part of the experimental impedance and the one determined by the DRT. The discrepancy method was already used in 1990 by Honerkamp et al. in [75] for generally ill-posed problems by examining and comparing them with the PMSE method, which is based on minimizing the predictive mean squared signal error and the self-consistence method. They concluded, that the most robust and reliable results can be found for the self-consistence method. Another approach is the use of the L-curve method, which uses a logarithmic plot of the size of the regularized solution versus the size of the corresponding residuals for different regularization parameter values. From the bend point of the resulting characteristic L-curve, an optimal regularization parameter can be derived, which represents a compromise between the two values investigated. The method was firstly described in [76,77]. Paul et al. analyzed the application of this method to the DRT in [78]. In [30], Hahn et al. compared the previous mentioned approaches in terms of interoperability and summed squared error. They derive a rule of thumb for the regularization parameter, which has a value of 0.1 to 0.2. However, this value differs by orders of magnitude from other publications. In addition to the variation in electrochemical systems being studied, the determination of the optimal regularization parameter is significantly influenced by various meta-parameters. These include the signal-to-noise ratio of the measurement and the chosen number of time constants N_τ for the DRT analysis. Higher levels of noise and a larger number of elements result in an increase in the optimal regularization parameter. A more detailed assessment of the regularization parameter was conducted by Maradesa et al. in [79], who used synthetic experiments to test empirically how close the λ values obtained using cross validation scores and L-curve methods are to the optimal regularizer.

Sweeping through a large range of empirical tests, best results are achieved for the generalized [80] and the modified generalized [81] cross validation. In 2016, Zhang et al. [82] introduced an enhanced Tikhonov regularization method that eliminates the need for manual adjustment of the regularization parameter. This improvement involves replacing the single scalar parameter with a distribution and solving a modified optimization problem, where the distribution is optimized alongside the distribution of relaxation times function. Subsequently, Gavrilyuk et al. [83] conducted a thorough analysis of this method, focusing on its robustness against noise, frequency resolution, and the impact of differences in implementation. Their findings suggest that both methods yield different results, and the optimal choice between them may vary depending on the specific case.

2.2.4. Post-processing of distribution functions

The obtained distribution function does not inherently provide information, neither on the number of peaks nor on the assignments of single or multiple peaks to specific polarization processes. To address this issue, Hahn et al. [30] suggested a post-processing step involving the application of a peak analysis of the distribution function using Gaussian peaks:

$$h_{\text{Gauss}}(\tau, H_\text{P}, W_\text{P}, X_\text{P}, S_\text{P}) =$$
$$H_\text{P} \cdot e^{\left(-0.5 \cdot \left(\frac{(\log_{10}(\tau) - X_\text{P})(1 - \text{sign}[\log_{10}(\tau) - X_\text{P}] \cdot S_\text{P})}{W_\text{P}}\right)^2\right)} \tag{28}$$

Eq. (28) shows that the Gaussian peak can be mathematically defined by four parameters: the height H, the width W, the position X, and the skewness S. If a symmetrical peak distribution is desired, the skewness parameter can be set to 0, otherwise negative values allow for a left tilted and positive values for a right tilted peak.

To achieve a comprehensive solution for the gDRT analysis, both distributions $h_{\text{RC}}(\tau)$ and $h_{\text{RL}}(\tau)$ can be combined into a single distribution function $h(\tau) = h_{\text{RC}}(\tau) - h_{\text{RL}}(\tau)$. This allows the representation of the resistive–capacitive parts with positive and the resistive–inductive parts with negative values in a single distribution. The combination is possible due to the closed relation between the transfer function of an RC and RL element, as explained in Section 4.4.1. Regardless of whether the fitted distribution is combined or kept separate, using the logarithmic form of the distribution is essential.

Determining the number of peaks is a prerequisite for performing the peak fit. Using the first derivative to find local minima and maxima and the second derivative to identify overlapping peaks that may not produce distinct extrema, can achieve this. To distinguish between resistive–capacitive and resistive–inductive peaks, it is crucial to consider the sign of the combined distribution and account for any open edges in the boundaries. These open edges may introduce additional peaks outside the calculated range of time constants. Alternatively, analyzing the curvature of the distribution function has also proven to yield good and reproducible results.

As a new approach, we propose using the distribution function obtained from the direct inversion of the transfer function (4) of an RQ element as the model function for peak fitting.

$$h_{\text{RQ}}(\tau, H_\text{P}, W_\text{P}, X_\text{P}) = \frac{H_\text{P}}{2\pi} \cdot \frac{\sin(W_\text{P}\pi)}{\cosh\left[W_\text{P} \ln\left(\frac{X_\text{P}}{\tau}\right)\right] + \cos(W_\text{P}\pi)} \tag{29}$$

The RQ peak model is characterized by three input parameters: H_P for the peak height, W_P for width, and X_P for the position. In contrast to the Gaussian peak, these parameters have a direct physical interpretation as a non-ideal, distributed resistive–inductive element. Specifically, the polarization is represented by the height H_P, and the width W_P corresponds to the process distributedness φ. Both models utilize X_P as the equivalent of the time constant.

This makes the second approach more suitable for estimating electrochemical parameters when distributed processes are expected in the electrochemical system. Moreover, the direct inversion back to an impedance spectrum is possible with this model. However, for more
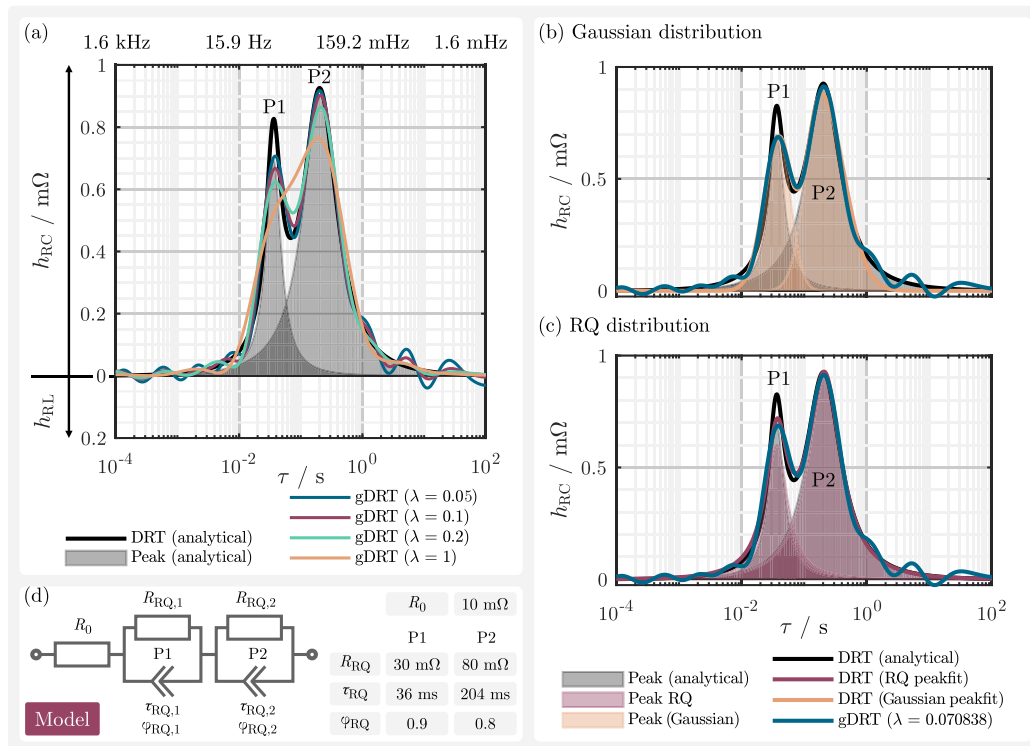
Fig. 5. (a) Distribution of gains obtained by the gDRT analysis with a variation of different λ's for a synthetic model consisting of a resistor and two RQ elements with specified parameters (d). For comparison the analytic distribution of gain (black and shaded gray) is calculated for each individual RQ element with Eq. (11) and summed for the total distribution. (b) shows the fit of two gaussian peaks (see Eq. (28)) to the distribution of gains obtained by the gDRT analysis with the regularization parameter λ determined by the L-curve method. (c) shows the same fit but with two RQ peaks (see Eq. (29)).

Table 1
Determined fitting parameters for the Gaussian and the RQ peak model compared to the input parameters of the synthetic ECM.

	R_∞	$R_{RQ,\,1}$	$R_{RQ,\,2}$	$\tau_{RQ,\,1}$	$\tau_{RQ,\,2}$	$\varphi_{RQ,\,1}$	$\varphi_{RQ,\,2}$
Model	120 mΩ	30 mΩ	80 mΩ	36 ms	204 ms	0.9	0.8
RQ	120.7 mΩ	34.8 mΩ	75.9 mΩ	36.6 ms	210.9 ms	0.866	0.807
	(+0.6%)	(+16.0%)	(−5.1%)	(+1.6%)	(+3.4%)	(−3.7%)	(+0.9%)
Gaussian	112.2 mΩ	36.2 mΩ	66 mΩ	39 ms	186.3 ms	–	–
	(−6.5%)	(+20.7%)	(−17.5%)	(+8.3%)	(−8.7%)	–	–

complex process distributions that differ from an RQ-distribution, the Gaussian peak model allows for a more general peak fitting, despite the drawback of lacking an equivalent description in the frequency domain. In the Gaussian peak model, the polarization can be determined by computing the area beneath each peak.

Parameter optimization necessitates nonlinear algorithms, which highlights the significance of precisely defined initial parameters and boundary conditions. In both scenarios, it is possible to estimate these values using the distribution function properties and the identified peak positions. Such properties are for instance the peak height, the distance to the neighboring peaks, and the sign of the distribution.

Fig. 5 shows the peak analysis with both peak models for a generic ECM consisting of a resistor and two RQ elements in series, with the parameters described in (d). The distribution function was determined by the gDRT analysis. In (a) the influence of the regularization is shown and compared to the analytical solution obtained by Eq. (11). Reducing the regularization parameter induces oscillations and improves the separability of processes with similar time constants. Stronger regularization reduces oscillations but also blurs processes. This once again emphasizes the importance of carefully selecting a regularization parameter, while also revealing the challenges in identifying peaks, as some may be caused by regularization and thus should not be considered. For both peak models (b) and (c) the regularization parameter was determined by the L-curve method as described in Section 2.2.3.

Both variants show good agreement for the overall distribution, with minor side peaks caused by the Tikhonov regularization technique. In cases where processes can be accurately described by RQ-distributions, individual Gaussian peaks display differences in form. In these instances, the RQ peak model performs better and provides a more precise representation of the underlying processes.

Table 1 compares the determined parameters with the input model parameters, thus confirming the visual findings. It is notable that the Gaussian peak model underestimates the overall polarization, whereas the RQ model exhibits less deviation in the time constants. The study shows that both methods exhibit increasing errors in polarization for the less distributed process, RQ_1, which is expected due to the higher error in the distribution obtained by the regularized gDRT for less distributed processes. In comparison, the trend for the time constants is vice-versa but the overall impact on the errors is much lower.

2.3. Probabilistic methods

The classical method for deconvolving the DRT involves using Tikhonov regularization (also known as ridge regression), which solves problem (8) to obtain the DRT. This approach has a Bayesian interpretation, which is well established in classical machine learning [54]. Specifically, given the probability of the impedance data, $p(\mathbf{Z}|\mathbf{x})$, in the context of the DRT model, and some prior knowledge on the DRT

encapsulated in a probability density function, $p(\mathbf{x})$. One can use Bayes theorem to write that [84]

$$p(\mathbf{x}|\mathbf{Z})p(\mathbf{Z}) = p(\mathbf{Z}|\mathbf{x})p(\mathbf{x}) \tag{30}$$

where $p(\mathbf{Z}|\mathbf{x})$ is the likelihood, which depends on the error model. Up to a multiplicative constant it follows that

$$p(\mathbf{x}|\mathbf{Z}) \propto p(\mathbf{Z}|\mathbf{x})p(\mathbf{x}) \tag{31}$$

If one chooses $p(\mathbf{x}) = \mathbb{1}(\mathbf{x})\exp\left(-\frac{\lambda}{2}\|\mathbf{D}\mathbf{x}\|^2\right)$, where $\mathbb{1}(\cdot)$ is the indicator function and $\mathbf{D}$ is a differentiation matrix, constrained ridge regression is recovered by maximizing the left hand side of (31). Most importantly, (31) provides a new interpretation for the DRT, which is not simply a single "point" in an approximation space but rather a random vector endowed with a certain probability distribution [84,85]. This implies that peaks identified by DRT deconvolution are also characterized by a certain credible band, which depend on the prior ($p(\mathbf{x})$) and the experimental data $\mathbf{Z}$. Furthermore, one can sample $\mathbf{x}$ given $\mathbf{Z}$ exactly using established frameworks [86,87].

The Bayesian interpretation can also be used to devise more advanced regularization models for the regularization. For instance, one can replace λ with a random vector $\boldsymbol{\lambda}$, endowed with a certain hyperprior distribution [84,88]. It has shown empirically that this makes and allows recovering DRTs with discontinuous features which would be otherwise smoothed out by naive Tikhonov regression [84].

Following the above notation, the matrix of weights (in general indicated with $\boldsymbol{\Omega}$) may be fixed or determined by experiments. Typically, this matrix is set to be proportional to a diagonal matrix, i.e., $\boldsymbol{\Omega} = \omega\mathbf{I}$. However, in a Bayesian context, the matrix $\boldsymbol{\Omega} = \text{diag}(\mathbf{w})$ can be assumed to be random where $\mathbf{w}$ is a random vector with its own prior distribution, $p(\mathbf{w})$ [89]. One benefit of this approach is that it enables the identification of outliers in the measured impedance spectrum. Dedicated algorithms can be employed to detect these frequencies and subsequently reduce the corresponding weight values. As a result, the algorithm can effectively censor these frequencies and improve the accuracy of the impedance measurements and the DRT deconvolution.

In the context of Bayesian statistics, peak deconvolution can also be performed using various methods. One such approach involves determining the mean DRT and then applying sequential peak assignment to deconvolve it. The optimal number of peaks can be determined using information-theoretic statistics, such as Akaike's information criterion or the Bayesian information criterion, which were discussed in the previous KK section. Moreover, assigning a certain probability to each peak can provide insight into its likelihood, holding great potential for assessing peak credibility and for separating likely from unlikely DRT features [90]. Furthermore these methods could be extended to devise quality indicators for the DRT [91].

2.3.1. Gaussian processes

In addition to the probabilistic extensions of vanilla ridge regression, probabilistic methods can also incorporate more advanced concepts such as Gaussian processes GP. In this context, the DRT is not considered a finite vector random variable, but rather a random process in an infinite space. It is assumed that the DRT itself is a Gaussian process, where the joint Gaussian distribution of two log tau values is endowed with a specific mean and variance [44]. As a result, since the DRT functional is linear, the impedance can also be modeled as a Gaussian process. By conditioning on the imaginary part of the impedance, it follows that $h(\log\tau)$ is a multivariate normal random variable

$$h(\log\tau)|\mathbf{Z}_{\text{im}}^{\text{exp}} \sim \mathcal{N}\left(\mu_h, \sigma_h\right) \tag{32}$$

where μ_h and σ_h are obtained analytically for any $\log\tau$. It is worth noting that the hyperparameters related to the Gaussian process can be determined in various ways, including through maximization of

the experimental evidence, thus maximizing the adherence of model prediction to data.

While the GP theory is very elegant it suffers from a couple of drawbacks. First, since the DRT is a GP, a non-negativity constraint is not easily enforced. Thus, $h(\log\tau)$ can feature spurious negative values. Second, the real part of the data cannot be used as the real part leads to a divergence in the impedance kernel. To obviate these issues finite GPs can be used whereby the underlying $h(\log\tau)$ is approximated with a finite collection of random variables [45]. Doing this stabilizes the kernel, and allows enforcing non-negativity constraints through the use of truncated normal distributions [45,92]. In addition to the advantages mentioned earlier, Gaussian processes offer exciting new opportunities for handling EIS data. These include the potential for active learning, the ability to predict spectra at frequencies that have not been tested, and the ability to generate EIS quality scores, among other capabilities. These advancements offer promising new directions for the field of EIS acquisition and analysis [55,93].

2.3.2. Neural network based methods

Neural networks can be employed to solve the DRT inversion problem in two ways. The first option, which is inspired by the deep-image prior [94], uses a deep neural network to generate the vector $\mathbf{x}$ such as the one defined above in Section 2.2.1 by setting $\mathbf{x} = \mathbf{x}_{\text{NN}}(\mathbf{y};\xi)$ where $\mathbf{y}$ is a vector containing neural network weights and biases, and ξ is a random number [95]. Optimization of weights and biases is obtained by solving

$$\hat{\mathbf{y}} = \arg\min_{\mathbf{y}} \|\mathbf{A}\,\mathbf{x}_{\text{NN}}(\mathbf{y};\xi) - \mathbf{Z}\| + \lambda\text{R}(\mathbf{x}) \tag{33}$$

giving the DRT approximation $\mathbf{x}_{\text{NN}}(\hat{\mathbf{y}};\xi)$. It is worth noting that "good" solutions to this problem can be obtained even if the regularization parameter, λ, is set to zero.

Alternatively, neural networks can be used as universal approximators of $h(\log\tau)$ by replacing the latter with a neural network, $h_{\text{NN}}(\log\tau;\mathbf{y})$, in the integral defined in Section 2 the DRT is replaced with a neural network $h_{\text{NN}}(\log\tau;\mathbf{y})$ [52]. In this case, more general approximations can be used for the integral in Eq. (7) leading to a problem formally identical to (33). While conventional DRT deconvolution is limited to single spectra, neural networks warrant more flexibility as. However, a multidimensional approach is required to analyze EIS spectra that depend on experimental conditions. Like the deep image prior one can think of augmenting the neural network inputs to include an experimental state $\boldsymbol{\Theta}$ leading to $h_{\text{NN}}(\log\tau,\boldsymbol{\Theta};\mathbf{y})$ [52]. Neural networks offer remarkable flexibility in solving the DRT inversion problem, as they can use unstructured data without specific spacing on state variables and frequencies, and are not constrained by the need for regularization. Despite having many more parameters than impedance data, these methods perform surprisingly well, and like Gaussian processes, they can be used for prediction. However, stability and computational time remain as issues, which can be addressed by using a pretraining step to fit $h_{\text{NN}}(\log\tau;\mathbf{y})$ against the $\mathbf{x}$ obtained using conventional methods [51]. While neural networks have demonstrated improved performance over ridge regression, further research is needed to validate their effectiveness, conduct error analysis, develop ad hoc regularizers, and conduct testing. This makes the DRT inversion problem an exciting and active area of research.

2.4. Data-driven methods

The distribution of relaxation times can also be determined using the purely interpolatory and data-driven Loewner method (LM) without the need for regularization, which was first introduced for batteries by Rüther et al. in [57]. The method is based on the Loewner framework (LF), which was originally used in [96] as a rational approximation tool and extended by an eigenvalue decomposition for the determination of underlying electrochemical processes in [97].

The measured impedance data of an electrochemical system can be described through the transfer function H

$$H(j\omega) = C(j\omega\mathbf{E} - \mathbf{A})^{-1}\mathbf{B}, \tag{34}$$

through the system matrix $\mathbf{A}$, the mass matrix $\mathbf{E}$, the output matrix C and the input matrix $\mathbf{B}$. The goal of LF is to form a surrogate model of the transfer function by determining the unknown matrices. For this purpose, both the impedance and the frequencies of the measurement are alternately spitted into a right and left data set and afterwards transferred into the Loewner matrix $\mathbb{L}$ and shifted Loewner matrix $\mathbb{L}_S$

$$\mathbb{L}_{(i,j)} = \frac{v_i - w_j}{\gamma_i - \psi_j}, \quad \mathbb{L}_{S,(i,j)} = \frac{\gamma_i v_i - \psi_j w_j}{\gamma_i - \psi_j}. \tag{35}$$

Here v and w describe the impedance and γ and ψ the selected measurement points $j\omega$ of the respective right and left data set. Based on $\mathbb{L}$ and $\mathbb{L}_S$, as well as the left vector of the transfer function $\mathbb{V}$ and the respective right vector $\mathbb{W}$ of it, the reconstructed matrices

$$\tilde{\mathbf{E}} = -\mathbb{L}, \quad \tilde{\mathbf{A}} = -\mathbb{L}_s, \quad \tilde{\mathbf{B}} = \mathbb{V}, \quad \tilde{\mathbf{C}} = \mathbb{W} \tag{36}$$

can be determined. If the model order of these matrices does not match that of the underlying system, singularities can occur in the Loewner matrices. These arise due to inherent redundancies in the matrices and must be eliminated by compression methods. As a result, a singular value decomposition is performed to identify the most important or dominant features. Different methods for determining the optimal model order k using this procedure were discussed in [57]. Using the determined model order, the projection matrices $\mathbf{X}_k$ and $\mathbf{Y}_k$ are now chosen as arbitrary truncated singular vector matrices. Those projection matrices are used to determine the reduced Loewner matrices $\hat{\mathbb{L}}$, $\hat{\mathbb{L}}_S$ and the reduced vectors of the transfer functions $\hat{\mathbb{V}}$, $\hat{\mathbb{W}}$ through

$$\hat{\mathbb{L}} = \mathbf{X}_k^T\mathbb{L}\mathbf{Y}_k, \quad \hat{\mathbb{L}}_s = \mathbf{X}_k^T\mathbb{L}_s\mathbf{Y}_k, \quad \hat{\mathbb{V}} = \mathbf{X}_k^T\mathbb{V}, \quad \hat{\mathbb{W}} = \mathbb{W}\mathbf{Y}_k. \tag{37}$$

A more detailed explanation on this step is given in [58]. The reduced system matrix $\hat{\mathbf{A}}$, mass matrix $\hat{\mathbf{E}}$, output matrix $\hat{\mathbf{C}}$ and input matrix $\hat{\mathbf{B}}$ can now be determined by applying

$$\hat{\mathbf{E}} = -\hat{\mathbb{L}}, \quad \hat{\mathbf{A}} = -\hat{\mathbb{L}}_s, \quad \hat{\mathbf{B}} = \hat{\mathbb{V}}, \quad \hat{\mathbf{C}} = \hat{\mathbb{W}}. \tag{38}$$

Those matrices can be directly used to calculate the reduced transfer function

$$\hat{H}(j\omega) = \hat{\mathbf{C}}(j\omega\hat{\mathbf{E}} - \hat{\mathbf{A}})^{-1}\hat{\mathbf{B}} = \hat{\mathbb{W}}(\hat{\mathbb{L}}_s - j\omega\hat{\mathbb{L}})^{-1}\hat{\mathbb{V}}. \tag{39}$$

which represents a purely data-driven and regularization-free representation of the original transfer function.

To determine the time constants and polarization contributions an eigenvalue decomposition must be performed. Therefore $\hat{\mathbf{A}}$ is incorporated into $\hat{\mathbf{E}}$ and

$$-\hat{\mathbf{A}}^{-1}\hat{\mathbf{E}} = \hat{V}\hat{\Sigma}\hat{V}^{-1} \tag{40}$$

is determined under the consideration of the eigen vector $\hat{V}$ and the matrix of eigenvalues $\hat{\Sigma}$. Here the diagonal entries of $\hat{\Sigma}$ correspond to the time constants τ. To determine the polarization contributions h_{LM},

$$h_{\mathrm{LM},i} = [\hat{\mathbf{C}}\hat{v}_i][\hat{w}_i^T\hat{\mathbf{B}}] \tag{41}$$

is solved, where v_i and w_i correspond to the ith column entry of the left and the right eigenvector. Using the time constants and polarization contributions, the familiar discrete representation

$$\hat{H}(j\omega) = \sum_i^k \frac{h_{\mathrm{LM},i}}{1 + j\omega\tau_i}, \tag{42}$$

of the transfer function results.

2.5. Discussion

In the previous sections, solutions to the fundamental mathematical inversion problem of the DRT analysis were presented. These include the gDRT, tDRT, and cDRT analysis based on a discretization and regularization technique for frequency and time domain data, a probabilistic approach based on the Bayesian optimization framework, and a purely data-driven model order reduction algorithm that utilizes the Loewner framework.

Regardless of the selected method, the calculation of the distribution function is possible without the need for any a priori knowledge, making it more reliable and reproducible than a widely used ECM fit. The resulting distribution can then be used to identify and understand the underlying processes of the system under investigation. However, interpreting the course and the distribution of the peaks might not always be straightforward, as they are influenced by meta-parameters like the regularization parameter and the electrochemical processes themselves. Here, additional prior knowledge of the system under study is advantageous. Further, every method may differ in specific peculiarities and restrictions, which are highlighted and discussed in the following section.

Comparison between DRT analysis methods: For a deeper insight into the mentioned challenges, a comparison between the gDRT- and the Loewner method is presented in Fig. 6. Here, as throughout the review, the same impedance measurement of a cylindrical lithium-ion cell from the manufacturer Panasonic was used as the input to the aforementioned deconvolution approaches. The used data provided by Rüther et al. is open-source and available for download at Zenodo [98]. To allow for an effective comparison, the lumped parameters R_0, L_0, and C_0, as well as the resistive–inductive processes, were subtracted from the original measurement. The values were taken from the results of Fig. 4. This step enables a more straightforward comparison between the methods since the Loewner method necessitates intricate post-processing when lumped elements are involved. More information regarding this can be found in [57].

When comparing the solutions obtained from the discrete gDRT analysis, which exhibits a discrete course of peaks, to the Loewner approach, it is evident that the latter produces scaled Dirac impulses at specific time constants, resulting in higher gains compared to the height of a single peak in the gDRT. Consequently, it becomes necessary to plot the results using two independent y-axes. However, if the area beneath one peak of the gDRT is summarized following the procedure outlined in Section 2.2.4, the difference in polarization is minimized.

Interpretation of diffusion: Fig. 6 identifies that both methods display a similar peak pattern for the higher time constants range ($\tau \geq 10^{-1}$), which is attributed to diffusion phenomena in electrochemical systems. In the Nyquist plot, this is typically rendered as an inclined straight line followed either by a closing semicircle or by a diverging incline in the imaginary part induced by a capacitance. However, due to measurement limitations in the low frequency range, the latter is often not visible in the spectrum. Solid-state diffusion phenomena are typically modeled by a type of Warburg diffusion [99]. The different variants are similar at higher frequencies, where they resemble the behavior of a CPE element [38], but begin to differ at lower frequencies. The finite-length Warburg (FLW) element exhibits a closing semicircle and the finite-space Warburg (FSW) element exhibits capacitive divergence [100]. Due to the limited frequency range of the measurement, it is not possible to distinguish between the mentioned Warburg diffusion types in the spectrum, so the CPE is often an appropriate choice for modeling the diffusive part.

Other electrochemical systems that show an electrochemical reaction alongside a transport diffusion phenomenon are commonly modeled using a Gerischer impedance diffusion model [101–104]. Examples of such systems are high temperature SOFC fuel cells [105,106] and mixed conducting materials [102]. In principle, the DRT can only approximate an FLW element with a closed semicircle at low frequencies.
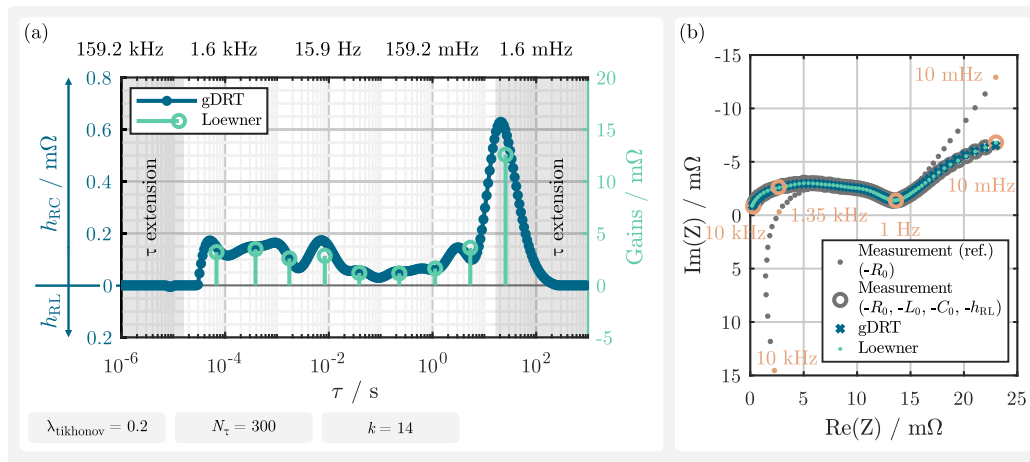
Fig. 6. The figure presents (a) a comparison between the gDRT and Loewner methods for the (b) reduced impedance spectrum of a lithium-ion battery measurement from the manufacturer Panasonic, where the lumped parameters R_0, C_0 and L_0 as well as the resistive–inductive effects are removed from the measurement reference spectrum. A good matching of the time constants and the polarization of the distribution of gains can be seen. Note that the selected model order k is higher than the resulting number of peaks. This is due to the required post-processing in the Loewner method [57].

This is evident when evaluating the reconstructed impedance spectrum in the extension range at low frequencies. In general, each gain in the distribution function corresponds to a closed semicircle because the kernel of the Fredholm integral is equivalent to the transfer function of an RC element. Empirically, it can be seen that the CPE behavior is represented by an increasing series of peaks, regardless of the method used for analysis. This observation is supported by the direct inversion of the transfer function of an FLW element by Boukamp [107], which also inherits the same pattern. However, transfer functions with divergent imaginary or real parts cannot be fully represented by the kernel used in the DRT. The reconstructed impedance spectrum is approximated correctly only in the analyzed frequency range and extrapolation will always results in a closed semicircle for low frequencies. This also explains why there is no direct inversion for elements with a divergent imaginary part, as it is the case for a CPE or FSW element. With the addition of lumped elements, especially the capacitance C_0, the gDRT analysis circumvents this restriction and allows the representation of an FSW element. A detailed overview regarding this can be found in the Appendix B.

What the DRT cannot provide is the exact identification and extrapolation of where the turning point for the Warburg diffusion types is expected if not included in the measurement data. Nevertheless this is also true for the widely used ECM model fitting technique. If the results of the gDRT in Fig. 3 are compared to the results of the cDRT in Fig. 4, it can be seen that neither the gDRT nor the cDRT can identify this turning point, though the cDRT results in a higher capacitance due to the increased limit at low frequency of the measurement data range.

Interpretation of peaks: In addition to the diffusion process, the resistive–capacitive part of the spectrum contains valuable information about the ongoing processes within the electrochemical system. As stated before, these include charge transfer phenomena, double layer effects, passivation layers, and interactions at the electrolyte interface. In combination they describe resistive–capacitive processes that generally do not appear as a process with a single time constant, but rather as a distribution of time constants. The more distributed the process, the broader the peaks in the distribution function are.

However, it is essential to note that a peak by itself does not always represent a distinct process within the system. Several factors can contribute to the presence of additional peaks:

First, the use of the Tikhonov regularization method in the gDRT can introduce smaller side peaks alongside the main peak (refer to Section 2.2.4). Similarly, in the data-driven Loewner method, distributed processes manifest as a series of gains (as discussed in [57]).

Second, it is possible for the same process to take place at both electrodes. However, their properties may vary slightly, leading to the appearance of two adjacent peaks. For instance, in the context of a battery, the charge transfer and double layer processes may occur at both electrodes, but subtle dissimilarities in the particle shapes and properties can result in minor differences in the associated time constants thus creating two peaks.

In summary, the presence of multiple peaks or distributed time constants must be carefully examined to ensure accurate interpretation and understanding of the underlying phenomena within the system.

Challenges and limitations: The following section will highlight and summarize the most significant challenges and limitations that arise when conducting the DRT analysis.

Kernel function. For the determination of the distribution function, a kernel function for the Fredholm integral must be selected. This also applies to the previously presented variety of discretization methods. For the analysis of electrochemical systems the transfer function of a resistive–capacitive element is used. This constricts the analysis to a single elementary transfer function. To overcome this limitation, the gDRT method includes lumped elements for capacitive and inductive phenomena. Resistive–inductive behavior can either be represented by a second distribution or by negative polarization in the distribution function. The Loewner method has no predefined kernels as it solely relies on data. However, the analysis of the system matrices involves interpreting the eigenvalues as time constants and associated gains, which implicitly confines the assumed type of underlying transfer function and makes the extraction of lumped parameters and resistive–inductive peaks difficult.

Linearity and noise. Most electrochemical systems exhibit a high degree of nonlinearity, therefore, the system should only be perturbed by small signals to allow a local linearization for impedance measurements. This deteriorates the signal-to-noise ratio and thus increases the influence of noise on the distribution. Electrochemical processes with low polarization could be overlooked because they are masked by the noise signal.

Uniqueness of the solution and regularization. The Loewner method is a purely data-driven and deterministic interpolation method. The computation of system matrices and transfer functions provides a unique result and the only degree of freedom is the order of model reduction and the interpretation of the eigenvalues. The other DRT methods discussed are based on solving an optimization problem with the distribution function as unknown. In most cases, this is an ill-posed problem with an ill-conditioned matrix for the linear system of equations. The required regularization with the regularization parameter as a degree

of freedom leads to a lack of uniqueness of the resulting distribution function. However, a careful choice of the regularization parameter leads to meaningful and reproducible results.

Peak identification and separability. For DRT methods that rely on regularization, even ideal RC elements, which correspond to Dirac impulses in the time domain, appear as Gaussian peaks. In the distribution function, the regularization acts as a low-pass filter, resulting in washed out peaks. The Loewner method does not suffer from this problem. For all DRT methods applies that discrete sampling points in the frequency domain lead to a necessary minimum separation of characteristic time constants. This mathematical implication makes it difficult to separate processes with similar time constants and their peaks in the distribution function and even more so in the case of regularization.

Parallel processes. The system description of all methods discussed correspond to a serial connection of elementary transfer elements. So far, parallel paths are not covered in the DRT analysis.

3. Application of DRT analysis on electrochemical systems

The distribution of relaxation times analysis offers a versatile tool for characterizing and analyzing systems across different scales: from material and component levels to electrodes and cells, and even up to the module and system levels. By understanding the properties and dynamics at different scales, scientists and engineers can make informed decisions to enhance the overall system's performance and durability.

3.1. Material and component level

Since impedance spectroscopy is the underlying measurement procedure for the calculation of the DRT in the frequency domain, it is inherently necessary to have a working electrochemical system. Therefore, DRT analysis for materials and components is scarce. While there are no publications on pure active materials known to the authors, some groups used DRT to analyze inactive components of batteries and fuel cells. To conduct this analysis, electrochemical systems are either operated without active material in blocking conditions or in a symmetrical setup, where both electrodes are made of the same active material at the same degree of lithiation (DOL). Fuel cells are operated in a symmetric setup, where both electrodes are supplied with the same gas. In all cases, the equilibrium potential of the cells will be 0 V but still may be excited by a voltage or current signal. With the reduced number of electrochemical reactions happening, the extraction of electronic or ionic transport processes becomes more manageable [108].

For LIBs, Hahn et al. [65] used symmetrical cells and cells in a blocking setup to measure the impedance of six different solid electrolytes at temperatures ranging from 25 °C to 80 °C. Using the eDRT and Tikhonov regularization they were able to identify a bulk-conductivity mechanism as main polarization contribution. They spotted the growth of an additional charge transfer process in the DRT for some solid electrolyte in a symmetrical cell, concluding that those materials are not chemically stable against lithium metal. Schadeck et al. [109] used the Tikhonov regularized DRT to analyze the implications of glass separators in graphite | lithium iron phosphate (LFP) cells with a liquid electrolyte. The change in DRT peaks assigned to the passivation layer and electrolyte interface (PL/EI) showed a decomposing effect of sodium borosilicate glass on the anode's solid electrolyte interphase (SEI). Zhuang et al. [110] investigated the effects of the amount of aluminum (Al) in Al-doped lithium lanthanum zirconium oxide (LLZO) solid electrolyte for LIBs using DRT. For low Al content they showed that increasing Al leads to lower time constants and polarization. For the highest Al-dopings, though, they identified additional polarization contributions for the grain boundaries due to phase segregation. Il'ina and Osinkin [111] analyzed an LLZO and lithium borosilicate (LBS) composite with Tikhonov regularized DRT. The DRT was used to investigate the influence of higher contents of LBS on time constants and polarization of the grain boundary and bulk transportation.

Lyagaeva et al. [112] used a combination of equivalent circuit modeling and DRT to deconvolute bulk and grain boundary transport resistances in a BCG ($BaCe_{0.9}Gd_{0.1}O_{3-\delta}$) proton conducting electrolyte for solid oxide fuel cells (SOFC). The SOFC was operated in a symmetrical setup with air on both electrodes. Contributions of bulk and grain boundary transport were separated by temperature variation. Kuzmin et al. [113] used the DRT to take a closer look at CZS ($CaZr_{0.95}Sc_{0.05}O_{3-d}$) electrolytes. The influence of temperature on the conductivity was quantified and the effect of different impurities on the grain boundary resistance was analyzed, finding that silicon (Si) significantly decreases the conductivity.

3.2. Electrode and cell level

In contrast to the material and component level, the DRT is an established method for the analysis of working electrodes and cells in fuel cells and batteries. The first application of EIS in combination with DRT on electrochemical storage technologies known to the authors was published by Schichlein et al. [49] in 2002. The motivation of the introduction of DRT to electrochemical systems was the ability to identify processes without the necessity to make assumptions on the model order a priori. Therefore, the DRT is extensively used to determine the number of processes in fuel cells and batteries, and how these contribute to the overall polarization.

For the process identification in batteries the DRT is applied to a variety of different chemistries. Shafiei Sabet et al. conducted a detail study on the time constants and polarization contributions in the impedance for a commercial NCA cylindrical cell [114] and NMC pouch cell [60] using DRT. Building half-cells for each electrode with an additional symmetrical Li—Li cell they were able to conclude on the contributions in the spectrum of the commercial full cells. Pan et al. [115] investigated the polarization contributions in LIBs with Si and silicon-oxide anodes by DRT. For the deconvolution of the processes they used symmetrical cells as well as half-cells under temperature and DOL variation. Zhao et al. in two publications developed methods for a physical interpretation of DRTs for effects in porous electrodes [33] and for solid-state diffusion [34]. In both cases the DRT was Tikhonov regularized and calculated similar to the gDRT. In the context of sodium-ion batteries (NIB) Mandl et al. [116] used the DRT with Tikhonov regularization to analyze the deposition and dissolution of sodium metal in symmetrical cells. The identification of main processes was conducted by investigating the changes of the impedance after storage at OCV. They concluded, that due to constant SEI growth, the polarization of the peak assigned to the PL/EI should increase. Furthermore, a variation of the temperature as well as the application of a DC offset was used to identify polarization contribution of the charge transfer and double layer (CT/DL). Subasinghe et al. [117] looked into monoclinic and rhombohedral prussian blue analogues (PBA) as cathode material in cylindrical NIB cells. In the Tikhonov regularized DRT the main polarization contributions of both PBA | hard carbon (HC) systems could be identified by SOC variation to be CT/DL and solid-state diffusion. Mohsin et al. [118] calculated the DRT for EIS of half and full cells at different SOCs to identify the dominant processes adding to the overall polarization for a novel NIB cathode material. Furthermore, the knowledge over the processes was used to conclude on the main degradation mechanisms during cycling. Since HC are a common anode active material for NIBs Schutjajew et al. [119] analyzed the sodiation and desodiation process of HC by looking at Tikhonov regularized DRT at different SOCs. Additionally, they used the results for the design and parameterization of an ECM. Further investigation of NIB anodes was done by Bottoni et al. [120] by looking into the influence of two different binders on the redox reaction of corncob HC. They identified PL/EI and CT/DL influences by variation of SOC and temperature in HC half cells. The DRT for

process identification is furthermore used in chemistries with lower technology readiness level like zinc-air [121], potassium-ion [122], lithium-sulfur [123], or lithium-oxygen [124].

The DRT though is not limited to the usage for process identification and modeling. In the following, applications of the DRT for cell design and aging analysis are shown. Togasaki et al. [125] used the DRT to calculate the utilization ratio of the cathode active material in solid-state LIBs and the dependency on the coating thickness, showing that thicker electrodes do not necessarily contribute to a higher energy density. Zhuo et al. [126] analyzed the influence of rGO additive to prussian blue cathode in NIBs by Tikhonov regularized DRT and found an improved performance of the cathodes with rGO additive in the high frequency range. For the analysis of the aging behavior of batteries, the changes in polarization can give valuable insight into the underlying process. Steinhauer et al. [127] used the eDRT to track the changes in the polarization of the PL/EI process during the formation of graphite half cells by measuring the EIS at certain potentials. After identifying the corresponding peak in the DRT, an ECM model was used to track the changes in resistance of the SEI. Rüther et al. [128] used a holistic DRT analysis that combined complementary DRT approaches to examine process variations among 92 commercial cylindrical cells. They found a non-normal distribution for most of the time constants and gains studied. They also performed a correlation analysis that allowed categorization of the identified processes into cell winding, electrochemical interface processes, and solid-state diffusion. Zhu et al. [129] measured the impedance at low temperatures to enable improved separation of single processes. By tracking the change in polarization of different processes during aging they could conclude on dominant degradation mechanisms verified post-mortem by SEM. A similar approach was used by Zhou et al. [130] to analyze the effects of high temperature aging on the cell's polarization contributions, while Rüther et al. [131] used the DRT to conclude on the main aging mechanism in context of the identification of inhomogeneities in the serial and parallel connection of cells. Since the deposition of metallic lithium (LD) on the anode of LIBs is a prominent aging mechanism during low temperature charging, various publications used the DRT in context of the detection of LD. Chen et al. [132] and Yi et al. [133] measured EIS after low temperature charging and used the DRT to track the changes in the polarization contribution of certain peaks. Chen et al. additionally recognized that LD alters the polarization of the peak assigned to CT/DL, by weakening it and shifting it to lower time constants. Katzer et al. [134,135] used the DRT to identify the characteristic frequency of the PL/EI process on the anode for the detection of LD. The knowledge about the characteristic frequencies enabled the detection by analyzing the impedance relaxation [134] and even online detection [135] of the degradation mechanism. Goldammer and Kowal [29] used the time domain DRT as online detection method for loss of active material in a commercial pouch cell.

Since the DRT method was first applied on fuel cells [49], it became an established method for process identification and polarization analysis in SOFCs as well as in polymer electrolyte membrane fuel cells (PEMFC). Papurello et al. [136] used the DRT with Tikhonov regularization to analyze the EIS of a SOFC under load. The regularization parameter λ was determined using the L-curve method. Identification of processes was accomplished by a variation of temperature of the cell and partial pressure of the anode and cathode gasses. The results of the DRT were used to design and parameterize an ECM which showed good agreement with the measurements for all test cases. A similar approach was chosen by Dierickx et al. [137], varying the air and fuel composition instead of the pressure. The DRT was again used for model parameterization, this time for a physicochemically motivated transmission line mode. The effects of parameter variation on the polarization was studied afterwards. An especially detailed analysis of the DRT of SOFC was conducted by Caliandro et al. [138]. The changes of the Tikhonov regularized DRT in an anode supported single cell SOFC, provided with air and H2, were investigated under the variation

of cell temperature, applied current density, partial pressure of oxygen (O_2), partial pressure of steam at the anode, as well as the flow rate, and fuel composition. While the partial pressure of O_2 showed effects on the O_2 diffusion and oxygen reduction reaction (ORR), the hydrogen reduction reaction (HRR) was influenced by changes of temperature, current density, and partial pressure of steam in the fuel. The changes in flow rate only influenced the gas conversion, while the high frequency resistance, probably determined by ionic transport mechanisms, was only altered by changing temperature. A similar investigation was conducted by Hong et al. [139] by looking into the influences of variation of temperature, pressure and flow rate on the polarization. They additionally used the Tikhonov regularized DRT to design and parameterize an ECM with split contributions for anode and cathode processes. Osinkin [105] conducted an analysis on the influence of the regularization parameter λ of the Tikhonov regularization on the DRT results for different cathode gasses as well as the use of an additional electrocatalyst. In further publications Osinkin used Tikhonov regularized DRT to deconvolute the polarization contributions of high performance SOFCs. The insights into the main polarization contributions enables the identification of hurdles and optimization potential for electrolyte compositions [140] and diffusion mechanisms [141]. Sumi et al. [142] investigated the changes of polarization contributions in the Tikhonov regularized DRT to analyze the aging in a micro-tubular SOFC. They found that CT/DL and ionic transport mechanisms are mainly influenced during the cell's operation.

Weiß et al. [143] analyzed the polarization contributions in a high temperature PEMFC using the DRT. The validity of the measured impedance spectra was confirmed by the Kramers–Kronig test and the Tikhonov regularization was applied on the DRT. The deconvolution of processes was conducted by supplying the cathode with air or pure O_2 and symmetric operation by supplying both electrodes with hydrogen (H_2). The knowledge about the underlying processes was then used to investigate the influences of changing the current density and gas stoichiometry on every process. Heinzmann et al. [144] used Tikhonov regularized DRT in combination with the variation of current density and relative humidity for process identification in a PEMFC. Furthermore, the separation of anode and cathode processes was achieved by varying the partial pressure and symmetric operation of the fuel cell with H_2. In a second publication [145] they used the knowledge about processes to develop and parameterize a transmission line model. Reshetenko and Kulikovsky analyzed the Tikhonov regularized DRTs for PEMFCs with low amount of platinum on the cathode [146,147]. First, they verified the polarization contributions determined by the DRT with a physics-based impedance model while analyzing the influence of the thickness of the cathode catalyst layer and the applied current density [146]. In the second publication they analyzed the influence of the position in the flow field [147] on the local and overall polarization, by using a segmented cell and measuring the impedance with a varying DC offset. Additionally, by testing a high-Pt PEMFC in a similar way, the influence of the amount of platinum catalyst was quantified depending on the current density. Yuan et al. [148] used EIS and DRT to parameterize a physical 2D PEMFC impedance model and analyzed the influences of changes in the model on the simulated impedance to identify promising approaches for material and system optimization. For further insights into the use of DRT on fuel cells the reader is referred to the review of Dierickx et al. [47].

For a better overview on the characteristic processes and especially the time constants linked to the processes, the literature used in this review was analyzed accordingly. The time constant may vary depending on the operating conditions of the system that were reported in the publication. Therefore, for each investigated system, e.g., the same electrode material once in a single layer cells, once in a cylindrical cell, an upper and a lower time constant was extracted together with the corresponding process. The results were split between batteries and fuel cells and all processes were assigned to one of the categories on the horizontal axis shown in Fig. 7. Due to the variation of different
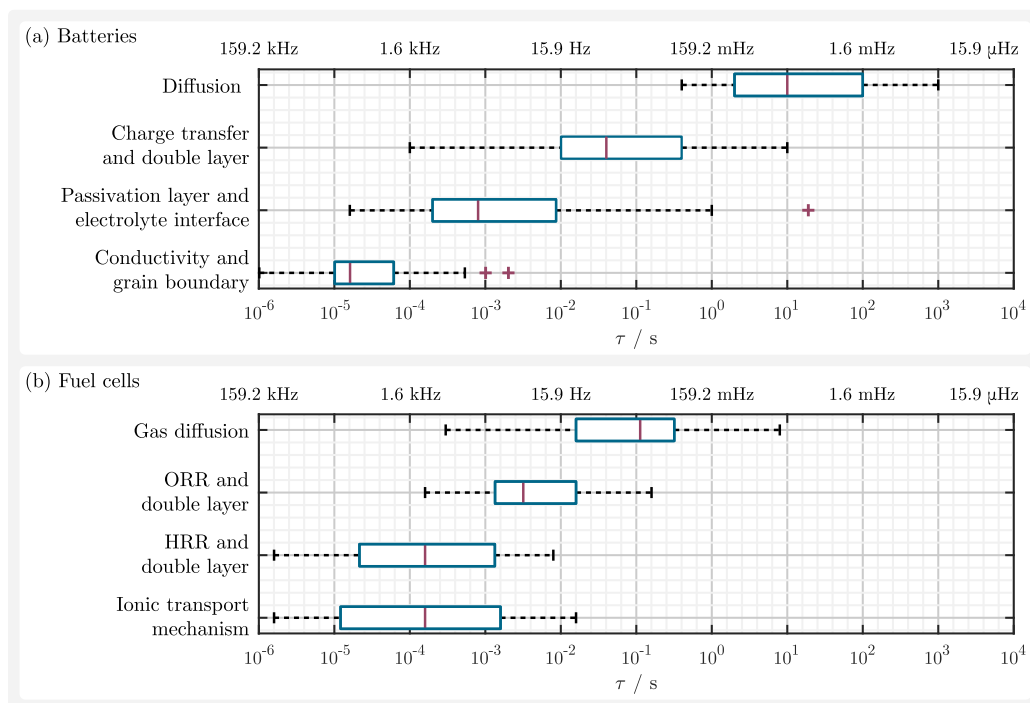
Fig. 7. Time constants of processes extracted for batteries [33,34,60,65,110,111,114–120,122–125,129–132,134,149,150] in (a) and fuel cells [105,112,136,138,139,142–144,146,147] in (b) from a total of 34 publications.

systems, electrodes and operating conditions, the deviation for all processes is high. For batteries though it becomes clear that in many cases diffusion as well as conductivity and grain boundary processes can be separated from CT/DL and PL/EI by a sole consideration of the corresponding time constant. While PL/EI in many cases is reported to be happening at smaller time constants than CT/DL, the large overlap in the quartiles of the boxplots shows, that a clear separation between both needs further analysis, e.g., by variation of temperature or SOC. For fuel cells the separation shows to be less clear between processes, especially for HRR and ionic transport mechanisms. The ORR is often reported as the rate limiting step at the electrode, which seems to be confirmed in the studied literature. When comparing batteries and fuel cells, it seems that the CT/DL process in batteries is reported to be even slower than the ORR, with the battery's diffusion processes happening several decades slower than the fuel cell's gas diffusion.

3.3. Module and system level

As it became clear from the preceding considerations, the calculation of the DRT is an ill-posed problem, whereby increased noise in the measurement data leads to a significant increased impairment of the inversion and thus to a poor resolution and broad peaks or artifacts. This becomes particularly relevant in the characterization of systems, since here, on the one hand, the impedances are usually considerably lower than in single cells and, on the other hand, the geometric dimensions are larger and inductive effects therefore play a greater role and affect the higher frequencies. These statements apply to both fuel cells and batteries. In addition to these effects, inhomogeneous conditions also play a role: when operating a fuel cell stack or a multi-cell battery, inhomogeneous conditions such as temperature gradients can occur. Accordingly, the total impedance at the system level results from the sum of the individual impedances and thus the DRT of the system consists of a superposition of peaks which are shifted depending on the inhomogeneous conditions [131]. This leads to a broadening of the peaks and again a loss of selectivity when trying to distinguish between different processes. It should also be noted that these inhomogeneities, temperatures and concentration

gradients, can also occur in individual large-format battery and fuel cells. In this configuration, the determined impedance then corresponds to a parallel connection of equivalent small cells with homogeneous but different boundary conditions. This in turn results in a superposition of the peaks shifted depending on the boundary conditions and thus again in a reduction of the selectivity. Both effects together (1) limitations due to the measurement equipment and (2) inhomogeneous operating conditions complicate the application and interpretation of DRT on the system level. Therefore, it is obvious that for the investigation of the underlying physical and chemical processes, small cell formats are used, and it also explains that the majority of publications deals with single cells and often smaller laboratory cells.

Nevertheless, especially with regard to the application of electrochemical systems, there is a need for diagnosis in order to operate the systems optimally with regard to performance, service life, and safety, as it is emphasized for lithium-ion batteries in [151]. Since monitoring of the individual cell voltages is implemented for lithium-ion batteries and fuel cell systems anyway, in many cases the impedance of the individual cells is determined rather than the impedance of the overall system. The determination of an overall impedance may be necessary or purposeful if access to the individual cell voltages is not available and, for example, a battery module or complete battery system is to be examined and evaluated by a third party. For Li-ion batteries, there are only a few examples in the literature with an impedance measurement above cell level: Togasaki et al. [152] have measured the impedance on four series connected commercial 18 650 cells (NCA/graphite) to detect an imbalance of the SOC. They argue that the method is interesting for bipolar cell designs of solid-state lithium-ion batteries, where the individual voltage and thus impedance cannot be measured. Tanim et al. [151] also detected imbalance of SOC in series as well parallel connected 16 Ah automotive lithium-ion pouch cells (NMC/graphite) and extended the diagnosis to the spread of aging. Measurements on lithium-ion batteries with a larger number of series connected cells and thus voltages higher than 100 V have been demonstrated by Yokoshima et al. [153] and Kasper et al. [154]. In the study of Yokoshima et al. it could be shown, that the impedance measurement on system level can be used to detect a single degraded module inside the battery pack,

whereas the focus on the study of Kasper et al. was to demonstrate the calibration of the impedance measurement for a automotive battery pack with 396 cells and the impact of the parasitic inductance while the interpretation of the impedance data was not addressed. Whereby all of these studies did not further evaluate the impedance above the DRT. Rüther et al. measured the impedance of up to 12 serially connected cells to detect inhomogeneities within a battery pack [131] On the other hand, applications of DRT can be found in the literature for lead–acid batteries [155–157]. This is certainly also due to the design of lead–acid batteries, since a serial connection of cells is used here without having access to the individual cell potentials in general. Despite the challenges mentioned for the application of the DRT to systems above cell level, it seems reasonable to strive for a DRT evaluation if the impedance data is of appropriate quality.

3.4. Discussion

The DRT analysis is applied on electrochemical systems from materials and single components over electrodes and cells up to modules and systems. The use of the DRT though is mostly applied on electrode and cell level, while the application on materials is scarce, due to the necessity for working electrochemical systems. For modules and systems the available literature is limited as well, probably due to the challenges imposed by low impedances, higher inductivities and influences of cell variations.

In the considered literature regarding batteries and fuel cells, some repeatedly used procedures for the analysis of the DRT can be singled out. For batteries the processes are usually analyzed by changing the SOC and temperature of the cell. This allows the differentiation between effects of CT/DL (reported to be changing with the SOC and temperature) and PL/EI (reported to be changing only with temperature). Since anode and cathode processes cannot be separated by these techniques, for the full process identification it is necessary to extract electrodes from the cells under test. While some publications neglect the influence of the lithium-metal counter electrode, a often used procedure is the building of a symmetrical Li cell to identify the processes attributed to lithium-metal dissolution.

For fuel cells, the common technique to deconvolute the processes visible in the DRT are the changes in partial pressure of the cathode and anode gasses. This is true for SOFC and PEMFC systems. While for the SOFC the third parameter variation usually is the temperature, for PEMFC the current density is altered.

When looking at the methods used to calculate the DRT it becomes obvious that the Tikhonov regularization, although it has significant downsides and various improved methods have been reported in literature, remains the most common method for the calculation of the DRT for fuel cells and batteries. Additionally, the vast majority of publications do not report the regularization parameter λ or how the chosen λ was achieved, while the influence on the resulting distribution cannot be underestimated. Furthermore, in most publications it is not reported how the authors handle lumped elements.

In conclusion, the DRT shows to be an often used and powerful method for the deconvolution of processes in various electrochemical systems, applicable from the analysis of electrolytes and separators in symmetrical cells up to whole fuel cell systems. For the reliable report of DRT results, the quality of both the measurement and the calculation and regularization methods are of utmost importance. In many cases, though, the publications using the DRT lack transparency on how the data was processed in order to get to the final results. Additionally, the quality of the underlying impedance measurements is rarely checked by methods like the Kramers–Kronig test (see Section 4.4).

4. Measurement and validation methods

The following section discusses state-of-the-art techniques for acquiring the measurement data that is essential for performing DRT analysis. These include time series data obtained by pulse testing, electrochemical impedance spectroscopy, and alternative measurement methods for frequency domain data. In addition, two validation methods are presented to assess whether the measurement conditions meet the requirements for linear and time-invariant systems necessary for reliable data analysis.

4.1. Pulse measurement

Pulse tests involve the application of a current or voltage perturbation that is not sinusoidal. In most of the cases, a current pulse of constant magnitude is applied, and the resulting voltage response is measured [13–15]. Typically, the duration of the pulse falls within the range of a few seconds up to a few minutes. Since the state of the system is assumed to change during the pulse, it is important to account for, e.g., state of charge (SOC) changes during the measurement. Afterwards, it is possible to exclude any OCV changes when the characteristic OCV curve is available [14]. The pulse response of the system can be divided into the instantaneous response, which includes the purely ohmic contribution R_0, and the transient response, which is influenced by electrochemical processes at the electrode/electrolyte interface, e.g. charge transfer, and slower processes such as diffusion phenomena. Due to the limited sampling frequency in the time domain, processes with small time constants can contribute mainly to the instantaneous response and are not visible in the transient part. This usually leads to higher R_0 compared to the values obtained by impedance spectroscopy. The transient part is commonly described by the superposition of multiple exponential terms with different time constants with or without a term describing the non-linear effects [12, 16]. This method can be used for the characterization of the internal resistance [14], the power capability [158], or diffusion characteristics of an electrochemical system (generally known as GITT or PITT method) [159–161]. Further, the time series data can be transformed into frequency domain [11,13], or used as input for the DRT analysis (see Section 2.2.2 for details). Pulse tests offer the advantage of a faster and more extended characterization of slower processes like solid-state diffusion [11,15], which usually require a sub millihertz range [13]. With pulse measurements this is easy achievable and compared to classical impedance spectroscopy measurement the time is drastically reduced [13,67].

4.2. Electrochemical impedance spectroscopy

Impedance spectroscopy is a highly effective and well-established method for analyzing electrochemical systems in the frequency domain by determining the transfer function H for either impedance Z or admittance $Y = Z^{-1}$, the reciprocal of impedance. To obtain H, a sinusoidal signal of a specific frequency is applied to the system, which serves as an eigenfunction of a linear time-invariant system (LTI). As such, the signal's shape remains constant as it passes through the system, and only its amplitude and phase are altered. To determine the impedance, the measured time domain signals must first be transformed into the frequency domain. This is the step with the highest computational effort and is typically achieved using methods such as Fourier transform or nonlinear least-squares fitting. Once the complex phasor is acquired, the impedance $Z(j\omega)$ respectively the transfer function

$$H(j\omega) = \frac{U(j\omega)}{I(j\omega)} \tag{43}$$

can be calculated. Overviews and tutorials on impedance spectroscopy can be found in [9–11].

To satisfy the LTI requirements, it is necessary to keep the excitation amplitude of the input signal low, in order to minimize nonlinearities in transfer processes and diffusion, as well as nonstationarities induced by changes in the state-of-charge (SOC) and the temperature, especially for low frequency sinusoids. This enables the system to operate at a linear

operating point that would otherwise be nonlinear for electrochemical systems. However, very low amplitudes lead to a poor signal-to-noise ratio, necessitating a trade-off between achieving linearity and minimizing measurement noise. In order to find an appropriate amplitude, it is advisable to first determine the average polarization of the system within the specified frequency range and testing conditions. Based on this information, the amplitude can be estimated by taking the resolution and accuracy of the measurement equipment being used into account. As a general guideline, it is recommended to measure low impedance devices like batteries in galvanostatic mode, which helps to estimate the SOC change during a half cycle, while also mitigating the risk of damage to the cell that may arise due to excessively high currents. On the other hand, the opposite is true for high impedance systems, such as material probes. In this case, it is advisable to utilize the potentiostatic mode to avoid too high voltages that may result from using a high input current. Nonetheless, with properly selected parameters, both measurement modes should yield equivalent results.

4.3. Alternative measurement techniques

In addition to the conventional approach of evaluating impedance at individual frequencies, as described in Section 4.2, numerous research articles have been published presenting alternative methods for impedance measurement.

One of the most popular approaches is based on multi-sine excitation signals [162–165]. The core idea is that by simultaneously overlapping multiple frequencies, the measurement time can be reduced to the duration required to analyze the impedance of the lowest frequency. In comparison to a classical frequency sweep, where each individual frequency is measured sequentially and the time is determined by the sum of every independent measurement, the duration of a multi-sine measurement is significantly reduced. This not only saves time but also helps avoid instabilities arising from changing internal and/or external states. However, signal design and post-processing via Fourier transformation are not straightforward and leave room for error, as well as opportunities for improvement and optimization, as demonstrated in detail by Zappen et al. [166] and more recently by Kallel et al. [167].

Other research groups employ different time domain signals, such as chirp signals [168], rectangular, sawtooth, or triangular shaped signals [169], sequences of rectangular pulses [170], or more advanced Sinc and Gaussian signals [171], which in theory contain a continuous frequency band. However, there are limitations due to measurement resolution and noise.

Another approach directly analyzes the system response to a white noise perturbation signal [172,173]. Compared to the other presented methods, the analysis of synthetic noise signals present worse results.

Some groups recommend to apply a RC model fit as a post processing step to smooth out the often noisy results of the Fourier transform [166,167].

4.4. Validation

To ensure accurate processing and analysis of impedance spectra, it is crucial not to violate the criteria proposed by the system theory for Linear Time-Invariant (LTI) systems throughout the measurement process. These can be summarized as follows: [10,174–176].

Linearity: In a linear system, the combined response to multiple input signals is simply the sum of their individual responses. Applied to impedance spectroscopy, the resulting impedance has to remain unchanged regardless of the input signal's amplitude. However, electrochemical systems, being inherently nonlinear, require linearization through the selection of small perturbations in order to achieve a linear response.

Stability and stationarity: The system should remain stable and exhibit no response unless perturbed by an input signal. Subsequent to the excitation, the system's response should converge to zero, allowing
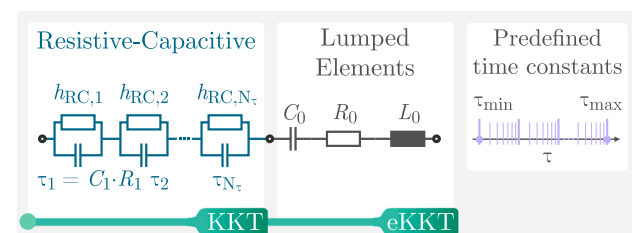
Fig. 8. Equivalent circuit model for the linear and extended Kramers–Kronig test.

it to return to its initial state without altering its inherent characteristics during the measurement process. When considering batteries, it is important to note that low-frequency perturbations can cause shifts in State of Charge (SOC) within a single half wave, while high amplitudes or uncontrolled environmental conditions can induce variations in cell temperature leading to time-variant behavior.

Causality: The system's response should solely rely on the current and past values of the perturbation as well as its internal states. Consequently, the system's response must be zero prior to any excitation, a principle that generally holds true for real-world specimens, as causality is a fundamental principle in physics.

The empirical detection of compliance with the aforementioned aspects involves repeating measurements under identical conditions and/or variations in the applied perturbation. However, this approach significantly prolongs the required measurement time and may not be feasible in certain cases. An alternative method is to utilize the Kramers–Kronig relation, which represents one of the earliest scientifically documented applications of the Hilbert Transform [177] and was independently introduced by Kramers [178] and Kronig [179]. The Kramers–Kronig relation establishes a link between the imaginary and real parts of a complex impedance spectrum through semi-infinite integrals:

$$Z_{\text{Im}}(\omega) = -\frac{2\omega}{\pi} \int_0^\infty \frac{Z_{\text{Re}}(\omega') - Z_{\text{Re}}(\omega)}{\omega'^2 - \omega^2} d\omega' \tag{44}$$

$$Z_{\text{Re}}(\omega) = Z_{\text{Re}}(\infty) + \frac{2}{\pi} \int_0^\infty \frac{\omega' Z_{\text{Im}}(\omega') - \omega Z_{\text{Im}}(\omega)}{\omega'^2 - \omega^2} d\omega' \tag{45}$$

In general, it is not possible to obtain a closed-form analytical solution for any measured impedance spectrum due to two major challenges that come with measured impedance spectra:

1. The frequency integral boundaries extend from $f_{\text{min}} = 0$ to $f_{\text{max}} = \infty$ in theory. However, due to practical limitations in the measurement setup, it is not possible to access frequencies within this entire range.
2. In applied impedance spectroscopy, the analyzed frequencies are typically distributed logarithmically with a finite number of measurement points. As a result, a continuous spectrum cannot be obtained, but rather a discrete representation of the impedance spectrum is acquired.

Although discretization of measurement points can be addressed by employing numerical methods to solve the integrals, the limitation imposed by the frequency boundaries remains a significant challenge. Various approaches can be found in the literature to tackle this issue. Some authors have employed extrapolation techniques to estimate the missing data [180], while others have utilized more advanced methods to extract sufficient information from an impedance spectrum, enabling the evaluation of the Kramers–Kronig integrals within an acceptable error range [181,182].

4.4.1. Kramers–Kronig validation

Today, the predominant approach in the scientific community, especially in the battery research, involves the indirect assessment of the Kramers–Kronig relation through the utilization of a Voigt equivalent-circuit model [174,183–185]. The central concept revolves around the notion that if a particular impedance spectrum can be expressed as a summation of valid transfer functions satisfying the Kramers–Kronig relations, then the measured spectrum itself must also meet the requirement of the Kramers–Kronig transferability. To be able to model arbitrary impedance spectra showing resistive–capacitive effects, as well as resistive–inductive, ohmic offset and pure capacitive or inductive contributions, it is necessary to extend the model with lumped elements. The inclusion of resistive–inductive effects can be achieved by permitting negative resistance values within the transfer function of the series of RC elements. This results in a comprehensive model consisting of a series of $N\tau$ RC elements, along with three lumped elements: R_0, L_0, and C_0. However, as indicated by

$$\theta = R_{\mathrm{RL}} = Z_{\mathrm{RL}}(R_{\mathrm{RL}}, \tau, j\omega) - Z_{\mathrm{RC}}(-R_{\mathrm{RL}}, \tau, j\omega), \tag{46}$$

attempting to represent the transfer function of an RL element using the transfer function of an RC element with negative resistive values introduces additional contributions to the ohmic resistor R_0. Consequently, the absolute value of the resistor does not possess a physical interpretation in general and should not be employed for quantitative statements. The same idea can be applied to the gDRT analysis described in Section 2.2.1, rendering the second distribution for resistive–inductive behavior obsolete (see Fig. 8). In order to validate the provided impedance spectrum, the model parameters have to be optimized for a minimal error between the measured and predicted data. The straight-forward approach involves employing a complex nonlinear least squares optimization [183]. However, this method is highly dependent on the initial starting point, making it less robust when applied to diverse impedance spectra. An alternative approach involves linearizing the system by predefining the time constants of the RC elements [183–185], resulting in a set of linear equations $\mathbf{Ax} = \mathbf{b}$. This enables the determination of parameters through a linear non-regularized optimization, enhancing robustness and reducing computational complexity.

When using a model-based approach, it is important to be aware of potential over- and underfitting. In case of the discrete Kramers–Kronig test, a too high model order for the series of RC elements can lead to mistune of the model to noise, nonlinearities, or instationarities in the data, leading to a false positive validation of the data. On the other hand, underfitting arises when the model fails to capture all the underlying patterns and relationships within the data. While underfitting is clearly visible to the scientist in the Nyquist plot, overfitting may be hidden in between the measurement points. Its therefore recommended to look at intermediate frequency points to detect loops and oscillations [184]. To ensure an accurate and reliable data validation, it is crucial to avoid these issues. For this reason Schönleber et al. [185] proposed a method to determine a considerable number of RC elements. However, this approach is not working reliably for spectra containing prominent resistive–inductive features. To find an optimal number for any arbitrary spectrum, Plank et al. [184] introduced three new features, based on the norm of the solution vector and the curvature of the predicted data. Data evaluation can be performed by analyzing the residuals of the real and imaginary part, which are composed of statistical and systematic errors. High levels of noise in the data are associated with increased statistical errors. Conversely, non-stationarities in the system introduce systematic errors, potentially caused by variations in internal or external states. Statistical errors exhibit a mean value of zero across the frequency range, while systematic errors tend to display tendencies or biases in the errors. Battery impedance spectra typically show systematic errors at very low frequencies, where changes in state of charge (SOC) and temperature may occur, as well as at very high frequencies, where electromagnetic coupling and all-pass characteristics are an issue [186,187].

4.4.2. ZHIT-transformation

An alternative method for validating impedance spectra involves utilizing the Hilbert transform. The mathematical transformations underlying this technique were independently developed by Kramers, Kronig, and Hilbert in the past. The linear version of the transformation is commonly attributed to the work of Kramers and Kronig, while the logarithmic transformation is associated with the contributions of Hilbert [186].

Electrochemical systems, being minimal-phase systems, exhibit a strong relationship between the logarithmic modulus and the phase of the transfer function. In mathematical terms, minimal-phase systems are characterized by having poles and zeros only in the left half of the s-plane [188]. In practical terms, this implies that the system must fulfill the aforementioned criteria and must not contain any all-pass contributions, such as delay or dead time. This represents an improvement over the Kramers–Kronig relations. The ZHIT algorithm, originally presented in this form by Schiller et al. [186,187], utilizes this relationship by constraining the Hilbert transform to minimal-phase systems. This leads to the following equation

$$\ln |Z(\omega)| = \ln |Z(0)| + \frac{2}{\pi} \int_{\omega_s}^{\omega} \phi(\omega') \, \mathrm{d} \ln \omega' + \sum_{k \geq 1 \in \mathbb{N}_{\mathrm{odd}}} \rho_k \frac{\mathrm{d}^k \phi(\omega)}{(\mathrm{d} \ln \omega')^k} \tag{47}$$

where $\ln |Z(0)|$ is a to be determined constant, ω the frequency under investigation, ω_s the starting frequency, and ω' the variable for frequency of the phase $\phi(\omega)$. For a more comprehensive description of the equation, further details can be found in [186,187]. Additionally, Ehm provides a detailed mathematical derivation in an unpublished document [189]. The prefactors ρ_k (see Table 2) for the odd derivatives of the phase can be determined by the Riemann-Zeta function:

$$\rho_k = -\frac{2}{\pi} \cdot \frac{1}{2^k} \cdot \zeta(k+1) \quad \text{for} \quad k \in \mathbb{N}_{\mathrm{odd}} \tag{48}$$

Typically, only the first derivative is used, as the prefactors exhibit an exponential decrease, resulting in diminishing influence from higher order derivatives. Consequently, this approach leads to higher errors in regions with a strong curvature, while yielding lower errors in regions characterized by a relatively flat curve.

A significant difference from the Kramers–Kronig relation is the localized nature of the integral, which lacks the semi-infinite boundaries. Instead it can be applied to a certain bounded frequency range. This characteristic allows for direct numerical analysis without the necessity of employing model discretization. In theory, the transformation can be performed in either direction, converting from phase to modulus or vice versa. However, the transformation from phase to modulus exhibits two distinct advantages, making it the superior approach. Firstly, the integral term is the dominant contribution, and integrating data is less affected by noise. Secondly, deviations from steady-state conditions typically have a lower impact on the phase compared to the modulus [187].

In the majority of impedance measurements, it is mandatory to apply a smoothing interpolation filter to refine the phase data. This step is essential to ensure that a accurate derivation is possible. Additionally it also helps to improve the numerical integration.

As the final step, it is necessary to determine the constant $\ln |Z(0)|$ by performing a linear regression in the logarithmic domain between the reconstructed and measured modulus. However, it is not advisable to include the entire frequency range due to potential steady-state errors at very low frequencies and the increased probability for mutual induction phenomena at very high frequencies. Therefore, it is recommended to conduct the regression within a medium frequency band to avoid an averaging effect between valid and invalid regions.

To accomplish a final data validation, one can examine the differences in the modulus prediction. If systematic deviations can be observed, a violation of the aforementioned criteria is highly probable rendering the spectra invalid. Alternatively, one can analyze the residuals of the reconstructed impedance according to the procedure

Table 2
Prefactors for ZHIT derivatives.

k	$\zeta(k+1)$	ρ_k
1	$\zeta(2) = \frac{\pi^2}{6}$	$-\frac{\pi}{6} \approx -0.52$
3	$\zeta(4) = \frac{\pi^4}{90}$	$-\frac{\pi^3}{360} \approx -0.086$
5	$\zeta(6) = \frac{\pi^6}{945}$	$-\frac{\pi^5}{15120} \approx -0.0202$
7	$\zeta(8) = \frac{\pi^8}{9450}$	$-\frac{\pi^7}{604800} \approx -0.005$

described for the Kramers–Kronig test in Section 4.4.1. The spectrum can be calculated with the predicted modulus and the measured phase.

So far, the ZHIT algorithm is much less used compared to the Kramers–Kronig relations, however there are recent publications in which the ZHIT algorithm was used for validation purposes and also for drift correction of corrupted impedance spectra in fuel-cell applications and corrosion barrier coatings [190,191]. Compared to the Kramers–Kronig test, the ZHIT technique is capable of validating bandwidth-limited measurements without the need of a model based approach for solving the underlying mathematical relation. Both methods are powerful tools with their own advantages and disadvantages for data validation.

4.5. Discussion

Despite their clear importance, KK relations are not widely used while analyzing EIS spectra, possibly due to the difficulty in understanding the theory and the availability of software can easily provide quantifiable and simple ways to quantify the EIS data quality. One approach to obviate this challenge is to devise scores that can gauge how experimental data fare against KK tests [192]. This involves two steps. First, one part of the experimental data (e.g., the imaginary part of the EIS spectrum) is regressed using a model, typically the DRT. Second, the model is used to predict the remaining part of spectrum (e.g., the real part). Finally, this prediction is compared to the experimental data. In the comparison, generally probabilistic metrics can be identified based on residuals, mean predictions, and distances between estimated distributions.

Metrics have been designed to provide a quantitative score between 0 and 100%, where 100% implies "perfect" KK compliance. One such metric uses residuals by computing the percentage of experimental points that lie within a set number of standard deviations of the KK mean prediction [192]. For example, if all experimental points of one portion of the EIS experimental data fall within the defined confidence band, a perfect 100% score is obtained. Other scores leverage the interpretation of the DRT and impedance as random variables (see 2.3) by computing the probabilistic distances between a subset of experimental data (and possibly their regression) and predictions drawn from a complementary subset of the EIS spectrum [55,192]. Accurate scoring of impedance spectral quality using the DRT analysis is crucial for certifying the reliability of EIS experiments. Thus, widespread development and adoption of scoring methods is expected not only for post hoc analysis but also online during experimentation.

5. Conclusion

The distribution of relaxation times analysis is a powerful and largely model-free approach that allows the deconvolution of frequency domain data into a distribution of relaxation times function in the time domain, enabling enhanced spectral resolution and thus better separation of electrochemical processes. Compared to the widely used equivalent circuit modeling technique, no a priori knowledge of the underlying processes is required, allowing for a straightforward analysis. The resulting distributions can be used to identify and track changes of relevant processes over different temperatures, states of charge or states of health, allowing for more reliable and accurate characterization.

According to the visual presentation in Fig. 1, the concluding remarks of this review follow the workflow of the DRT analysis, summarizing the key aspects from obtaining measurement data to interpreting the distribution function. It outlines the steps necessary for a successful implementation of the distribution of relaxation times method, which includes acquiring impedance and time-series data, applying appropriate deconvolution techniques, and interpreting the resulting distribution function to gain insights into the underlying electrochemical processes. By following this comprehensive workflow, researchers can effectively analyze electrochemical systems without the need for specific a priori knowledge, enhancing the understanding and optimization of such systems for various applications.

Data acquisition: Impedance spectroscopy is used for analyzing electrochemical systems and the resulting data is the input for the DRT analysis. For this, sinusoidal signals with distinct frequencies are applied sequentially to the system and its output values are determined. To identify the transfer function in the frequency domain the measurement data is transformed into the frequency domain using methods like Fourier transform or nonlinear least-squares fitting. Alternative excitation signals, such as multi-sine or various other time domain signals, have been explored to reduce measurement time and decrease the lower frequency limit reachable by classical impedance spectroscopy. To obtain qualitative good and valid measurement data, low-impedance specimen like batteries should be measured by 4-wire setup with short and pairwise twisted/shielded cables in galvanostatic mode. High-impedance systems should be measured in potentiostatic mode. For the amplitude, a trade-off between measurement noise and linearity conditions must be identified.

Alternatively to impedance data, the DRT analysis can also be applied on time-series data obtained by pulse measurements. Pulse tests differ from impedance spectroscopy by applying a non-sinusoidal current or voltage perturbation, typically in form of a short pulse, enabling the characterization of processes with higher time constants, such as solid-state diffusion in intercalation electrode materials.

Impedance data validation: To ensure accurate processing and a reliable and meaningful analysis of impedance spectra, it is important to check the adherence to the criteria proposed for linear time-invariant systems, including linearity, stability and stationarity, as well as causality. This is of major importance, as every electrochemical system is highly nonlinear and dependent on various internal and external states, which increases the likelihood of violating the aforementioned criteria during the measurement. Because the DRT analysis, but also the commonly used equivalent circuit modeling, requires a linear and time-invariant system, it is mandatory to check the measurement data's validity. For this purpose the extended Kramers–Kronig test and the Z-HIT transformation can be used. While both methods are based on different principles, they provide a reconstruction of the input data, thus allowing the qualitative and quantitative analysis of the residuals. From this, metrics have been designed to quantitatively assess the compliance of the experimental impedance data with the LTI criteria, offering scores from 0% to 100%. These metrics are based on the residuals and probabilistic distances. The most straightforward approach is to check for the presence of systematic errors, which manifest as drifts from the 0% baseline and high statistical deviations. As a rule of thumb, the error should be lower than 1%.

Calculation of the distribution of relaxation times: The distribution of relaxation times analysis is a method that deconvolutes frequency domain data, or in specific cases time domain data, into a distribution of relaxation times in the time domain. This can be mathematically described by a Fredholm integral of first kind. This problem is widespread and can be found in various fields, like physics, geology or biophysics. It is known to be an inverse and ill-posed problem, meaning that many solutions exist that well approximate the data. For the deconvolution of time constants, there exist different kinds of solution methods, which can be classified into discretization and regularization based approaches, probabilistic methods, and purely

data-driven algorithms. In specific cases, where the transfer function is known and is suitable, an analytical direct inversion can be found by using a special transformation published by Kirkwood and Fouss. For each category, the most common methods are presented in this review and their unique challenges and benefits are discussed. In general, it is important to be transparent in the chosen meta-parameters of the analysis method, as they can have a non-neglectable influence on the result. For the discretization approach in form of the presented gDRT, the Tikhonov regularization is applied to reduce possible solutions and achieve a meaningful result. However, the regularization parameter has a crucial impact on the resulting distribution function and must therefore be always shown with the return. This also holds true for chosen number of time constants and their selected limits, even if their influence is much smaller. The pendant for the presented data-driven Loewner method is the selected model order for the model reduction.

Regardless of the selected solution method, a distribution function consisting of peaks is obtained. While the Loewner method provides gains with distinct time constants in form of scaled Dirac impulses, the gDRT analysis and their derivatives as well as the probabilistic method results in a discrete distribution.

Post-processing and interpretation: In most cases, it requires a post-processing step to identify and enumerate the present peaks. For this, the first- and second derivative and/or the curvature is used for identification and a subsequent peak fitting can be used to quantify the polarization contribution by calculating the areas of the single peaks. For the model-based peak analysis two functions are reasonable: a Gaussian bell curve and a RQ-distribution. The latter can be found by the aforementioned direct inversion of the transfer function of an RQ element, which is often used for representing distributed resistive–capacitive processes. Both presented peak models have distinct advantages and disadvantages and their application depends on the use case. Gaussian peaks are more adaptable but do not provide direct electrochemical properties as the less flexible RQ distribution does.

Peak interpretation in the context of solid-state diffusion reveals an increasing series of peaks that is not solely induced by the chosen regularization technique, but is intrinsic to the typically observed straight-line slope in the impedance spectrum. Recognizing these challenges is critical when performing peak analysis to ensure a reliable and meaningful interpretation. The results can also be used to derive model assumptions on the system to adopt a justified equivalent circuit model whose initial parameters can be estimated using DRT analysis.

In summary, distribution of relaxation times analysis provides a valuable and largely model-free approach to deconvolving frequency domain data into a distribution of relaxation times function in the time domain, providing improved spectral resolution and separability of electrochemical processes compared to classical equivalent circuit modeling. The use of DRT can lead to valuable insights into the complex behavior of electrochemical systems, especially when dealing with distributed processes, and its application holds great promise for advancing the understanding and characterization of various electrochemical phenomena at different scales, ranging from material and cell to module and system level.

CRediT authorship contribution statement

Christian Plank: Conceptualization, Methodology, Software, Investigation, Data curation, Writing – original draft, Writing – review & editing, Visualization. **Tom Rüther:** Conceptualization, Methodology, Software, Investigation, Data curation, Writing – original draft, Writing – review & editing. **Leonard Jahn:** Investigation, Writing – original draft, Writing – review & editing. **Maximilian Schamel:** Investigation, Writing – original draft, Writing – review & editing. **Jan Philipp Schmidt:** Conceptualization, Writing – original draft, Writing – review & editing, Supervision. **Francesco Ciucci:** Conceptualization, Writing – original draft, Writing – review & editing, Supervision. **Michael A. Danzer:** Conceptualization, Writing – original draft, Writing – review & editing, Supervision.

Declaration of competing interest

The authors declare that they have no known competing financial interests or personal relationships that could have appeared to influence the work reported in this paper.

Data availability

Acknowledgments

Funding

Appendix A. Equation systems for gDRT, tDRT and eKKT

A.1. eKKT

To avoid the need of the optimization of a complex system of equations and allow the usage of a very efficient linear-least-squares algorithm, the problem must be decomposed into its real and imaginary components. Due to the presence of lumped elements, calculations based on either the real or imaginary part alone are not possible. To solve this, the transfer function of the RC element, together with the measurement data, must be separated into their respective real and imaginary parts. Consequently, the system matrix will have a size of $2 \cdot (N_f) \times (N_\tau + 3)$, where N_f is the number of measured frequencies and N_τ is the number of preselected and logarithmically distributed time constants plus the three lumped elements R_0, L_0 and C_0. This leads to the following definition:

$$\begin{bmatrix} m_{\mathrm{Re},1,1} & \cdots & m_{\mathrm{Re},1,N_\tau} & 1 & 0 & 0 \\ \vdots & \ddots & \vdots & \vdots & \vdots & \vdots \\ m_{\mathrm{Re},N_f,1} & \cdots & m_{\mathrm{Re},N_f,N_\tau} & 1 & 0 & 0 \\ m_{\mathrm{Im},1,1} & \cdots & m_{\mathrm{Im},1,N_\tau} & 0 & \omega_1 & -\frac{1}{\omega_1} \\ \vdots & \ddots & \vdots & \vdots & \vdots & \vdots \\ m_{\mathrm{Im},N_f,1} & \cdots & m_{\mathrm{Im},N_f,N_\tau} & 0 & \omega_{N_f} & -\frac{1}{\omega_{N_f}} \end{bmatrix} \cdot \begin{bmatrix} h_{\mathrm{RC},1} \\ \vdots \\ h_{\mathrm{RC},N_\tau} \\ R_0 \\ L_0 \\ \hat{C}_0 \end{bmatrix} = \begin{bmatrix} \mathrm{Re}\{Z_1\} \\ \vdots \\ \mathrm{Re}\{Z_{N_f}\} \\ \mathrm{Im}\{Z_1\} \\ \vdots \\ \mathrm{Im}\{Z_{N_f}\} \end{bmatrix} \quad (\mathrm{A.1})$$

$$\begin{bmatrix} \mathbf{M}_{\mathrm{Re}} & \mathbf{P}_{\mathrm{Re}} \\ \mathbf{M}_{\mathrm{Im}} & \mathbf{P}_{\mathrm{Im}} \end{bmatrix} \cdot \begin{bmatrix} \mathbf{h}_{\mathrm{RC}} \\ \mathbf{x}_{\mathrm{P}} \end{bmatrix} = \begin{bmatrix} \mathbf{Z}_{\mathrm{Re}} \\ \mathbf{Z}_{\mathrm{Im}} \end{bmatrix} \quad (\mathrm{A.2})$$

$$\mathbf{A}_{\mathrm{eKKT}} \cdot \mathbf{x}_{\mathrm{eKKT}} = \mathbf{Z} \quad (\mathrm{A.3})$$

with the system submatrix M for the resistive–capacitive distribution and the system sub matrix P for the lumped elements. To be able to

represent the system in matrix vector form, the optimization parameter of the capacitance C_0 has to be inverted:

$$\hat{C}_0 = \frac{1}{C_0} \tag{A.4}$$

The transfer function of an RC element separates into its real part

$$m_{\text{Re},i,k} = \frac{1}{1 + (\omega_i \tau_k)^2} \tag{A.5}$$

and its corresponding imaginary part:

$$m_{\text{Im},i,k} = -\frac{\omega_i \tau_k}{1 + (\omega_i \tau_k)^2}. \tag{A.6}$$

The presented system of equations can either be used for the extended Kramers–Kronig test (see Section 4.4.1) or the extended DRT analysis (see Section 2.2.1). Both require some sort of regularization technique to find a physically meaningful interpretation (see Section 2.2.3). Compared to the regular DRT analysis, which is usually restricted to positive values, the Kramers–Kronig test is unrestricted, allowing the representation of resistive–capacitive and resistive–inductive effects in one distribution function. As (46) indicates, this is possible due to the fact that the transfer function of a resistive–inductive element can be represented by inserting the negative resistance in the transfer function of an resistive–capacitive element plus an ohmic offset as compensation.

A.2. gDRT

For the generalized DRT analysis (gDRT), a second distribution for resistive–inductive effects is added. Compared to the derivation of the equation system for the eKKT/eDRT, there are no further differences:

$$\left[\left[\begin{matrix} \mathbf{M}_{\text{Re}} \end{matrix}\right] \left[\begin{matrix} n_{\text{Re},1,1} & \cdots & n_{\text{Re},1,N_\tau} \\ \vdots & \ddots & \vdots \\ n_{\text{Re},N_f,1} & \cdots & n_{\text{Re},N_f,N_\tau} \end{matrix}\right] \left[\begin{matrix} \mathbf{P}_{\text{Re}} \end{matrix}\right] \\ \left[\begin{matrix} \mathbf{M}_{\text{Im}} \end{matrix}\right] \left[\begin{matrix} n_{\text{Im},1,1} & \cdots & n_{\text{Im},1,N_\tau} \\ \vdots & \ddots & \vdots \\ n_{\text{Im},N_f,1} & \cdots & n_{\text{Im},N_f,N_\tau} \end{matrix}\right] \left[\begin{matrix} \mathbf{P}_{\text{Im}} \end{matrix}\right]\right] \cdot \left[\begin{matrix} \mathbf{h}_{\text{RC}} \\ h_{\text{RL},1} \\ \vdots \\ h_{\text{RL},N_\tau} \\ \mathbf{x}_{\text{P}} \end{matrix}\right] = \left[\begin{matrix} \mathbf{Z}_{\text{Re}} \\ \mathbf{Z}_{\text{Im}} \end{matrix}\right] \tag{A.7}$$

$$\left[\begin{matrix} \mathbf{M} & \mathbf{N} & \mathbf{P} \end{matrix}\right] \cdot \left[\begin{matrix} \mathbf{h}_{\text{RC}} \\ \mathbf{h}_{\text{RL}} \\ \mathbf{x}_{\text{P}} \end{matrix}\right] = \mathbf{Z} \tag{A.8}$$

$$\mathbf{A}_{\text{gDRT}} \cdot \mathbf{x}_{\text{gDRT}} = \mathbf{Z} \tag{A.9}$$

The resulting system matrix for the gDRT is composed of the system submatrix M for the resistive–capacitive distribution, the system submatrix N for the resistive–inductive distribution and the system sub matrix P for the lumped elements. For the second distribution $\mathbf{h}_{\text{RL}}$, the kernel is swapped from the transfer function of an RC element to the transfer function of an RL element. To implement it in the system which is split into real and imaginary part, the transfer function has to be split into its real part

$$n_{\text{Re},i,k} = \frac{(\omega_i \tau_k)^2}{1 + (\omega_i \tau_k)^2} \tag{A.10}$$

and its imaginary part

$$n_{\text{Im},i,k} = \frac{\omega_i \tau_k}{1 + (\omega_i \tau_k)^2}. \tag{A.11}$$

A.3. tDRT

The equation system for the time domain DRT analysis (tDRT) can be derived as follows:

$$\left[\begin{matrix} g_{1,1} & \cdots & g_{1,N_\tau} & I_{\text{P}} & 1 \\ \vdots & \ddots & \vdots & \vdots & \vdots \\ g_{N_t,1} & \cdots & g_{N_t,N_\tau} & 0 & 1 \end{matrix}\right] \cdot \left[\begin{matrix} h_{\text{RC},1} \\ \vdots \\ h_{\text{RC},N_\tau} \\ R_0 \\ U_{\text{OCV}} \end{matrix}\right] = \left[\begin{matrix} U_1 \\ \vdots \\ U_{N_t} \end{matrix}\right] \tag{A.12}$$

$$\left[\left[\begin{matrix} \mathbf{G} \end{matrix}\right] \begin{matrix} I_{\text{P}} & 1 \\ \vdots & \vdots \\ 0 & 1 \end{matrix}\right] \cdot \left[\begin{matrix} \mathbf{h}_{\text{RC}} \\ R_0 \\ U_{\text{OCV}} \end{matrix}\right] = \mathbf{U} \tag{A.13}$$

$$\mathbf{A}_{\text{tDRT}} \cdot \mathbf{x}_{\text{tDRT}} = \mathbf{U} \tag{A.14}$$

The coefficients $g_{i,k}$ of the sub-matrix $\mathbf{G}$ are defined with:

$$g_{i,k} = I_{\text{P}} \left(\left(1 - e^{\frac{-t_i}{\tau_k}} \right) - \left(1 - e^{\frac{-(t_i - t_d)}{\tau_k}} \right) \right) \tag{A.15}$$

where i is the nth sampling point corresponding to time t_i and k is the nth RC-element in the sum and thus defining the time constant τ_k. By removing the step-functions we assume that the time when the pulse was applied is $t = 0$ and the time when the current was stopped is $t = t_d$ and only values for $t > 0$ may be considered. The vector $\mathbf{U}$ contains the measured cell voltages U_i at the sampling times t_i.

The resulting system matrix $\mathbf{A}_{\text{tDRT}}$ contains the sub-matrix $\mathbf{G}$ as well as the entries for the open-circuit-potential U_{OCV} and the ohmic drop induced by the lumped resistance R_0 and the current of the pulse I_{P}.

A.4. cDRT

The equation system for the combined DRT analysis (cDRT) is a combination of both, the tDRT and the gDRT, to allow the fusion of frequency- and time domain data in a single system of equations. It is defined as follows:

$$\left[\begin{matrix} \left[\begin{matrix} \mathbf{M}_{\text{Re}} \end{matrix}\right] & \left[\begin{matrix} \mathbf{N}_{\text{Re}} \end{matrix}\right] & \left[\begin{matrix} \mathbf{P}_{\text{Re}} \end{matrix}\right] & \begin{matrix} 0 \\ \vdots \\ 0 \end{matrix} \\ \left[\begin{matrix} \mathbf{M}_{\text{Im}} \end{matrix}\right] & \left[\begin{matrix} \mathbf{M}_{\text{Im}} \end{matrix}\right] & \left[\begin{matrix} \mathbf{P}_{\text{Im}} \end{matrix}\right] & \begin{matrix} 0 \\ \vdots \\ 0 \end{matrix} \\ \left[\begin{matrix} \mathbf{G} \end{matrix}\right] & \left[\begin{matrix} \mathbf{0} \end{matrix}\right] & \begin{matrix} I_{\text{P}} & 0 & 0 & 1 \\ \vdots & \vdots & \vdots & \vdots \\ 0 & 0 & 0 & 1 \end{matrix} \end{matrix}\right] \cdot \left[\begin{matrix} \mathbf{h}_{\text{RC}} \\ \mathbf{h}_{\text{RL}} \\ \mathbf{x}_{\text{P}} \\ U_{\text{OCV}} \end{matrix}\right] = \left[\begin{matrix} \mathbf{Z}_{\text{Re}} \\ \mathbf{Z}_{\text{Im}} \\ \hline \mathbf{U} \end{matrix}\right] \tag{A.16}$$

$$\mathbf{A}_{\text{cDRT}} \cdot \mathbf{x}_{\text{cDRT}} = \left[\begin{matrix} \mathbf{Z} \\ \mathbf{U} \end{matrix}\right] \tag{A.17}$$

To increase robustness and improve the results, an implementation of a weighting for pulse data and the overlapping data range between pulse and impedance data is recommended. In this work a linear decline in the overlapping range was used or both datasets.

Since the different versions of the system of equations represent an ill-posed inversion problem, it is necessary to apply a regularization technique or something similar in order to obtain a meaningful solution. In this paper, the Tikhonov L2 regularization with a single regularization parameter is used. Details can be found in Sections 2.2.1 and 2.2.3.

Appendix B. Analysis of Warburg and Gerischer diffusion with gDRT analysis

The presence of diffusion processes in the spectrum results in a distinct peak pattern in the gDRT analysis. Depending the ongoing electrochemical reaction, the boundaries and the coupling with the diffusion phenomenon, diffusion in batteries and fuel cells is typically modeled by different types of Warburg or Gerischer diffusion. The diffusion represented by a finite-space Warburg (FSW) element with the equation

$$Z_{\text{FSW}}(\omega) = Z_0 (j\omega\tau_0)^{-0.5} \coth(j\omega\tau_0)^{0.5} \tag{B.1}$$

is often found in battery spectra, while for the gas diffusion layer in fuel cells, researches either assume a Gerischer type of diffusion or a finite-length Warburg (FLW) element. Its transfer function is defined as
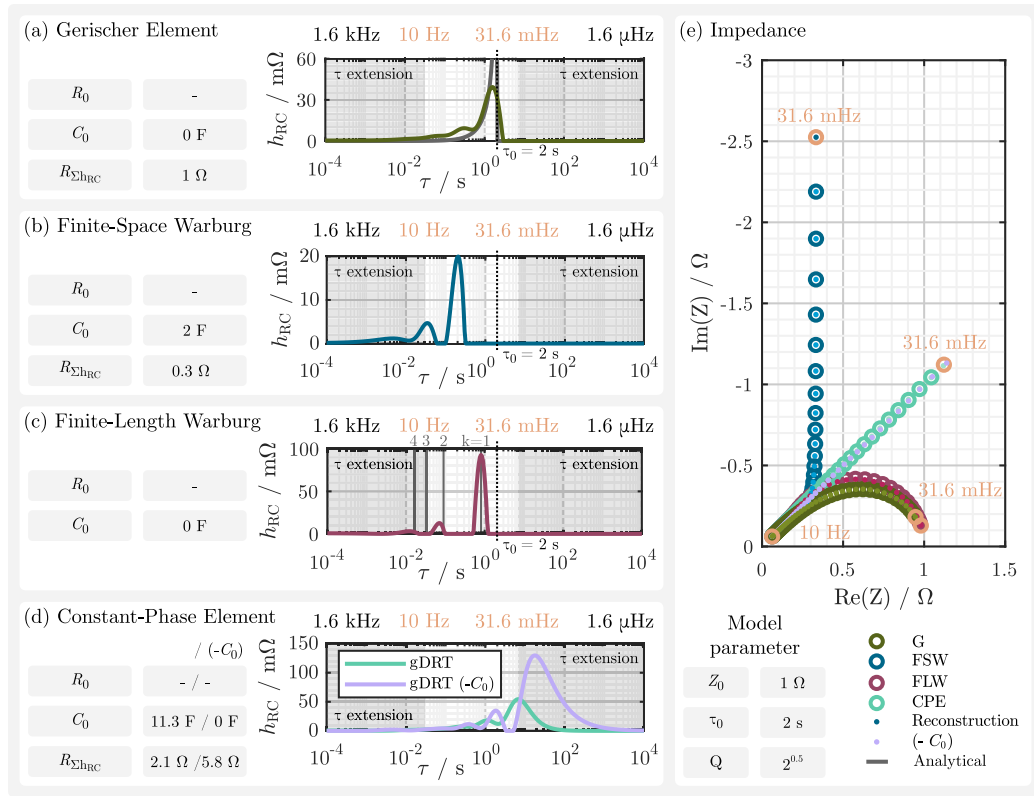
Fig. B.9. Analysis of different branches of the Warburg element and the Gerischer element with the gDRT method with $\lambda = 0.1$ and $N_\tau = 300$. For the Gerischer and the finite-length Warburg the analytical distributions functions are depicted in gray. Please note, that for a better visual comparison, only the time constants for the finite-length Warburg are marked. (a) Distribution function and lumped parameters for the Gerischer element. (b) Distribution function and lumped parameters for the finite-space Warburg. (c) Distribution function and lumped parameters for the finite-length Warburg. (d) Distribution function and lumped parameters for the semi-infinite Warburg or respectively a CPE with $\varphi = 0.5$. Compared for gDRT with the capacitance C_0 and without. (e) Comparison of the simulated impedances with the reconstructed impedance for the different Warburg types as well as the Gerischer element.

follows:

$$Z_{\text{FLW}}(\omega) = Z_0(j\omega\tau_0)^{-0.5}\tanh(j\omega\tau_0)^{0.5} \qquad (B.2)$$

Boukamp has derived an analytical expression for the distribution function of an FLW element [107]. He showed that it consists of an infinite sum of time constants of ideal RC elements, which correspond to Dirac impulses in the distribution function. The time constants and polarization contributions for $k \in 1, 2, \ldots, \infty$ are defined as follows:

$$h_{\text{FLW,k}}(k) = \frac{2Z_0\tau_0}{\pi^2(k - 0.5)^2} \qquad (B.3)$$

$$\tau_{\text{FLW,k}}(k) = \frac{h_{\text{FLW,k}}(k)}{2Z_0} \qquad (B.4)$$

Due to the limited measurement range, in many cases only the sloped straight incline is observable, which can be described by either a semi-infinite Warburg (SIW) element or a constant phase element (CPE) element with $\varphi = 0.5$ and the Warburg coefficient A_{W}:

$$Z_{\text{SIW}}(\omega) = \frac{A_{\text{W}}}{(\omega)^{0.5}} - j\frac{A_{\text{W}}}{(\omega)^{0.5}} = \frac{\sqrt{2}A_{\text{W}}}{(j\omega)^{0.5}} = \frac{1}{Q(j\omega)^{0.5}} = Z_{\text{CPE}}(\omega, \varphi = 0.5) \qquad (B.5)$$

For the Gerischer type of diffusion, the transfer function is defined as:

$$Z_{\text{G}}(\omega) = Z_0(1 + j\omega\tau_0)^{-0.5} \qquad (B.6)$$

Derived from the definition given by Boukamp [193], the analytical distribution function for the Gerischer can be calculated. It is continuous, but only defined for $\tau < \tau_0$ and set to 0 for $\tau \geq \tau_0$ [193]:

$$h_{\text{RC,G}}(\tau) = \frac{2}{\tau_0}\frac{Z_0}{\pi}\sqrt{\frac{\tau}{\tau_0 - \tau}} \qquad (B.7)$$

Fig. B.9 shows the resulting distribution functions for the previously introduced types of Warburg diffusion. The gDRT analysis accurately represents each Warburg branch in the Nyquist plot, at least within the given frequency range. This validation is supported by elements for which an analytical distribution can be calculated. In the case of the Gerischer element, the resulting distribution closely matches the analytical distribution. The characteristic time constant found by the gDRT method is shifted slightly to lower values due to the applied regularization. Regarding the FLW element, the primary time constant is correctly identified, but the detection of secondary peaks depends on the regularization parameter. Higher values of this parameter tend to smooth out subsequent peaks, resulting in incorrect time constants. Conversely, a lower regularization parameter improves the ability to separate and locate the smaller side peaks. While the FSW requires a lumped capacitance C_0 to reconstruct the transfer function, the FLW is characterized without it, as indicated by $C_0 = 0$. The SIW can theoretically be modeled by both variants, but they start to differ when extrapolated in frequency, as shown in Fig. B.10. Depending on the capacitance, the extrapolation follows the behavior of either an FLW (for $C_0 = 0$) or an FSW (for $C_0 > 0$), limiting the validity of both
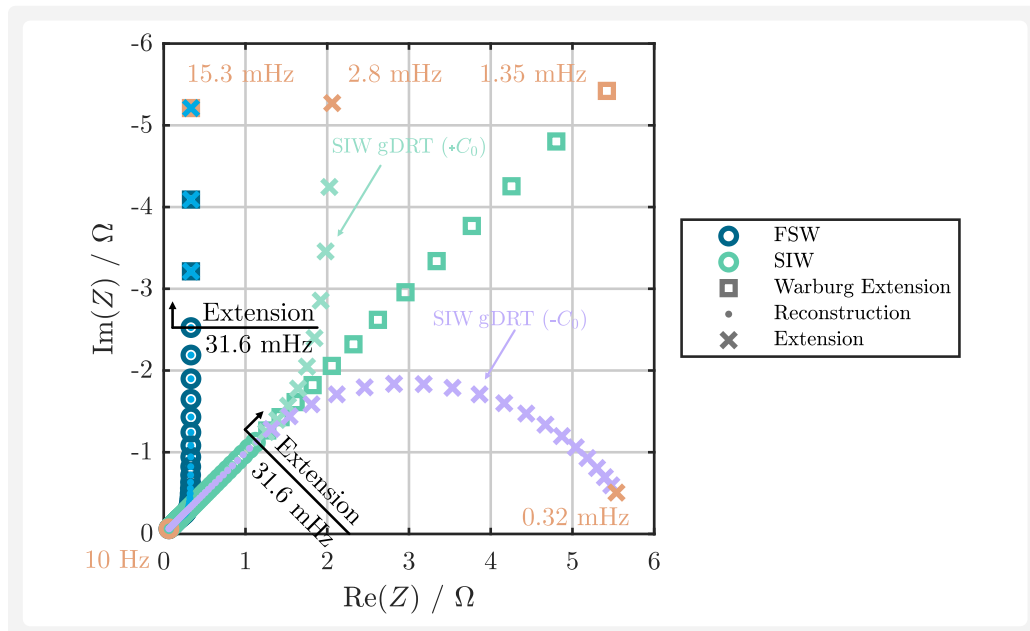
Fig. B.10. Comparison of the extrapolated reconstruction obtained by the distribution function of the gDRT analysis for FSW and SIW Warburg elements. The frequency range for the simulation of the input impedance is in the range of $31.6\,\text{mHz}$ and $10\,\text{Hz}$. For the extrapolation the lower frequency limit is extended to $0.32\,\text{mHz}$. To allow for a better comparison the results for SIW and FSW are truncated.
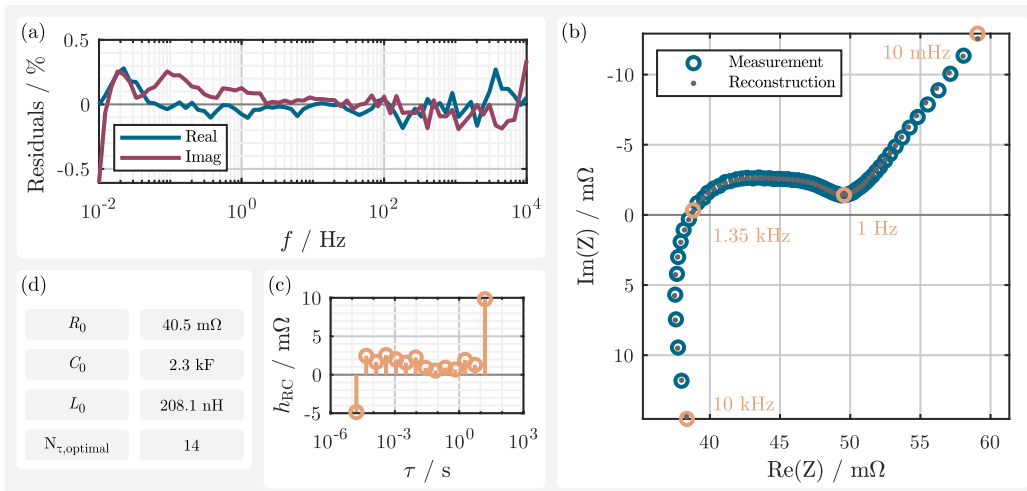
Fig. C.11. Impedance measurement validation of a cylindrical lithium-ion cell from the manufacturer Panasonic with the extended Kramers–Kronig test [184]. (a) Residuals between reconstruction and measurement. (b) Impedance spectrum and reconstruction. (c) Calculated unconstrained distribution function. (d) Lumped eKKT model parameter and optimal number of RC elements determined according to [184].

variants to the input frequency range. On the other hand, the other types of Warburg diffusion can be extrapolated well without losing accuracy over frequency.

The peak series is observed independently of the diffusion variant, although adding the capacitance appears to shift the peak series to lower time constants and reduce the overall polarization of the distribution function. The FLW shows the correct polarization, while the FSW shows the correct capacitance. For the SIW, no obvious correlation can be found for the parameters.

In conclusion, the gDRT method is capable of reconstructing diffusion phenomena, but a quantitative interpretation of the polarization and capacity must be treated with caution, as it strongly depends on the visible part of the diffusion branch and the nature of the underlying diffusion process.

Appendix C. Experimental

Throughout this review, the DRT analysis utilized a publicly available dataset provided by Rüther et al. [98]. The dataset can be accessed in the Bavarian Center for Battery Technology (BayBatt) community at Zenodo for download using the following link: https://doi.org/10.5281/zenodo.8182851.

For the impedance and pulse measurement, cell index 42 was selected.

To validate the measurement data, two methods were applied: the extended Kramers–Kronig test (see Fig. C.11) and the Z-HIT transformation (see Fig. C.12). Both methods confirmed the dataset's validity, providing reliable results for the analysis.
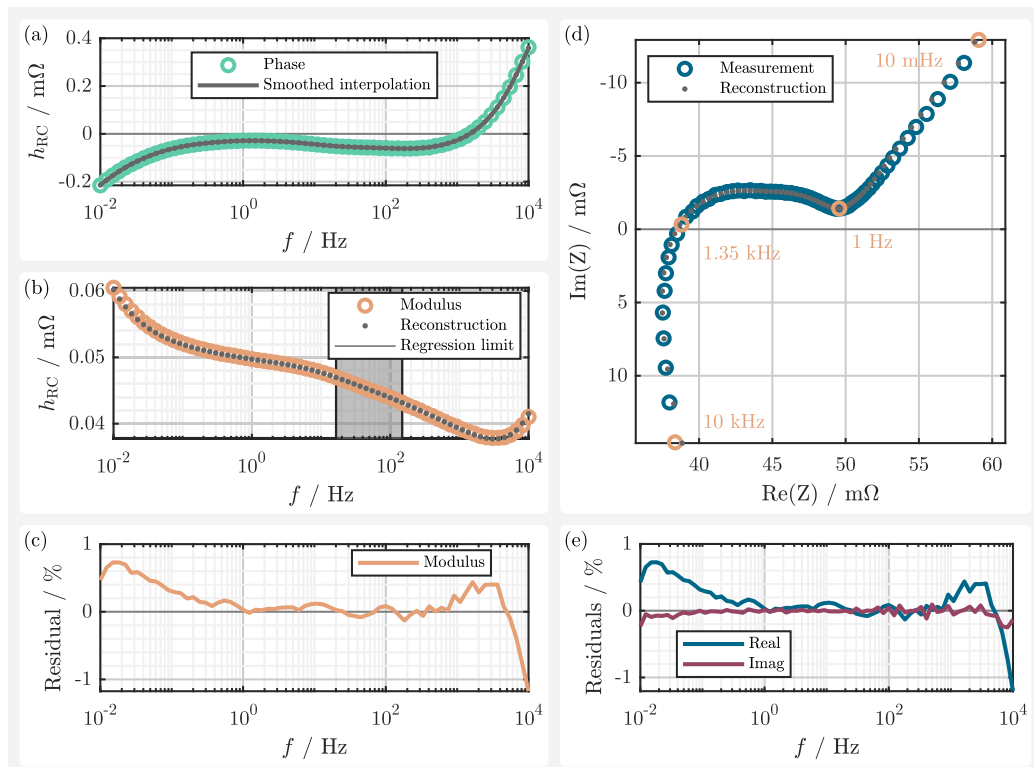
Fig. C.12. Impedance measurement validation of a cylindrical lithium-ion cell from the manufacturer Panasonic with the Z-HIT transformation. (a) Phase of the measurement and the smoothed interpolant function. (b) Measured and reconstructed modulus with the used range of data for the regression optimization. (c) Residuals between the modulus and its reconstruction. (d) Measured and reconstructed impedance in the Nyquist plot. (e) Residuals between the measured and reconstructed impedance.

References

[1] M. Baumann, T. Domnik, M. Haase, C. Wulf, P. Emmerich, C. Rösch, P. Zapp, T. Naegler, M. Weil, Comparative patent analysis for the identification of global research trends for the case of battery storage, hydrogen and bioenergy, Technol. Forecast. Soc. Change 165 (2021) 120505, http://dx.doi.org/10.1016/j.techfore.2020.120505.

[2] L. Qiao, X. Judez, T. Rojo, M. Armand, H. Zhang, Review—Polymer electrolytes for sodium batteries, J. Electrochem. Soc. 167 (7) (2020) 070534, http://dx.doi.org/10.1149/1945-7111/ab7aa0.

[3] J. Ma, Y. Li, N.S. Grundish, J.B. Goodenough, Y. Chen, L. Guo, Z. Peng, X. Qi, F. Yang, L. Qie, C.-A. Wang, B. Huang, Z. Huang, L. Chen, D. Su, G. Wang, X. Peng, Z. Chen, J. Yang, S. He, X. Zhang, H. Yu, C. Fu, M. Jiang, W. Deng, C.-F. Sun, Q. Pan, Y. Tang, X. Li, X. Ji, F. Wan, Z. Niu, F. Lian, C. Wang, G.G. Wallace, M. Fan, Q. Meng, S. Xin, Y.-G. Guo, L.-J. Wan, The 2021 battery technology roadmap, J. Phys. D: Appl. Phys. 54 (18) (2021) 183001, http://dx.doi.org/10.1088/1361-6463/abd353.

[4] G.G. Eshetu, H. Zhang, X. Judez, H. Adenusi, M. Armand, S. Passerini, E. Figgemeier, Production of high-energy Li-ion batteries comprising silicon-containing anodes and insertion-type cathodes, Nat. Commun. 12 (1) (2021) 5459, http://dx.doi.org/10.1038/s41467-021-25334-8.

[5] W. Pantoja, J.A. Perez-Taborda, A. Avila, Tug-of-War in the selection of materials for battery technologies, Batteries 8 (9) (2022) 105, http://dx.doi.org/10.3390/batteries8090105.

[6] L. Gaines, J. Zhang, X. He, J. Bouchard, H.E. Melin, Tracking flows of end-of-life battery materials and manufacturing scrap, Batteries 9 (7) (2023) 360, http://dx.doi.org/10.3390/batteries9070360.

[7] G.D.J. Harper, E. Kendrick, P.A. Anderson, W. Mrozik, P. Christensen, S. Lambert, D. Greenwood, P.K. Das, M. Ahmeid, Z. Milojevic, W. Du, D.J.L. Brett, P.R. Shearing, A. Rastegarpanah, R. Stolkin, R. Sommerville, A. Zorin, J.L. Durham, A.P. Abbott, D. Thompson, N.D. Browning, B.L. Mehdi, M. Bahri, F. Schanider-Tontini, D. Nicholls, C. Stallmeister, B. Friedrich, M. Sommerfeld, L.L. Driscoll, A. Jarvis, E.C. Giles, P.R. Slater, V. Echavarri-Bravo, G. Maddalena, L.E. Horsfall, L. Gaines, Q. Dai, S.J. Jethwa, A.L. Lipson, G.A. Leeke, T. Cowell, J.G. Farthing, G. Mariani, A. Smith, Z. Iqbal, R. Golmohammadzadeh, L. Sweeney, V. Goodship, Z. Li, J. Edge, L. Lander, V.T. Nguyen, R.J.R. Elliot, O. Heidrich, M. Slattery, D. Reed, J. Ahuja, A. Cavoski, R. Lee, E. Driscoll, J. Baker, P. Littlewood, I. Styles, S. Mahanty, F. Boons, Roadmap for a sustainable circular economy in lithium-ion and future battery technologies, J. Phys.: Energy 5 (2) (2023) 021501, http://dx.doi.org/10.1088/2515-7655/acaa57.

[8] J. Neumann, M. Petranikova, M. Meeus, J.D. Gamarra, R. Younesi, M. Winter, S. Nowak, Recycling of lithium–Ion batteries—Current state of the art, circular economy, and next generation recycling, Adv. Energy Mater. 12 (17) (2022) 2102917, http://dx.doi.org/10.1002/aenm.202102917.

[9] N. Meddings, M. Heinrich, F. Overney, J.-S. Lee, V. Ruiz, E. Napolitano, S. Seitz, G. Hinds, R. Raccichini, M. Gaberšček, J. Park, Application of electrochemical impedance spectroscopy to commercial Li-ion cells: A review, J. Power Sources 480 (2020) 228742, http://dx.doi.org/10.1016/j.jpowsour.2020.228742.

[10] A.C. Lazanas, M.I. Prodromidis, Electrochemical impedance spectroscopy - A tutorial, in: ACS Measurement Science Au, 2023, http://dx.doi.org/10.1021/acsmeasuresciau.2c00070{&}ref=pdf.

[11] S. Wang, J. Zhang, O. Gharbi, V. Vivier, M. Gao, M.E. Orazem, Electrochemical impedance spectroscopy, Nat. Rev. Methods Primers 1 (1) (2021) 7158, http://dx.doi.org/10.1038/s43586-021-00039-w.

[12] S. Gantenbein, M. Weiss, E. Ivers-Tiffée, Impedance based time-domain modeling of lithium-ion batteries: Part I, J. Power Sources 379 (2018) 317–327, http://dx.doi.org/10.1016/j.jpowsour.2018.01.043.

[13] J.P. Schmidt, E. Ivers-Tiffée, Pulse-fitting – A novel method for the evaluation of pulse measurements, demonstrated for the low frequency behavior of lithium-ion cells, J. Power Sources 315 (2016) 316–323, http://dx.doi.org/10.1016/j.jpowsour.2016.03.026.

[14] A. Barai, K. Uddin, W.D. Widanage, A. McGordon, P. Jennings, A study of the influence of measurement timescale on internal resistance characterisation methodologies for lithium-ion cells, Sci. Rep. 8 (1) (2018) 21, http://dx.doi.org/10.1038/s41598-017-18424-5.

[15] G.L. Plett, Battery Management Systems: Volume 1: Battery Modeling, in: Artech House Power Engineering and Power Electronics, Artech House, Boston and London, 2015.

[16] E. Barsoukov, J.R. Macdonald (Eds.), Impedance Spectroscopy: Theory, Experiment, and Applications, third ed., Wiley, Hoboken, NJ, 2018.

[17] Z. Chu, G.L. Plett, M.S. Trimboli, M. Ouyang, A control-oriented electrochemical model for lithium-ion battery, Part I: Lumped-parameter reduced-order model with constant phase element, J. Energy Storage 25 (2019) 100828, http://dx.doi.org/10.1016/j.est.2019.100828.

[18] M. Hahn, L. Grüne, C. Plank, F. Katzer, T. Rüther, L. Jahn, M.A. Danzer, Model predictive fast charging control by means of a real-time discrete electrochemical model, J. Energy Storage 42 (2021) 103056, http://dx.doi.org/10.1016/j.est.2021.103056.

[19] S. Kim, D.P. Neikirk, Compact equivalent circuit model for the skin effect, in: 1996 IEEE MTT-S International Microwave Symposium Digest, IEEE, 1996, pp. 1815–1818, http://dx.doi.org/10.1109/MWSYM.1996.512297.

[20] J.J. Adams, J.T. Bernhard, Broadband equivalent circuit models for antenna impedances and fields using characteristic modes, IEEE Trans. Antennas and Propagation 61 (8) (2013) 3985–3994, http://dx.doi.org/10.1109/TAP.2013.2261852.

[21] A.M. Dhirde, N.V. Dale, H. Salehfar, M.D. Mann, T.-H. Han, Equivalent electric circuit modeling and performance analysis of a PEM fuel cell stack using impedance spectroscopy, IEEE Trans. Energy Convers. 25 (3) (2010) 778–786, http://dx.doi.org/10.1109/TEC.2010.2049267.

[22] A. Leonide, Y. Apel, E. Ivers-Tiffee, SOFC modeling and parameter identification by means of impedance spectroscopy, ECS Trans. 19 (20) (2009) 81–109, http://dx.doi.org/10.1149/1.3247567.

[23] J. Illig, M. Ender, A. Weber, E. Ivers-Tiffée, Modeling graphite anodes with serial and transmission line models, J. Power Sources 282 (2015) 335–347, http://dx.doi.org/10.1016/j.jpowsour.2015.02.038.

[24] M.A. Danzer, J. Wilhelm, H. Aschemann, E.P. Hofer, Model-based control of cathode pressure and oxygen excess ratio of a PEM fuel cell system, J. Power Sources 176 (2) (2008) 515–522, http://dx.doi.org/10.1016/j.jpowsour.2007.08.049.

[25] G. Swift, T.S. Molinski, W. Lehn, A fundamental approach to transformer thermal modeling. I. Theory and equivalent circuit, IEEE Trans. Power Deliv. 16 (2) (2001) 171–175, http://dx.doi.org/10.1109/61.915478.

[26] J.P. Schmidt, D. Manka, D. Klotz, E. Ivers-Tiffée, Investigation of the thermal properties of a Li-ion pouch-cell by electrothermal impedance spectroscopy, J. Power Sources 196 (19) (2011) 8140–8146, http://dx.doi.org/10.1016/j.jpowsour.2011.05.047.

[27] S. Nejad, D.T. Gladwin, D.A. Stone, A systematic review of lumped-parameter equivalent circuit models for real-time estimation of lithium-ion battery states, J. Power Sources 316 (2) (2016) 183–196, http://dx.doi.org/10.1016/j.jpowsour.2016.03.042.

[28] M.A. Danzer, Generalized distribution of relaxation times analysis for the characterization of impedance spectra, Batteries 5 (3) (2019) 53, http://dx.doi.org/10.3390/batteries5030053.

[29] E. Goldammer, J. Kowal, Determination of the distribution of relaxation times by means of pulse evaluation for offline and online diagnosis of lithium-ion batteries, Batteries 7 (2) (2021) 36, http://dx.doi.org/10.3390/batteries7020036.

[30] M. Hahn, S. Schindler, L.-C. Triebs, M.A. Danzer, Optimized process parameters for a reproducible distribution of relaxation times analysis of electrochemical systems, Batteries 5 (2) (2019) 43, http://dx.doi.org/10.3390/batteries5020043.

[31] T.P. Heins, N. Schlüter, U. Schröder, Electrode-resolved monitoring of the ageing of large-scale lithium-ion cells by using electrochemical impedance spectroscopy, ChemElectroChem 4 (11) (2017) 2921–2927, http://dx.doi.org/10.1002/celc.201700686.

[32] Y. Lu, C.-Z. Zhao, J.-Q. Huang, Q. Zhang, The timescale identification decoupling complicated kinetic processes in lithium batteries, Joule 6 (6) (2022) 1172–1198, http://dx.doi.org/10.1016/j.joule.2022.05.005.

[33] Y. Zhao, V. Kumtepeli, S. Ludwig, A. Jossen, Investigation of the distribution of relaxation times of a porous electrode using a physics-based impedance model, J. Power Sources 530 (1) (2022) 231250, http://dx.doi.org/10.1016/j.jpowsour.2022.231250.

[34] Y. Zhao, S. Kücher, A. Jossen, Investigation of the diffusion phenomena in lithium-ion batteries with distribution of relaxation times, Electrochim. Acta 432 (2022) 141174, http://dx.doi.org/10.1016/j.electacta.2022.141174, URL https://www.sciencedirect.com/science/article/pii/S0013468622013317.

[35] A. Schiefer, M. Heinzmann, A. Weber, Inductive low–frequency processes in PEMFC–Impedance spectra, Fuel Cells 20 (4) (2020) 499–506, http://dx.doi.org/10.1002/fuce.201900212.

[36] I. Pivac, B. Šimić, F. Barbir, Experimental diagnostics and modeling of inductive phenomena at low frequencies in impedance spectra of proton exchange membrane fuel cells, J. Power Sources 365 (2017) 240–248, http://dx.doi.org/10.1016/j.jpowsour.2017.08.087.

[37] K.S. Cole, R.H. Cole, Dispersion and absorption in dielectrics I. Alternating current characteristics, J. Chem. Phys. 9 (4) (1941) 341–351, http://dx.doi.org/10.1063/1.1750906.

[38] A. Lasia, The origin of the constant phase element, J. Phys. Chem. Lett. 13 (2) (2022) 580–589, http://dx.doi.org/10.1021/acs.jpclett.1c03782.

[39] A. Jossen, Fundamentals of battery dynamics, J. Power Sources 154 (2) (2006) 530–538, http://dx.doi.org/10.1016/j.jpowsour.2005.10.041.

[40] C. Fleischer, W. Waag, H.-M. Heyn, D.U. Sauer, On-line adaptive battery impedance parameter and state estimation considering physical principles in reduced order equivalent circuit battery models, J. Power Sources 260 (2014) 276–291, http://dx.doi.org/10.1016/j.jpowsour.2014.01.129.

[41] P. Mauracher, E. Karden, Dynamic modelling of lead/acid batteries using impedance spectroscopy for parameter identification, J. Power Sources 67 (1–2) (1997) 69–84, http://dx.doi.org/10.1016/S0378-7753(97)02498-1.

[42] M. Kunaver, Ž. Rojec, V. Subotić, S. Pereverzyev, M. Žic, Extraction of distribution function of relaxation times by using DRT-RBLM tools: A new approach to combine levenberg-marquardt algorithm and radial basis functions for discretization basis, J. Electrochem. Soc. 169 (11) (2022) 110529, http://dx.doi.org/10.1149/1945-7111/ac9a83.

[43] B.A. Boukamp, Distribution (function) of relaxation times, successor to complex nonlinear least squares analysis of electrochemical impedance spectroscopy? J. Phys.: Energy 2 (4) (2020) 042001, http://dx.doi.org/10.1088/2515-7655/aba9e0.

[44] J. Liu, F. Ciucci, The Gaussian process distribution of relaxation times: A machine learning tool for the analysis and prediction of electrochemical impedance spectroscopy data, Electrochim. Acta 331 (2020) 135316, http://dx.doi.org/10.1016/j.electacta.2019.135316, URL https://www.sciencedirect.com/science/article/pii/S0013468619321887.

[45] A. Maradesa, B. Py, E. Quattrocchi, F. Ciucci, The probabilistic deconvolution of the distribution of relaxation times with finite Gaussian processes, Electrochim. Acta 413 (2022) 140119, http://dx.doi.org/10.1016/j.electacta.2022.140119, URL https://www.sciencedirect.com/science/article/pii/S0013468622002912.

[46] F. Dion, A. Lasia, The use of regularization methods in the deconvolution of underlying distributions in electrochemical processes, J. Electroanal. Soc. 475 (1) (1999) 28–37, http://dx.doi.org/10.1016/S0022-0728(99)00334-4.

[47] S. Dierickx, A. Weber, E. Ivers-Tiffée, How the distribution of relaxation times enhances complex equivalent circuit models for fuel cells, Electrochim. Acta 355 (2020) 136764, http://dx.doi.org/10.1016/j.electacta.2020.136764.

[48] P.C. Hansen (Ed.), Discrete Inverse Problems, Society for Industrial and Applied Mathematics, 2010, http://dx.doi.org/10.1137/1.9780898718836.

[49] H. Schichlein, A.C. Müller, M. Voigts, A. Krügel, E. Ivers-Tiffée, Deconvolution of electrochemical impedance spectra for the identification of electrode reaction mechanisms in solid oxide fuel cells, J. Appl. Electrochem. 32 (8) (2002) 875–882, http://dx.doi.org/10.1023/A:1020599525160, URL https://link.springer.com/article/10.1023/a:1020599525160.

[50] K. Liedermann, The calculation of a distribution of relaxation times from the frequency dependence of the real permittivity with the inverse Fourier transformation, J. Non-Cryst. Solids 175 (1) (1994) 21–30, http://dx.doi.org/10.1016/0022-3093(94)90311-5.

[51] E. Quattrocchi, B. Py, A. Maradesa, Q. Meyer, C. Zhao, F. Ciucci, Deconvolution of electrochemical impedance spectroscopy data using the deep-neural-network-enhanced distribution of relaxation times, Electrochim. Acta 439 (2023) 141499, http://dx.doi.org/10.1016/j.electacta.2022.141499, URL https://www.sciencedirect.com/science/article/pii/S0013468622016565.

[52] E. Quattrocchi, T.H. Wan, A. Belotti, D. Kim, S. Pepe, S.V. Kalinin, M. Ahmadi, F. Ciucci, The deep-DRT: A deep neural network approach to deconvolve the distribution of relaxation times from multidimensional electrochemical impedance spectroscopy data, Electrochim. Acta 392 (2021) 139010, http://dx.doi.org/10.1016/j.electacta.2021.139010, URL https://www.sciencedirect.com/science/article/pii/S0013468621013001.

[53] T. Horlin, Maximum entropy in impedance spectroscopy of non-inductive systems, Solid State Ion. 67 (1–2) (1993) 85–96, http://dx.doi.org/10.1016/0167-2738(93)90313-R.

[54] D. Calvetti, E. Somersalo, Inverse problems: From regularization to Bayesian inference, WIREs Comput. Stat. 10 (3) (2018) e1427, http://dx.doi.org/10.1002/wics.1427.

[55] F. Ciucci, The Gaussian process Hilbert transform (GP-ht): Testing the consistency of electrochemical impedance spectroscopy data, J. Electrochem. Soc. 167 (12) (2020) 126503, http://dx.doi.org/10.1149/1945-7111/aba937.

[56] T.G. Bergmann, N. Schlüter, Introducing alternative algorithms for the determination of the distribution of relaxation times, Chemphyschem 23 (13) (2022) e202200012, http://dx.doi.org/10.1002/cphc.202200012.

[57] T. Rüther, I.V. Gosea, L. Jahn, A.C. Antoulas, M.A. Danzer, Introducing the loewner method as a data-driven and regularization-free approach for the distribution of relaxation times analysis of lithium-ion batteries, Batteries 9 (2) (2023) 132, http://dx.doi.org/10.3390/batteries9020132.

[58] A.C. Antoulas, S. Lefteriu, A.C. Ionita, Chapter 8: A tutorial introduction to the loewner framework for model reduction, in: P. Benner, M. Ohlberger, A. Cohen, K. Willcox (Eds.), Model Reduction and Approximation, Society for Industrial and Applied Mathematics, Philadelphia, PA, 2017, pp. 335–376, http://dx.doi.org/10.1137/1.9781611974829.ch8.

[59] P. Iurilli, C. Brivio, V. Wood, Detection of lithium–Ion cells' degradation through deconvolution of electrochemical impedance spectroscopy with distribution of relaxation time, Energy Technol. (2022) 2200547, http://dx.doi.org/10.1002/ente.202200547.

[60] P. Shafiei Sabet, D.U. Sauer, Separation of predominant processes in electrochemical impedance spectra of lithium-ion batteries with nickel-manganese-cobalt cathodes, J. Power Sources 425 (2019) 121–129, http://dx.doi.org/10.1016/j.jpowsour.2019.03.068.

[61] T.H. Wan, M. Saccoccio, C. Chen, F. Ciucci, Influence of the discretization methods on the distribution of relaxation times deconvolution: Implementing radial basis functions with DRTtools, Electrochim. Acta 184 (2015) 483–499, http://dx.doi.org/10.1016/j.electacta.2015.09.097.

[62] R.M. Fuoss, J.G. Kirkwood, Electrical properties of solids. VIII. Dipole moments in polyvinyl chloride-diphenyl systems *, J. Am. Chem. Soc. 63 (2) (1941) 385–394, http://dx.doi.org/10.1021/ja01847a013.

[63] H. Keiter, M. Rosenberg, On the probability distributions of relaxation times in glasses, Eur. Phys. J. B 5 (3) (1998) 599–603, http://dx.doi.org/10.1007/s100510050484.

[64] M.F. Rosenberg, Untersuchungen Zum Phänomenologischen Ansatz Der Dielektrizitätsfunktion Polarer Amorpher Systeme Oder Die Regularisierung Eines Exponentiell Schlecht Gestellten Problems (Ph.D. thesis), Technische Universität Dortmund, Dortmund, 2002, http://dx.doi.org/10.17877/DE290R-14808.

[65] M. Hahn, D. Rosenbach, A. Krimalowski, T. Nazarenus, R. Moos, M. Thelakkat, M.A. Danzer, Investigating solid polymer and ceramic electrolytes for lithium-ion batteries by means of an extended Distribution of Relaxation Times analysis, Electrochim. Acta 344 (2020) 136060, http://dx.doi.org/10.1016/j.electacta.2020.136060.

[66] L. Wildfeuer, P. Gieler, A. Karger, Combining the distribution of relaxation times from EIS and time-domain data for parameterizing equivalent circuit models of lithium-ion batteries, Batteries 7 (3) (2021) 52, http://dx.doi.org/10.3390/batteries7030052.

[67] D. Klotz, M. Schönleber, J.P. Schmidt, E. Ivers-Tiffée, New approach for the calculation of impedance spectra out of time domain data, Electrochim. Acta 56 (24) (2011) 8763–8769, http://dx.doi.org/10.1016/j.electacta.2011.07.096.

[68] K. Takano, K. Nozaki, Y. Saito, K. Kato, A. Negishi, Impedance spectroscopy by voltage-step chronoamperometry using the Laplace transform method in a lithium-ion battery, J. Electrochem. Soc. 147 (3) (2000) 922, http://dx.doi.org/10.1149/1.1393293.

[69] X. Wang, Y. Kou, B. Wang, Z. Jiang, X. Wei, H. Dai, Fast calculation of broadband battery impedance spectra based on S transform of step disturbance and response, IEEE Trans. Transp. Electr. 8 (3) (2022) 3659–3672, http://dx.doi.org/10.1109/TTE.2022.3153680.

[70] Y. Hoshi, N. Yakabe, K. Isobe, T. Saito, I. Shitanda, M. Itagaki, Wavelet transformation to determine impedance spectra of lithium-ion rechargeable battery, J. Power Sources 315 (2016) 351–358, http://dx.doi.org/10.1016/j.jpowsour.2016.03.048.

[71] M. Itagaki, M. Ueno, Y. Hoshi, I. Shitanda, Simultaneous determination of electrochemical impedance of lithium-ion rechargeable batteries with measurement of charge-discharge curves by wavelet transformation, Electrochim. Acta 235 (2017) 384–389, http://dx.doi.org/10.1016/j.electacta.2017.03.077.

[72] G. Nusev, D. Juricic, M. Gaberscek, J. Moskon, P. Boskoski, Fast impedance measurement of Li-Ion battery using discrete random binary excitation and wavelet transform, IEEE Access 9 (2021) 46152–46165, http://dx.doi.org/10.1109/ACCESS.2021.3058368.

[73] H. Watanabe, M. Uemori, I. Shitanda, M. Itagaki, Determination of electrochemical impedance of lithium-ion battery from charge curve by wavelet transformation, Electrochim. Acta 428 (2022) 140957, http://dx.doi.org/10.1016/j.electacta.2022.140957.

[74] M. Saccoccio, T.H. Wan, C. Chen, F. Ciucci, Optimal regularization in distribution of relaxation times applied to electrochemical impedance spectroscopy: Ridge and lasso regression methods - a theoretical and experimental study, Electrochim. Acta 147 (2014) 470–482, http://dx.doi.org/10.1016/j.electacta.2014.09.058.

[75] J. Honerkamp, J. Weese, Tikhonovs regularization method for ill-posed problems, Contin. Mech. Thermodyn. 2 (1) (1990) 17–30, http://dx.doi.org/10.1007/BF01170953.

[76] P.C. Hansen, D.P. O'Leary, The use of the L-curve in the regularization of discrete ill-posed problems, SIAM J. Sci. Comput. 14 (6) (1993) 1487–1503, http://dx.doi.org/10.1137/0914086.

[77] P.C. Hansen, Analysis of discrete ill-posed problems by means of the L-curve, SIAM Rev. 34 (4) (1992) 561–580, http://dx.doi.org/10.1137/1034115.

[78] T. Paul, P.W. Chi, P.M. Wu, M.K. Wu, Computation of distribution of relaxation times by Tikhonov regularization for Li ion batteries: usage of L-curve method, Sci. Rep. 11 (1) (2021) 12624, http://dx.doi.org/10.1038/s41598-021-91871-3.

[79] A. Maradesa, B. Py, T.H. Wan, M.B. Effat, F. Ciucci, Selecting the regularization parameter in the distribution of relaxation times, J. Electrochem. Soc. 170 (3) (2023) 030502, http://dx.doi.org/10.1149/1945-7111/acbca4.

[80] G. Wahba, A comparison of GCV and GML for choosing the smoothing parameter in the generalized spline smoothing problem, Ann. Statist. 13 (4) (1985) http://dx.doi.org/10.1214/aos/1176349743.

[81] Y.-J. Kim, C. Gu, Smoothing spline Gaussian regression: More scalable computation via efficient approximation, J. R. Stat. Soc. Ser. B Stat. Methodol. 66 (2) (2004) 337–356, http://dx.doi.org/10.1046/j.1369-7412.2003.05316.x.

[82] Y. Zhang, Y. Chen, M. Li, M. Yan, M. Ni, C. Xia, A high-precision approach to reconstruct distribution of relaxation times from electrochemical impedance spectroscopy, J. Power Sources 308 (2016) 1–6, http://dx.doi.org/10.1016/j.jpowsour.2016.01.067.

[83] A.L. Gavriljuk, D.A. Osinkin, D.I. Bronin, On a variation of the Tikhonov regularization method for calculating the distribution function of relaxation times in impedance spectroscopy, Electrochim. Acta 354 (2020) 136683, http://dx.doi.org/10.1016/j.electacta.2020.136683.

[84] F. Ciucci, C. Chen, Analysis of electrochemical impedance spectroscopy data using the distribution of relaxation times: A Bayesian and hierarchical Bayesian approach, Electrochim. Acta 167 (2015) 439–454, http://dx.doi.org/10.1016/j.electacta.2015.03.123, URL https://www.sciencedirect.com/science/article/pii/S0013468615007203.

[85] J. Huang, M. Papac, R. O'Hayre, Towards robust autonomous impedance spectroscopy analysis: A calibrated hierarchical Bayesian approach for electrochemical impedance spectroscopy (EIS) inversion, Electrochim. Acta 367 (2021) 137493, http://dx.doi.org/10.1016/j.electacta.2020.137493, URL https://www.sciencedirect.com/science/article/pii/S0013468620318867.

[86] B. Carpenter, A. Gelman, M.D. Hoffman, D. Lee, B. Goodrich, M. Betancourt, M. Brubaker, J. Guo, P. Li, A. Riddell, Stan: A probabilistic programming language, J. Stat. Softw. 76 (1) (2017).

[87] A. Pakman, L. Paninski, Exact Hamiltonian Monte Carlo for truncated multivariate Gaussians, J. Comput. Graph. Statist. 23 (2) (2014) 518–542, URL http://www.jstor.org/stable/43305741.

[88] D. Calvetti, E. Somersalo, Hypermodels in the Bayesian imaging framework, Inverse Problems 24 (3) (2008) 034013, http://dx.doi.org/10.1088/0266-5611/24/3/034013.

[89] M.B. Effat, F. Ciucci, Bayesian and hierarchical Bayesian based regularization for deconvolving the distribution of relaxation times from electrochemical impedance spectroscopy data, Electrochim. Acta 247 (2017) 1117–1129, http://dx.doi.org/10.1016/j.electacta.2017.07.050, URL https://www.sciencedirect.com/science/article/pii/S0013468617314676.

[90] J. Huang, N.P. Sullivan, A. Zakutayev, R. O'Hayre, How reliable is distribution of relaxation times (DRT) analysis? A dual regression-classification perspective on DRT estimation, interpretation, and accuracy, Electrochim. Acta 443 (2023) 141879, http://dx.doi.org/10.1016/j.electacta.2023.141879, URL https://www.sciencedirect.com/science/article/pii/S001346862300066X.

[91] N. Schlüter, T. Bergmann, S. Ernst, U. Schröder, Quality-indicator-based preprocessing for the distribution of relaxation times method, ChemElectroChem 8 (6) (2021) 1167–1182, http://dx.doi.org/10.1002/celc.202100173.

[92] N.J. Williams, C. Osborne, I.D. Seymour, M.Z. Bazant, S.J. Skinner, Application of finite Gaussian process distribution of relaxation times on SOFC electrodes, Electrochem. Commun. 149 (2023) 107458, http://dx.doi.org/10.1016/j.elecom.2023.107458, URL https://www.sciencedirect.com/science/article/pii/S1388248123000322.

[93] B. Py, A. Maradesa, F. Ciucci, Gaussian processes for the analysis of electrochemical impedance spectroscopy data: Prediction, filtering, and active learning, Electrochim. Acta 439 (2023) 141688, http://dx.doi.org/10.1016/j.electacta.2022.141688, URL https://www.sciencedirect.com/science/article/pii/S0013468622018448.

[94] V. Lempitsky, A. Vedaldi, D. Ulyanov, Deep image prior, in: 2018 IEEE/CVF Conference on Computer Vision and Pattern Recognition, 2018, pp. 9446–9454, http://dx.doi.org/10.1109/CVPR.2018.00984.

[95] J. Liu, F. Ciucci, The deep-prior distribution of relaxation times, J. Electrochem. Soc. 167 (2) (2020) 026506, http://dx.doi.org/10.1149/1945-7111/ab631a.

[96] A.J. Mayo, A.C. Antoulas, A framework for the solution of the generalized realization problem, Linear Algebra Appl. 425 (2–3) (2007) 634–662, http://dx.doi.org/10.1016/j.laa.2007.03.008.

[97] A. Sorrentino, I.V. Gosea, B. Patel, A.C. Antoulas, T. Vidakovic-Koch, Loewner framework and distribution of relaxation times of electrochemical systems: Solving issues through a data-driven modeling approach, SSRN Electron. J. (2022) http://dx.doi.org/10.2139/ssrn.4217752.

[98] T. Rüther, M. Schamel, C. Plank, F. Schomburg, F. Röder, M.A. Danzer, Cell-to-cell-variations of a panasonic NCR18650B, http://dx.doi.org/10.5281/zenodo.8182851.

[99] M. Schönleber, C. Uhlmann, P. Braun, A. Weber, E. Ivers-Tiffée, A consistent derivation of the impedance of a lithium-ion battery electrode and its dependency on the state-of-charge, Electrochim. Acta 243 (2017) 250–259, http://dx.doi.org/10.1016/j.electacta.2017.05.009.

[100] T.Q. Nguyen, C. Breitkopf, Determination of diffusion coefficients using impedance spectroscopy data, J. Electrochem. Soc. 165 (14) (2018) E826–E831, http://dx.doi.org/10.1149/2.1151814jes.

[101] J. Song, M.Z. Bazant, Electrochemical impedance imaging via the distribution of diffusion times, Phys. Rev. Lett. 120 (11) (2018) 116001, http://dx.doi.org/10.1103/PhysRevLett.120.116001.

[102] B. Boukamp, Interpretation of the Gerischer impedance in solid state ionics, Solid State Ion. 157 (1–4) (2003) 29–33, http://dx.doi.org/10.1016/S0167-2738(02)00185-6.

[103] B. Boukamp, Electrochemical impedance spectroscopy in solid state ionics: recent advances, Solid State Ion. 169 (1–4) (2004) 65–73, http://dx.doi.org/10.1016/j.ssi.2003.07.002.

[104] A. Kulikovsky, Why impedance of the gas diffusion layer in a PEM fuel cell differs from the Warburg finite-length impedance? Electrochem. Commun. 84 (2017) 28–31, http://dx.doi.org/10.1016/j.elecom.2017.09.014.

[105] D.A. Osinkin, An approach to the analysis of the impedance spectra of solid oxide fuel cell using the DRT technique, Electrochim. Acta 372 (2021) 137858, http://dx.doi.org/10.1016/j.electacta.2021.137858, URL https://www.sciencedirect.com/science/article/pii/S0013468621001481.

[106] D.A. Osinkin, Hydrogen oxidation kinetics on a redox stable electrode for reversible solid-state electrochemical devices: The critical influence of hydrogen dissociation on the electrode surface, Electrochim. Acta 389 (2021) 138792, http://dx.doi.org/10.1016/j.electacta.2021.138792.

[107] B.A. Boukamp, Derivation of a distribution function of relaxation times for the (fractal) finite length warburg, Electrochim. Acta 252 (2017) 154–163, http://dx.doi.org/10.1016/j.electacta.2017.08.154.

[108] N. Ogihara, S. Kawauchi, C. Okuda, Y. Itou, Y. Takeuchi, Y. Ukyo, Theoretical and experimental analysis of porous electrodes for lithium-ion batteries by electrochemical impedance spectroscopy using a symmetric cell, J. Electrochem. Soc. 159 (7) (2012) A1034–A1039, http://dx.doi.org/10.1149/2.057207jes.

[109] U. Schadeck, M. Hahn, T. Gerdes, W. Krenkel, M.A. Danzer, R. Moos, Sodium borosilicate glass separators as an electrolyte additive donor for improving the electrochemical performance of lithium-ion batteries, J. Electrochem. Soc. 166 (14) (2019) A3416–A3424, http://dx.doi.org/10.1149/2.1011914jes, URL https://iopscience.iop.org/article/10.1149/2.1011914jes/meta.

[110] L. Zhuang, X. Huang, Y. Lu, J. Tang, Y. Zhou, X. Ao, Y. Yang, B. Tian, Phase transformation and grain-boundary segregation in Al-Doped Li7La3Zr2O12 ceramics, Ceram. Int. 47 (16) (2021) 22768–22775, http://dx.doi.org/10.1016/j.ceramint.2021.04.295, URL https://www.sciencedirect.com/science/article/pii/S0272884221013547.

[111] E.A. Il'ina, D.A. Osinkin, Interpretation of the resistance of Li7La3Zr2O12 – Li2O–B2O3–SiO2 composite electrolytes for all–solid–state batteries using the distribution of relaxation times technique, J. Power Sources 580 (2023) 233370, http://dx.doi.org/10.1016/j.jpowsour.2023.233370, URL https://www.sciencedirect.com/science/article/pii/S0378775323007462.

[112] J.G. Lyagaeva, G.K. Vdovin, D.A. Medvedev, Distinguishing bulk and grain boundary transport of a proton-conducting electrolyte by combining equivalent circuit scheme and distribution of relaxation times analyses, J. Phys. Chem. C 123 (36) (2019) 21993–21997, http://dx.doi.org/10.1021/acs.jpcc.9b05705.

[113] A.V. Kuzmin, M.S. Plekhanov, A.S. Lesnichyova, Influence of impurities on the bulk and grain-boundary conductivity of CaZrO3-based proton-conducting electrolyte: A distribution of relaxation time study, Electrochim. Acta 348 (2020) 136327, http://dx.doi.org/10.1016/j.electacta.2020.136327, URL https://www.sciencedirect.com/science/article/pii/S0013468620307192.

[114] P. Shafiei Sabet, G. Stahl, D.U. Sauer, Non-invasive investigation of predominant processes in the impedance spectra of high energy lithium-ion batteries with nickel–cobalt–aluminum cathodes, J. Power Sources 472 (2020) 228189, http://dx.doi.org/10.1016/j.jpowsour.2020.228189, URL https://www.sciencedirect.com/science/article/pii/S0378775320304924.

[115] K. Pan, F. Zou, M. Canova, Y. Zhu, J.-H. Kim, Comprehensive electrochemical impedance spectroscopy study of Si-based anodes using distribution of relaxation times analysis, J. Power Sources 479 (2020) 229083, http://dx.doi.org/10.1016/j.jpowsour.2020.229083.

[116] M. Mandl, J. Becherer, D. Kramer, R. Mönig, T. Diemant, R.J. Behm, M. Hahn, O. Böse, M.A. Danzer, Sodium metal anodes: Deposition and dissolution behaviour and SEI formation, Electrochim. Acta 354 (2020) 136698, http://dx.doi.org/10.1016/j.electacta.2020.136698, URL https://www.sciencedirect.com/science/article/pii/S0013468620310914.

[117] L.U. Subasinghe, G. Satyanarayana Reddy, A. Rudola, P. Balaya, Analysis of heat generation and impedance characteristics of prussian blue analogue cathode-based 18650-type sodium-ion cells, J. Electrochem. Soc. 167 (11) (2020) 110504, http://dx.doi.org/10.1149/1945-7111/ab9ee9, URL https://iopscience.iop.org/article/10.1149/1945-7111/ab9ee9/meta.

[118] I.U. Mohsin, L. Schneider, M. Häringer, C. Ziebert, M. Rohde, W. Bauer, H. Ehrenberg, H.J. Seifert, Heat generation and degradation mechanisms studied on Na3V2(PO4)3/C positive electrode material in full pouch / coin cell assembly, J. Power Sources 545 (2022) 231901, http://dx.doi.org/10.1016/j.jpowsour.2022.231901, URL https://www.sciencedirect.com/science/article/pii/S0378775322008850.

[119] K. Schutjajew, T. Tichter, J. Schneider, M. Antonietti, C. Roth, M. Oschatz, Insights into the sodiation mechanism of hard carbon-like materials from electrochemical impedance spectroscopy, Phys. Chem. Chem. Phys. 23 (19) (2021) 11488–11500, http://dx.doi.org/10.1039/D1CP00610J, URL https://pubs.rsc.org/en/content/articlehtml/2021/cp/d1cp00610j.

[120] L. Bottoni, H. Darjazi, L. Sbrascini, A. Staffolani, S. Gabrielli, G. Pastore, A. Tombesi, F. Nobili, Electrochemical characterization of charge storage at anodes for sodium–Ion batteries based on corncob waste–derived hard carbon and binder, ChemElectroChem 10 (8) (2023) http://dx.doi.org/10.1002/celc.202201117.

[121] R. Franke-Lang, J. Kowal, Analysis of electrochemical impedance spectroscopy on zinc-air batteries using the distribution of relaxation times, Batteries 7 (3) (2021) 56, http://dx.doi.org/10.3390/batteries7030056.

[122] C. Sheng, F. Yu, C. Li, H. Zhang, J. Huang, Y. Wu, M. Armand, Y. Chen, Diagnosing the SEI layer in a potassium ion battery using distribution of relaxation time, J. Phys. Chem. Lett. 12 (8) (2021) 2064–2071, http://dx.doi.org/10.1021/acs.jpclett.1c00118.

[123] R. Soni, J.B. Robinson, P.R. Shearing, D.J. Brett, A.J. Rettie, T.S. Miller, Lithium-sulfur battery diagnostics through distribution of relaxation times analysis, Energy Storage Mater. 51 (2022) 97–107, http://dx.doi.org/10.1016/j.ensm.2022.06.016, URL https://www.sciencedirect.com/science/article/pii/S2405829722003245.

[124] J. Chen, E. Quattrocchi, F. Ciucci, Y. Chen, Charging processes in lithium-oxygen batteries unraveled through the lens of the distribution of relaxation times, Chem (2023) http://dx.doi.org/10.1016/j.chempr.2023.04.022.

[125] N. Togasaki, A. Nakao, T. Tanaka, U. Harada, H. Onish, H. Yasuda, S. Kobayashi, F. Maeda, T. Osaka, Utilization ratio of active materials in all-solid-state batteries examined using electrochemical impedance analysis with the transmission line model, J. Electrochem. Soc. 170 (5) (2023) 050519, http://dx.doi.org/10.1149/1945-7111/acd35b.

[126] W. Zhuo, J. Li, X. Li, L. Ma, G. Yan, H. Wang, S. Tan, W. Mai, Improving rechargeability of Prussian blue cathode by graphene as conductive agent for sodium ion batteries, Surf. Interfaces 23 (2021) 100911, http://dx.doi.org/10.1016/j.surfin.2020.100911, URL https://www.sciencedirect.com/science/article/pii/S2468023020309020.

[127] M. Steinhauer, S. Risse, N. Wagner, K.A. Friedrich, Investigation of the solid electrolyte interphase formation at graphite anodes in Lithium-Ion Batteries with electrochemical impedance spectroscopy, Electrochim. Acta 228 (2017) 652–658, http://dx.doi.org/10.1016/j.electacta.2017.01.128.

[128] T. Rüther, M. Schamel, C. Plank, F. Schomburg, F. Röder, M.A. Danzer, Cell-to-cell variation beyond parameter analysis — Identification and correlation of processes in Lithium-Ion Batteries using a combined distribution of relaxation times analysis, J. Power Sources 587 (2023) 233677, http://dx.doi.org/10.1016/j.jpowsour.2023.233677, URL https://www.sciencedirect.com/science/article/pii/S0378775323010534.

[129] J. Zhu, M. Knapp, X. Liu, P. Yan, H. Dai, X. Wei, H. Ehrenberg, Low-temperature separating lithium-ion battery interfacial polarization based on Distribution of Relaxation Times (DRT) of impedance, IEEE Trans. Transp. Electr. 7 (2) (2021) 410–421, http://dx.doi.org/10.1109/TTE.2020.3028475.

[130] X. Zhou, J. Huang, Z. Pan, M. Ouyang, Impedance characterization of lithium-ion batteries aging under high-temperature cycling: Importance of electrolyte-phase diffusion, J. Power Sources 426 (2019) 216–222, http://dx.doi.org/10.1016/j.jpowsour.2019.04.040.

[131] T. Rüther, C. Plank, M. Schamel, M.A. Danzer, Detection of inhomogeneities in serially connected lithium-ion batteries, Appl. Energy 332 (2023) 120514, http://dx.doi.org/10.1016/j.apenergy.2022.120514.

[132] X. Chen, L. Li, M. Liu, T. Huang, A. Yu, Detection of lithium plating in lithium-ion batteries by distribution of relaxation times, J. Power Sources 496 (2021) 229867, http://dx.doi.org/10.1016/j.jpowsour.2021.229867.

[133] M. Yi, F. Jiang, G. Zhao, D. Guo, D. Ren, L. Lu, M. Ouyang, Detection of lithium plating based on the distribution of relaxation times, in: Proceedings of 2021 IEEE 4th International Electrical and Energy Conference (CIEEC), Institute of Electrical and Electronics Engineers Inc, Piscataway, NJ, 2021, pp. 1–5, http://dx.doi.org/10.1109/CIEEC50170.2021.9510538.

[134] F. Katzer, M.A. Danzer, Analysis and detection of lithium deposition after fast charging of lithium-ion batteries by investigating the impedance relaxation, J. Power Sources 503 (2021) 230009, http://dx.doi.org/10.1016/j.jpowsour.2021.230009, URL https://www.sciencedirect.com/science/article/pii/S0378775321005371.

[135] F. Katzer, T. Rüther, C. Plank, F. Roth, M.A. Danzer, Analyses of polarisation effects and operando detection of lithium deposition in experimental half- and commercial full-cells, Electrochim. Acta 436 (2022) 141401, http://dx.doi.org/10.1016/j.electacta.2022.141401.

[136] D. Papurello, D. Menichini, A. Lanzini, Distributed relaxation times technique for the determination of fuel cell losses with an equivalent circuit model to identify physicochemical processes, Electrochim. Acta 258 (2017) 98–109, http://dx.doi.org/10.1016/j.electacta.2017.10.052, URL https://www.sciencedirect.com/science/article/pii/S0013468617321503.

[137] S. Dierickx, J. Joos, A. Weber, E. Ivers-Tiffée, Advanced impedance modelling of Ni/8YSZ cermet anodes, Electrochim. Acta 265 (2018) 736–750, http://dx.doi.org/10.1016/j.electacta.2017.12.029, URL https://www.sciencedirect.com/science/article/pii/S0013468617325896.

[138] P. Caliandro, A. Nakajo, S. Diethelm, J. van herle, Model-assisted identification of solid oxide cell elementary processes by electrochemical impedance spectroscopy measurements, J. Power Sources 436 (2019) 226838, http://dx.doi.org/10.1016/j.jpowsour.2019.226838.

[139] J. Hong, A. Bhardwaj, H. Bae, I.-h. Kim, S.-J. Song, Electrochemical impedance analysis of SOFC with transmission line model using Distribution of Relaxation Times (DRT), J. Electrochem. Soc. 167 (11) (2020) 114504, http://dx.doi.org/10.1149/1945-7111/aba00f.

[140] D.A. Osinkin, Detailed analysis of electrochemical behavior of high–performance solid oxide fuel cell using DRT technique, J. Power Sources 527 (2022) 231120, http://dx.doi.org/10.1016/j.jpowsour.2022.231120, URL https://www.sciencedirect.com/science/article/pii/S0378775322001434.

[141] D.A. Osinkin, Identification of gas diffusion phenomena on highly active Ni–ceramic anodes using the DRT technique, J. Power Sources 571 (2023) 233085, http://dx.doi.org/10.1016/j.jpowsour.2023.233085, URL https://www.sciencedirect.com/science/article/pii/S0378775323004603.

[142] H. Sumi, H. Shimada, Y. Yamaguchi, T. Yamaguchi, Y. Fujishiro, Degradation evaluation by distribution of relaxation times analysis for microtubular solid oxide fuel cells, Electrochim. Acta 339 (2020) 135913, http://dx.doi.org/10.1016/j.electacta.2020.135913.

[143] A. Weiß, S. Schindler, S. Galbiati, M.A. Danzer, R. Zeis, Distribution of relaxation times analysis of high-temperature PEM fuel cell impedance spectra, Electrochim. Acta 230 (2017) 391–398, http://dx.doi.org/10.1016/j.electacta.2017.02.011.

[144] M. Heinzmann, A. Weber, E. Ivers-Tiffée, Advanced impedance study of polymer electrolyte membrane single cells by means of distribution of relaxation times, J. Power Sources 402 (2018) 24–33, http://dx.doi.org/10.1016/j.jpowsour.2018.09.004, URL https://www.sciencedirect.com/science/article/pii/S0378775318309753.

[145] M. Heinzmann, A. Weber, E. Ivers-Tiffée, Impedance modelling of porous electrode structures in polymer electrolyte membrane fuel cells, J. Power Sources 444 (2019) 227279, http://dx.doi.org/10.1016/j.jpowsour.2019.227279.

[146] T. Reshetenko, A. Kulikovsky, Distribution of relaxation times: A tool for measuring oxygen transport resistivity of a low–pt PEM fuel cell cathode, J. Electrochem. Soc. 167 (14) (2020) 144505, http://dx.doi.org/10.1149/1945-7111/abc10f.

[147] T. Reshetenko, A. Kulikovsky, Understanding the distribution of relaxation times of a low–Pt PEM fuel cell, Electrochim. Acta 391 (2021) 138954, http://dx.doi.org/10.1016/j.electacta.2021.138954, URL https://www.sciencedirect.com/science/article/pii/S0013468621012445.

[148] H. Yuan, H. Dai, X. Wei, P. Ming, Internal polarization process revelation of electrochemical impedance spectroscopy of proton exchange membrane fuel cell by an impedance dimension model and distribution of relaxation times, Chem. Eng. J. 418 (2021) 129358, http://dx.doi.org/10.1016/j.cej.2021.129358, URL https://www.sciencedirect.com/science/article/pii/S1385894721009463.

[149] J.P. Schmidt, T. Chrobak, M. Ender, J. Illig, D. Klotz, E. Ivers-Tiffée, Studies on LiFePO4 as cathode material using impedance spectroscopy, J. Power Sources 196 (12) (2011) 5342–5348, http://dx.doi.org/10.1016/j.jpowsour.2010.09.121, URL https://www.sciencedirect.com/science/article/pii/S0378775310019786.

[150] H. Jia, P. Gao, L. Zou, K.S. Han, M.H. Engelhard, Y. He, X. Zhang, W. Zhao, R. Yi, H. Wang, C. Wang, X. Li, J.-G. Zhang, Controlling ion coordination structure and diffusion kinetics for optimized electrode-electrolyte interphases and high-performance Si anodes, Chem. Mater. 32 (20) (2020) 8956–8964, http://dx.doi.org/10.1021/acs.chemmater.0c02954.

[151] T.R. Tanim, E.J. Dufek, S.V. Sazhin, Challenges and needs for system-level electrochemical lithium-ion battery management and diagnostics, MRS Bull. 46 (5) (2021) 420–428, http://dx.doi.org/10.1557/s43577-021-00101-8.

[152] N. Togasaki, T. Yokoshima, Y. Oguma, T. Osaka, Detection of unbalanced voltage cells in series-connected lithium-ion batteries using single-frequency electrochemical impedance spectroscopy, J. Electrochem. Sci. Technol. 12 (4) (2021) 415–423, http://dx.doi.org/10.33961/jecst.2021.00115.

[153] T. Yokoshima, D. Mukoyama, H. Nara, S. Maeda, K. Nakazawa, T. Momma, T. Osaka, Impedance measurements of kilowatt-class lithium ion battery modules/cubicles in energy storage systems by square-current electrochemical impedance spectroscopy, Electrochim. Acta 246 (2017) 800–811, http://dx.doi.org/10.1016/j.electacta.2017.05.076.

[154] M. Kasper, M. Moertelmaier, M. Ragulskis, N. Al–Zubaidi R–Smith, J. Angerer, M. Aufreiter, A. Romero, J. Krummacher, J. Xu, D.E. Root, F. Kienberger, Calibrated electrochemical impedance spectroscopy and time–domain measurements of a 7 kWh automotive lithium–Ion battery module with 396 cylindrical cells, Batter. Supercaps 6 (2) (2023) http://dx.doi.org/10.1002/batt.202200415.

[155] J. Badeda, M. Kwiecien, D. Schulte, D. Sauer, Battery state estimation for lead-acid batteries under float charge conditions by impedance: Benchmark of common detection methods, Appl. Sci. 8 (8) (2018) 1308, http://dx.doi.org/10.3390/app8081308.

[156] S. Bauknecht, J. Kowal, B. Bozkaya, J. Settelein, E. Karden, Electrochemical impedance spectroscopy as an analytical tool for the prediction of the dynamic charge acceptance of lead-acid batteries, Batteries 8 (7) (2022) 66, http://dx.doi.org/10.3390/batteries8070066.

[157] J. Olarte, J. Martínez de Ilarduya, E. Zulueta, R. Ferret, U. Fernández-Gámiz, J.M. Lopez-Guede, A battery management system with EIS monitoring of life expectancy for Lead–Acid batteries, Electronics 10 (11) (2021) 1228, http://dx.doi.org/10.3390/electronics10111228.

[158] W. Waag, S. Käbitz, D.U. Sauer, Experimental investigation of the lithium-ion battery impedance characteristic at various conditions and aging states and its influence on the application, Appl. Energy 102 (1) (2013) 885–897, http://dx.doi.org/10.1016/j.apenergy.2012.09.030.

[159] E. Markevich, M.D. Levi, D. Aurbach, Comparison between potentiostatic and galvanostatic intermittent titration techniques for determination of chemical diffusion coefficients in ion-insertion electrodes, J. Electroanal. Soc. 580 (2) (2005) 231–237, http://dx.doi.org/10.1016/j.jelechem.2005.03.030.

[160] M. Ecker, T.K.D. Tran, P. Dechent, S. Käbitz, A. Warnecke, D.U. Sauer, Parameterization of a physico-chemical model of a lithium-ion battery, J. Electrochem. Soc. 162 (9) (2015) A1836–A1848, http://dx.doi.org/10.1149/2.0551509jes.

[161] M. Stevenson, S. Weiß, G. Cha, M. Schamel, L. Jahn, D. Friedrich, M.A. Danzer, J.Y. Cheong, J. Breu, Osmotically delaminated silicate nanosheet-coated NCM for ultra-stable li+ storage and chemical stability toward long-term air exposure, Small (Weinheim Bergstrasse, Ger.) (2023) e2302617, http://dx.doi.org/10.1002/smll.202302617.

[162] B. Sanchez, G. Vandersteen, R. Bragos, J. Schoukens, Optimal multisine excitation design for broadband electrical impedance spectroscopy, Meas. Sci. Technol. 22 (11) (2011) 115601, http://dx.doi.org/10.1088/0957-0233/22/11/115601.

[163] R. Koch, A. Jossen, Speed optimized multisine stimuli for electrochemical impedance spectroscopy with a switched mode excitation, in: 2014 IEEE Vehicle Power and Propulsion Conference (VPPC), IEEE, 2014, pp. 1–6, http://dx.doi.org/10.1109/VPPC.2014.7007135.

[164] J.P. Christophersen, J. Morrison, W. Morrison, C. Motloch, Rapid impedance spectrum measurements for state-of-health assessment of energy storage devices, SAE Int. J. Passeng. Cars - Electron. Electr. Syst. 5 (1) (2012) 246–256, http://dx.doi.org/10.4271/2012-01-0657.

[165] B. Ulgut, Methods-employing multisine electrochemical impedance spectroscopy for batteries in galvanostatic mode, J. Electrochem. Soc. 169 (11) (2022) 110510, http://dx.doi.org/10.1149/1945-7111/ac9d05.

[166] H. Zappen, F. Ringbeck, D. Sauer, Application of time-resolved multi-Sine impedance spectroscopy for lithium-ion battery characterization, Batteries 4 (4) (2018) 64, http://dx.doi.org/10.3390/batteries4040064.

[167] A.Y. Kallel, O. Kanoun, On the design of multisine signals for maintaining stability condition in impedance spectroscopy measurements of batteries, J. Energy Storage 58 (2023) 106267, http://dx.doi.org/10.1016/j.est.2022.106267.

[168] R. Suresh, S. Swaminathan, R. Rengaswamy, Rapid impedance spectroscopy using dual phase shifted chirp signals for electrochemical applications, Int. J. Hydrogen Energy 45 (17) (2020) 10536–10548, http://dx.doi.org/10.1016/j.ijhydene.2019.10.031.

[169] M. Kowalewski, Selection of excitation signals for high-impedance spectroscopy, J. Phys. Conf. Ser. 459 (2013) 012060, http://dx.doi.org/10.1088/1742-6596/459/1/012060.

[170] J. Sihvo, T. Roinila, D.-I. Stroe, Broadband impedance measurement of lithium-ion battery in the presence of nonlinear distortions, Energies 13 (10) (2020) 2493, http://dx.doi.org/10.3390/en13102493.

[171] R. Land, P. Annus, M. Min, Time-frequency impedance spectroscopy: excitation considerations, in: Proceedings of the IMEKO TC4 International Symposium on Novelties in Electrical Measurements and Instrumentations, 2007, pp. 1–4.

[172] G.S. Popkirov, R.N. Schindler, A new impedance spectrometer for the investigation of electrochemical systems, Rev. Sci. Instrum. 63 (11) (1992) 5366–5372, http://dx.doi.org/10.1063/1.1143404.

[173] C. Gabrielli, F. Huet, M. Keddam, Comparison of sine wave and white noise analysis for electrochemical impedance measurements, J. Electroanal. Soc. 335 (1–2) (1992) 33–53, http://dx.doi.org/10.1016/0022-0728(92)80230-2.

[174] A. Lasia, Electrochemical impedance spectroscopy and its applications, in: B.E. Conway, J.O. Bockris, R.E. White (Eds.), Modern Aspects of Electrochemistry, Vol. 32, Kluwer Academic Publishers, Boston, 2002, pp. 143–248, http://dx.doi.org/10.1007/0-306-46916-2_2.

[175] K.J. Szekeres, S. Vesztergom, M. Ujvári, G.G. Láng, Methods for the determination of valid impedance spectra in non–stationary electrochemical systems: Concepts and techniques of practical importance, ChemElectroChem 8 (7) (2021) 1233–1250, http://dx.doi.org/10.1002/celc.202100093.

[176] B. Boukamp, Practical application of the Kramers-Kronig transformation on impedance measurements in solid state electrochemistry, Solid State Ion. 62 (1–2) (1993) 131–141, http://dx.doi.org/10.1016/0167-2738(93)90261-Z.

[177] F.W. King (Ed.), Hilbert Transforms, Cambridge University Press, 2010, http://dx.doi.org/10.1017/CBO9780511735271.

[178] H.A. Kramers, La diffusion de la lumière par les atomes, in: Atti del Congresso Internationale dei Fisici, Como, 1927, pp. 545–557.

[179] R. de L. Kronig, On the theory of dispersion of X-Rays, J. Opt. Soc. Amer. 12 (6) (1926) 547, http://dx.doi.org/10.1364/JOSA.12.000547.

[180] M. Urquidi-Macdonald, S. Real, D.D. Macdonald, Applications of Kramers—Kronig transforms in the analysis of electrochemical impedance data—III. Stability and linearity, Electrochim. Acta 35 (10) (1990) 1559–1566, http://dx.doi.org/10.1016/0013-4686(90)80010-L.

[181] G.A. Ruiz, C.J. Felice, Low error Kramers-Kronig estimations using symmetric extrapolation method, J. Electr. Bioimpedance 12 (1) (2021) 147–152, http://dx.doi.org/10.2478/joeb-2021-0017.

[182] J.M. Esteban, M.E. Orazem, On the application of the Kramers–Kronig relations to evaluate the consistency of electrochemical impedance data, J. Electrochem. Soc. 138 (1) (1991) 67–76, http://dx.doi.org/10.1149/1.2085580.

[183] B.A. Boukamp, A linear Kronig–Kramers transform test for immittance data validation, J. Electrochem. Soc. 142 (6) (1995) 1885–1894, http://dx.doi.org/10.1149/1.2044210.

[184] C. Plank, T. Rüther, M.A. Danzer, Detection of non-linearity and non-stationarity in impedance spectra using an extended Kramers-Kronig test without overfitting, in: 2022 International Workshop on Impedance Spectroscopy (IWIS), IEEE, 2022, pp. 1–6, http://dx.doi.org/10.1109/IWIS57888.2022.9975131.

[185] M. Schönleber, D. Klotz, E. Ivers-Tiffée, A method for improving the robustness of linear Kramers-Kronig validity tests, Electrochim. Acta 131 (2014) 20–27, http://dx.doi.org/10.1016/j.electacta.2014.01.034.

[186] C.A. Schiller, F. Richter, E. Gülzow, N. Wagner, Validation and evaluation of electrochemical impedance spectra of systems with states that change with time, Phys. Chem. Chem. Phys. 3 (3) (2001) 374–378, http://dx.doi.org/10.1039/B007678N.

[187] W. Ehm, H. Göhr, R. Kaus, B. Röseler, C.A. Schiller, The evaluation of electrochemical impedance spectra using a modified logarithmic Hilbert transform, ACH - Models Chem. 137 (2000) 145–157.

[188] N. Balabanian, W.R. Lepage, What is a minimum-phase network? Trans. Am. Inst. Electr. Eng., I 74 (6) (1956) 785–788, http://dx.doi.org/10.1109/TCE. 1956.6372462.

[189] W. Ehm, Expansions for the logarithmic Kramers-Kronig relations, 1991, URL https://zahner.de/media-files/support_downloads/files/zhitehm.pdf.

[190] C.F. Mänken, D. Schäfer, R.-A. Eichel, F. Kunz, Automatic data curation and analysis pipeline for electrochemical impedance spectroscopy measurements conducted on solid oxide cell stacks, ECS Trans. 111 (6) (2023) 373–383, http://dx.doi.org/10.1149/11106.0373ecst.

[191] W. Strunz, C.A. Schiller, J. Vogelsang, The change of dielectric properties of barrier coatings during the initial state of immersion, Mater. Corros. 59 (2) (2008) 159–166, http://dx.doi.org/10.1002/maco.200804156.

[192] J. Liu, T.H. Wan, F. Ciucci, A Bayesian view on the Hilbert transform and the Kramers-Kronig transform of electrochemical impedance data: Probabilistic estimates and quality scores, Electrochim. Acta 357 (2020) 136864, http://dx.doi.org/10.1016/j.electacta.2020.136864, URL https://www.sciencedirect.com/science/article/pii/S0013468620312573.

[193] B.A. Boukamp, A. Rolle, Use of a distribution function of relaxation times (DFRT) in impedance analysis of SOFC electrodes, Solid State Ion. 314 (2018) 103–111, http://dx.doi.org/10.1016/j.ssi.2017.11.021.